Modeling and Signal Processing of Low-Finesse Fabry-Perot Interferometric Fiber Optic Sensors

Cheng Ma

Dissertation submitted to the faculty of the
Virginia Polytechnic Institute and State University
in partial fulfillment of the requirements for the degree of

Doctor of Philosophy
in
Electrical Engineering

Anbo Wang, Chair

Yong Xu

Ting-Chung Poon

Gary R. Pickrell

James R. Heflin

September 4, 2012
Blacksburg, Virginia

Keywords: Fiber Optics, Fiber Optic Sensors, Fabry-Perot, White-Light Interferometry

Modeling and Signal Processing of Low-Finesse Fabry-Perot Interferometric Fiber Optic Sensors

Cheng Ma

ABSTRACT

This dissertation addresses several theoretical issues in low-finesse fiber optic Fabry-Perot Interferometric (FPI) sensors. The work is divided into two levels: modeling of the sensors, and signal processing based on White-Light-Interferometry (WLI).

In the first chapter, the technical background of the low-finesse FPI sensor is briefly reviewed and the problems to be solved are highlighted.

A model for low finesse Extrinsic FPI (EFPI) is developed in Chapter 2. The theory is experimentally proven using both single-mode and multimode fiber based EFPIs. The fringe visibility and the additional phase in the spectrum are found to be strongly influenced by the optical path difference (OPD), the output spatial power distribution and the working wavelength; however they are not directly related to the light coherence.

In Chapter 3, the Single-Multi-Single-mode Intrinsic FPI (SMS-IFPI) is theoretically and experimentally studied. Reflectivity, cavity refocusing, and the additional phase in the sensor spectrum are modeled. The multiplexing capacity of the sensor is dramatically increased by promoting light refocusing. Similar to EFPIs, wave-front distortion generates an additional phase in the interference spectrogram. The resultant non-constant phase plays an important role in causing abrupt jumps in the demodulated OPD.

WLI-based signal processing of the low-finesse FP sensor is studied in Chapter 4. The lower bounds of the OPD estimation are calculated, the bounds are applied to evaluate OPD demodulation algorithms. Two types of algorithms (TYPE I & II) are studied and compared. The TYPE I estimations suffice if the requirement for resolution is relatively low. TYPE II estimation has dramatically reduced error, however, at the expense of potential demodulation jumps. If the additional phase is reliably dependent on OPD, it can be calibrated to minimize the occurrence of such jumps.

In Chapter 5, the work is summarized and suggestions for future studies are given.

To Yanna

for the amazing support you have always provided

Acknowledgements

I am indebted and thankful to my advisor, Dr. Anbo Wang, for providing me this opportunity to work on something I truly enjoy. I learnt so much from him in every aspects of my professional life. His encouragements gave me the courage to overcome difficulties, and gained me the confidence to develop an academic career. He is not only a wonderful advisor, but also a role model and a close friend.

I would like to thank the other committee members, Dr. Gary R. Pickrell, Dr. Yong Xu, Dr. Ting-Chung Poon, and Dr. James R. Heflin for their assistances throughout my research. I am deeply grateful to Ms. Mary L. Hallauer and Dr. William L. Hallauer for their tremendous help as teachers and friends.

I would like to thank my dearest friends and colleagues at CPT, Dorothy Wang, Kathy Wang, and Bo Dong for their help and friendship in the past 6 years. Thanks also extend to Dr. Evan Lally, Dr. Zhengying Li, Dr. Brian Scott, Dr. James Gong, Dr. Ming Han, Dr. Yizheng Zhu, Dr. Kristie Cooper, Dr. Baigang Zhang, Dr. Zhengyu Huang, Dr. Juncheng Xu, Dr. Fabin Shen and Ms. Debbie Collins for their helps, advices, and all kinds of contributions to my research..

Special gratitude goes to my best friends and teachers in Blacksburg—Bin Zhang & Juan Wang, Liguo Kong & Hong Tang, Chunlin Luo & Chen Tang & Bright Zheng, Teresa Ehrlich & David Ehrlich—for all the helps and beautiful memories they have brought.

I would like to express my deepest gratitude to my parents, who have been encouraging and supporting me to get this far. I would like to thank my wife, Yanna, for her persistent assistance and encouragement. Without her care and love, this dissertation would not have been possible.

Contents

List of Figures

List of Tables

Chapter 1 Introduction

1.1. Background

1.1.1 Fiber-optic sensing in general

The development of optical fibers is a scientific and technological miracle, the significance of which has been recognized by the 2009 Nobel Prize. Besides their glaring triumph in telecommunication, optical fibers have brought the industrial world another revolution in the area of sensing. Made from purely insulating dielectric materials (typically fused silica), fibers show significant improvements in their immunity to electromagnetic interference (EMI) and corrosion; as such, when sensors are made using the fibers, they fit perfectly to sensing applications where EMI and/or corrosion are of major concerns. The extremely low transmission loss and high melting temperature also benefit applications requiring long-distance, harsh-environment measurements. Being developed for nearly three decades, fiber-optic (FO) sensing has achieved wide commercialization [1, 2], and the technology is still expanding vigorously [3-5].

Two effects in the fiber have been widely explored as major sensing mechanisms. The first effect is distributed linear or nonlinear scattering along the fiber. Such scatterings (Rayleigh, Raman, Brillouin, etc.) can be generated along the whole fiber, their temporal and spectral features can be affected by physical parameters such as temperature and strain. Fully distributed FO sensing technologies (capable of measuring a one-dimensional span from hundreds of meters up to tens of kilometers in a spatially continuous manner) are mainly based on this mechanism [6-8]. The second effect involves optical interference inside the fiber. Whenever the optical beam transmitted inside the fiber is split into multiple parts (by locally distributed reflection or scattering), they will interfere once re-coupled back to the original transmission mode. Devices which can perform such beam-splitting and re-coupling can be generally classified as FO interferometers, such as Mach-Zehnder (MZ), Fabry-Perot (FP), Michelson, Sagnac interferometers, and fiber gratings [9, 10]. The split beams travel with different phase velocities or through distinct optical paths (or both), and thus their interference produces spectral patterns encoded with the optical path difference (OPD) among them. Because the interference is sensitive to OPD change as small as a fraction of the optical

wavelength (sub-micrometer), such devices can be used as highly sensitive single-point or multi-point (quasi-distributed) sensing elements. This project deals with signal processing issues of one type of such devices, the low-finesse FO-FP interferometers.

1.1.2 Low-finesse fiber-optic Fabry-Perot interferometers

Low-finesse means that the two reflection surfaces forming the FP cavity have similar but low reflectivities (typically less than 7% power reflectivity), so secondary reflections do not contribute much to the spectral pattern of the interference spectrum. If one of the surfaces (usually the one on the far-end from the lead-in beam) is coated with highly reflective coating which generates a higher reflection, this structure is sometimes referred to as a FO Fizeau interferometer [11]. Because secondary reflections inside a Fizeau interferometer can also be neglected for most cases, it can be classified as low-finesse and is accordingly covered by this research. The technical strategy behind "low-finesse" is to minimize fabrication complexity (thus bring down the cost) and maximize sensor robustness. The cost and structural/chemical instabilities (at high temperatures) associated with highly-reflective coatings tend to jeopardize sensor performance and cost, and is thus avoided universally in the sensing community.

In the past two decades, the Center for Photonics Technology at Virginia Tech involved in developing all kinds of low-finesse FO FP sensors. Sensors have been developed to measure temperature, strain, pressure, acoustic emission, EM fields, acceleration, partial discharge, biological/chemical agents, etc.[12-16]. The success of the technology does not only stay within the lab, but also extends to field applications. Our field tests clearly demonstrated the technology's superior capabilities over their electrical counterpart, and help to secure a niche market for such devices.

1.2. Signal processing approaches for low-finesse FO FPI

One of the major achievements of the FO-FPI is its ability to perform high-precision distance/ displacement measurements, which has been widely adopted in Scanning Probe Microscopy (SPM) [17-19]. Such applications only involve displacement measurement of much less than a wavelength, in which case quadrature detection may be well approximated as linear, and displacement sensitivity as high as 2 fm/$(Hz)^{1/2}$ was achieved

[20]. For measurements involving larger OPD change, single laser or dual-laser arrangements were used in a "fringe counting" mode [21, 22]. Such narrow line-width laser based technologies only provide relative OPD measurements, and suffer from intensity noise. Multiplexing is also difficult to achieve using this method.

In many applications, absolute OPD measurement is essential. In such practices, white-light interferometry (WLI) is widely adopted. The term "WLI" often refers to two different technologies when applied to FO FPI. The first technology (denoted as type 1 WLI) utilizes a low-coherent broadband source together with another local OPD-scanning interferometer to interrogate the sensor's OPD by reading the maximum of the total interference when the OPDs of the two interferometers match [23-26]. The second technology (type 2 WLI) employs a spectrometer (either a broadband source with a monochromater or a wavelength-swept laser with a detector) to interrogate the interference spectrum of the FPI, which gives direct estimation of the OPD [27]. Both methods have their own pros and cons. For the first technology, absolute measurement is readily achieved, at the expense of higher system complexity. The second scheme significantly simplifies the system and opens up possibility for multiplexing. However, effective and reliable signal processing remains challenging, as will be detailed in the next section. This project will focus on solving some key signal processing issues in the type 2 WLI-FP systems.

1.3. Identification of problems

1.3.1 Basic signal processing concept

The interference spectrum of the low-finesse FPI can be written as

$$I \propto 1 + FV \cdot \cos\left(k_0 \cdot OPD + \varphi_0\right) \tag{1.1}$$

where FV is a real number between 0 and 1, denoting the fringe visibility, which is directly related to the signal to noise ratio (SNR). k_0 is the wavenumber in vacuum, defined by $k_0 = 2\pi/\lambda_0$, where λ_0 is the wavelength in vacuum. OPD is the parameter to be determined, it is related to the FP cavity parameter as $OPD=2n_{\text{eff}}L$, where n_{eff} is the effective refractive index of the FP cavity medium, and L is the physical cavity length. φ_0

is the initial phase (or additional phase) term, the significance of which has been underestimated in the past. A detailed analysis and treatment of this phase term will be a major task in this project. The total phase, or phase of the fringe, is defined through $\varphi_{tot} = k_0 OPD + \varphi_0$. The whole story of WLI based FP signal demodulation lies in estimating the frequency (*OPD*) of a given sensor spectrum *I*. In general, the demodulation algorithms fall within two categories.

Category 1: OPD estimation. This approach directly estimates the "frequency" of the spectrum (OPD). It provides absolute measurement, but the accuracy is comparatively low.

Category 2: Total phase estimation. Tracking the spectral position of a single point (or multiple points), such as peaks and valleys, always yields much accurate characterization. However, this method relies on the assumption that the particular fringe on which the special observation point resides can be identified. When applied to spectrum with one "fringe" being easily identified (such as fiber Bragg grating), this method works fine; however it encounters tremendous difficulty when applied to FP demodulation, due to the fact that all fringes appear to be identical. Noise and shift of the additional phase φ_0 can both result in misinterpretation of the fringe order, and this so-called phase ambiguity (or 2π ambiguity, fringe order ambiguity) will give rise to abrupt discontinuities (or simply put, "jumps") in the demodulated cavity length. In a word, higher estimation accuracy always comes at the expense of non-absolute measurement, as reflected by the risks of demodulation jumps.

1.3.2 Available methods for direct OPD estimation

Direct OPD estimation is of special importance due to two facts: 1) It offers absolute measurement of the cavity length and 2) fringe order determination in high-resolution peak-tracking approaches relies on accurate OPD estimation.

OPD estimation in Eq. 1.1 is in principle identical to frequency estimation of a discrete time-domain signal, with the evenly sampled temporal points being substituted with evenly sampled points in the wavenumber domain. Two classes of methods are typically used for frequency estimation in sinusoidal signals: non-parametric frequency estimation

(classical) and parametric frequency estimation (modern). In classical frequency estimation, typical approach involves computing the periodogram of the signal (by using fast Fourier transform, FFT). For circumstances where periodogram fails to provide satisfactory results (especially poor spectral resolution), parametric spectral estimation methods are employed. Some of the most popular algorithms are: autoregressive-moving-average (ARMA) model estimation, Pisarenko harmonic decomposition (PHD), multiple signal classification (MUSIC), and estimating signal parameter via rotational invariance techniques (ESPRIT), etc [28, 29]. To date, most signal processing approaches employed for WLI -FP signal demodulation are based on non-parametric estimation. Only very few papers report WLI-FP spectral characterization using parametric approaches [30].

1.3.3 Brief review of WLI-FP signal demodulation algorithms

In 1992, Chen *et al*. proposed a method to track the peak position of the fringe in the spectrum [31]. This method is in principle a total phase approach; for applications involving larger cavity length change (over λ/2), fringe ambiguity will come into play. The basic idea has been developed over the years and was widely adopted as "peak tracking" method [32, 33]. In the early 90's, Claus *et al*. developed a simple method to demodulate the cavity length of a fiber FP sensor [34]. Denoting two neighboring fringe peaks (or valleys) in the spectrum as λ_1 and λ_2, cavity length can be readily obtained using

$$d = \lambda_1\lambda_2 / \left(2n_{eff}\left|\lambda_1 - \lambda_2\right|\right) \tag{1.2}$$

This method is afterwards named the "peak-to-peak" method and sought wide applications and developments [35, 36]. The approach is very simple and provides absolute measurement, however, it is very sensitive to noise, as the noise term on the denominators tends to be amplified. In the late 90's, using the FFT peak to directly indicate the cavity length was proposed and the accuracy of this approach was improved by interpolation or zero-padding [37, 38]. This approach also provides absolute measurement, but suffers from low accuracy, as the peak-to-peak method. In 2003, Qi *et al*. developed an approach aiming to solve both the poor accuracy and fringe ambiguity problem [39]. The method uses Eq. 1.2 to estimate the fringe order, and applies peak-tracking to determine the cavity length. This approach is apparently an attempt to use

total phase demodulation, and solves the fringe ambiguity problem to some extent. However, it has several constrains. First, the algorithm performs better when total number of fringes in the spectrum is reduced. As fringe number increases, using only two peaks to determine the fringe order and only one peak to calculate the cavity length loses too much information. Secondly, fringe order ambiguity problem still exists. This is due to two facts: 1) use Eq.1.2 to estimate the fringe order is still too noisy to provide reliable predictions and 2) the method is based on the assumption that the additional phase term in Eq. 1.1 is a constant. In 3.4.2, it will be shown that any algorithm with the assumption of constant additional phase is intrinsically problematic and will lead to fringe order ambiguity. In 2004, Han *et al*. proposed a method based on curve fitting to estimate the cavity's OPD [40]. The method recognized the non-constant additional phase term in Eq. 1.1, and accordingly treated this term by a theoretical model. This method is basically a total phase approach and thus is susceptible to fringe ambiguity; meanwhile, it is only applicable to single-mode fiber (SMF) based extrinsic FPI (EFPI, the definition of which will be given in Section 2). In 2005, Shen *et al*. proposed a phase-linear-regression method to perform the frequency estimation of the interference spectrum [27]. The approach is divided into two parts. In the first step, a phase-linear-regression estimation is carried out using the entire spectrum which gives comparatively low-quality OPD estimation; in the second step, a correction is made to the first-step estimation based on pre-stored information regarding the additional phase in Eq. 1.1. This approach shows excellent precision, because it effectively uses the whole spectrum for estimation. However, in order to have higher precision, total phase approach is applied in step two with the assumption that the additional phase is a constant, which intrinsically will lead to fringe order ambiguity and subsequently cause demodulation jumps. From the year 2006 to 2011, new algorithms were published each year, with incremental improvements to the previous ones. For example, algorithms proposed by Jiang (2008) [41-43], Majumdar *et al.* (2009) [44, 45] used direct OPD estimation methods (phase-linear-regression and FFT for absolute measurement), and the work by Huang (2006) [46] and Zhou *et al*. (2011) [47] reported methods based on curve fitting which fell in the category of total phase demodulation. In 2006, Rao *et al.* published a FP signal demodulation algorithm using

Pisarenko harmonic decomposition (PHD), which is a parametric method giving direct OPD estimation [30, 48].

1.3.4 Brief review of low-finesse FO FP model

Physical models describing the spectral behavior of low-finesse FP cavities are indispensable in WLI-FP signal processing mainly due to 1) A good physical model helps to interpret the FP spectrum, which leads to better estimation of the OPD and 2) An effective model brings the sensor design to a higher engineering level to improve the signal demodulation quality by improving the SNR and reducing the additional phase shift.

In 1991, Murphy *et al*. modeled single-mode-fiber (SMF) extrinsic FPI (EFPI, in which the light diffracts into free space inside the cavity) by regarding the fiber end face as a point source and treated wave propagation using ray optics [22]. The model can roughly explain fringe visibility drop at larger OPD but fails to account for additional phase φ_0 as shown in Eq. 1.1. In 1995, Arya *et al*. treated the SMF-EFPI problem numerically using diffraction theory, and gave much better agreement between measured and predicted fringe visibility as a function of OPD [49]. The drawbacks of the model were lack of analytical expression and ignorance of the additional phase term. In 1999, Perennes *et al*. published their work in modeling the multimode-fiber (MMF) EFPI by a geometrical optics treatment [50]. The model only works for cases when "even excitation" condition is fulfilled (all the modes in the MMF are equally excited); however, this assumption is invalid for most applications. In 2004, Han *et al*. published a more rigorous model for MMF-EFPI, in which fiber mode analysis was used to precisely describe the FP cavity [51]. The model gave clear insights into the physics of the MMF-EFPI, and drew some important conclusions. Later in 2006, the same authors announced the implication of the model on an additional phase shift, which was surprisingly dependent on modal-excitation condition in the MMF [52]. However, a drawback of the model is its complexity and lack of analytical solution. For a standard MMF, mode excitation condition in the MMF fiber is difficult to be analyzed exactly, upon which the model is relied. In 2004, Han *et al*. reported an analytical model rigorously describing SMF-EFPI, and the wave-propagation induced additional phase term was well interpreted [40]. In

2011, another model for SMF-EFPI was proposed by Wilkinson *et al*. aiming at addressing multiple reflections and angular misalignment issues frequently encountered in SPM applications [53]. Unfortunately, theoretical models for intrinsic FPI (IFPI) were missing in the past literature.

1.3.5 Identification of problems

The signal processing of the WLI-FPI involves two levels: 1) modeling of the device to initiate connection between spectral parameters and cavity physical parameters and 2) demodulation of the WLI-FP spectrum to correlate the spectrum to cavity physical parameters (typically OPD). As revealed by the above literature reviews, problems exist in both levels.

Level 1: Physical modeling

Problem 1: The current modeling approaches for MMF-EFPI is not practical. They are either based on over-idealized assumptions (as in [50]) or too complicated in reflecting a real device (as in [51, 52]). An effective model to predict the behavior of a real MMF-EFPI is desired.

Problem 2: A theoretical analysis of the IFPI is missing in the literature.

Level 2: Signal processing

Problem 3: A vast variety of WLI-based signal demodulation algorithms have been developed in the past 30 years. Among them, or other than them, is there a "best" algorithm? Is there an ultimate achievable precision?

Problem 4: For high-accuracy estimation, total-phase demodulation schemes are applied. However, abrupt demodulated signal jump associated with such schemes is a notorious problem which stays unsolved. What factors cause the jumps? Can the jumps be eliminated, or reduced in a controllable manner?

This dissertation aims at addressing these remaining, but important issues in fiber-optic low-finesse WLI-FPI systems.

Chapter 2 Modeling of Fiber Optic Low-Finesse EFPI Sensors

2.1 Introduction

The spectrum of fiber optic low-finesse extrinsic Fabry-Perot (FP) interferometers (EFPIs) is studied in this chapter. Such fiber coupled interferometers have been demonstrated as highly sensitive and robust sensors for measurement of temperature [14, 54], strain [11], pressure [55, 56] and acoustic wave [57]. White-light interferometry [39], in which the interferometer is illuminated either by a broadband optical source or a wavelength-tunable laser and its reflected spectrum is analyzed, has shown promising advantages over other interrogation counterparts in terms of demodulation accuracy, absolute measurement and immunity to optical power instability. In order to make accurate and reliable measurements, the sensor spectrum needs to be characterized carefully, some advanced signal processing algorithms have been developed to this end [27, 39, 40]. While it is well understood that the demodulation error scales with noise power in the spectrum [58], the demand for high fringe visibility becomes crucial, especially if a multimode fiber (MMF) is used for excitation. During the past few years, it has been reported in several publications [40, 59, 60] that the additional phase in the spectrum also plays an important role in signal processing, which may potentially lead to abrupt jumps in the demodulated sensor cavity length (see 3.4.2). As such, in-depth theoretical modeling for both single-mode fiber (SMF) and MMF based EFPIs have been investigated in the past two decades [40, 49-51], aiming to find the dependence of sensor output spectrum on sensor geometry and optical property.

Arya et al. [49] addressed the fringe visibility of SMF-EFPI by considering diffraction in the interferometer cavity, the similar approach was extended to study the beam propagation (diffraction) and re-coupling induced additional phase term by Han et al. [40]. While SMF-EFPI manifests well-defined electromagnetic (EM) field profile in the cavity, MMF-EFPI does not: because MMF can have very diverse mode excitation conditions, each guided mode has its individual mode profile yet the phase differences among the excited modes are extremely complex, this poses considerable difficulties in modeling the MMF-EFPI. Pérennès et al. [50] developed a simple geometrical-optics approach, their theory led to an analytical solution for the fringe visibility, but was not

sufficiently accurate for many real applications. Han *et al.* [51, 52] treated the problem with a more rigorous EM field approach using optical fiber mode theory, and both the fringe visibility and additional phase issues have been addressed. All the above theories contributed to our understanding of the EFPI fiber sensor behavior; however, several key issues still remained unsolved.

The models based on rigorous EM field treatments, although promising in computing good numerical solutions, encounter difficulties at bridging the physical model with real-world applications, for example, mode excitation in MMF can be very complex, and may vary upon multiple environmental factors; all these factors can couple together to make the problem extremely complicated. In addition, several basic questions have yet been satisfactorily answered. In experiments, it is found that the fringe visibilities of MMF-EFPIs typically fade much faster as the cavity lengths increase than SMF-EFPIs do. How does this phenomenon relate to the temporal and spatial degree of coherence of the output light from the excitation fiber? In intrinsic Fabry-Perot interferometric (IFPI) sensors, the cavity-length-dependent additional phase can ultimately lead to demodulation discontinuities (see 3.4.2)[12]. Will this additional phase also behave similarly for the EFPI sensors? In principle, any fiber can experience a smooth transition from single mode-few mode-multimode operation without clear boundaries. Is there a unified theory applicable to all these working conditions? The theory described in the following subsection aims to solve these problems.

2.2 Development of the theory

2.2.1 Fundamental concepts

The subject is optical fiber low-finesse EFPIs. For the two types of dielectric materials typically encountered in EFPIs—silica and sapphire, the power reflectivities are approximately 4% and 7% respectively, sufficiently small to neglect multiple reflections inside the FP cavity. The word “extrinsic” refers to free-space propagation of the optical beam inside the cavity, as in contrast to “intrinsic”, in which case the propagation of the beam is assumed to be guided.

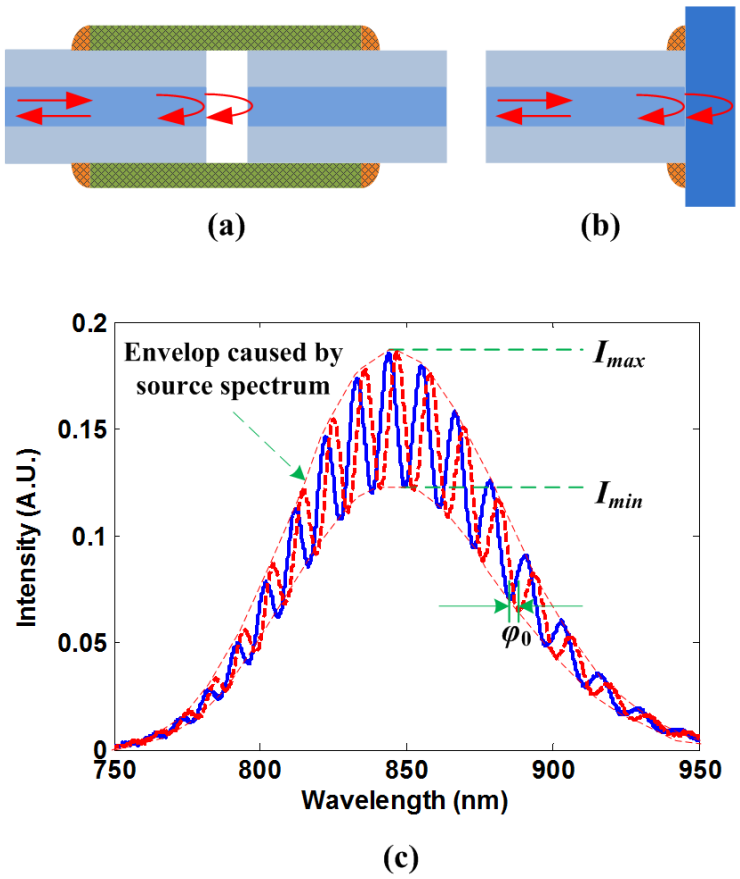

Figure 2.1. EFPI sensor schematics and spectrum. (a) EFPI sensor with air-gap cavity. (b) EFPI sensor with wafer cavity. (c) a typical sensor spectrum.

The free-space propagation of the light can either be in air or in dielectric. For the former, the two reflections are formed by two polished optical fiber ends, and the two fibers are aligned inside a capillary tube, as shown in Figure 2.1 (a). For the case of propagation in dielectrics, the excitation fiber is placed in adjacent to a (glass or sapphire) wafer, and the two reflections are generated on both sides of the wafer, as shown in Figure 2.1 (b). In both geometries, the two weak reflections possess certain phase relationship determined by the physical cavity length (e.g., optical path difference (OPD), defined as OPD = $2nL$, n is the refractive index of the dielectric (n = 1 for air) and L is the physical cavity length) and the two beams are coupled back into the lead-in fiber and interfere. The interference spectrum is then obtained to calculate the OPD encoded. A typical EFPI interference spectrum is illustrated in Figure 2.1 (c). The total phase of the sinusoid in the spectrum can be expressed as:

$$\Phi = k \cdot \mathrm{OPD} + \varphi_0 \tag{2.1}$$

In the above equation, k is the wavenumber defined as $k=2\pi/\lambda$, λ is the wavelength, and φ_0 is the additional phase we discussed in Section 1, which could cause the spectrum to shift (without a change in the density of the fringes). In Figure 2.1(c), the red dashed curve and the blue solid one have a phase difference of $\pi/2$. By identifying the maximum and minimum intensities in the fringe, the fringe visibility (FV) is calculated as:

$$\mathrm{FV} = \frac{I_{\max} - I_{\min}}{I_{\max} + I_{\min}} \tag{2.2}$$

2.2.2 The EFPI spectrum

Before proceeding to the theory, we will briefly introduce the physical model representing the subject matter. We will focus on EFPI structures with air-gap cavities (as shown in Figure 2.1 (a)), and the conclusion can be easily extended to a wafer-based cavity (see 2.3.5). For sensor geometry illustrated in Figure 2.1 (a), if the distance between the two reflective surfaces is sufficiently long, and the divergence angle of the optical beam is sufficiently large, light can reach the inner wall of the capillary tube and be partially reflected. In this regard the light propagation can no longer be treated as "free space", but rather partially guided, which tend to significantly complicate the analysis. In light of the above considerations, we will avoid such complications by applying the model illustrated in Figure 2.2.

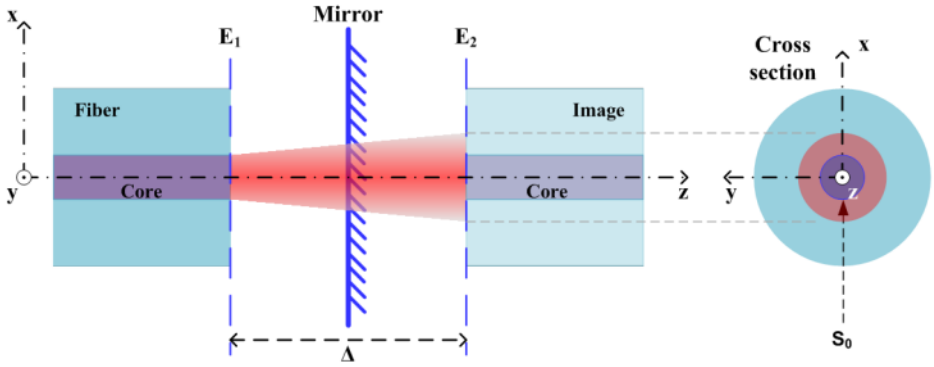

Figure 2.2. Schematic of the optical fiber low-finesse EFPI.

In the model, one of the two reflections is generated by the fiber- air interface and the other by an infinite mirror in the x-y plane with the same reflectivity; the two mirror

surfaces are perpendicular to the fiber axis (z axis). In the FP cavity, light propagates in +z direction, after getting reflected by the mirror, it propagates in the –z direction for the same distance and is re-coupled back into the lead-in fiber. This whole process is physically equivalent to the case in which the reflected light keeps propagating in free space along +z direction for another cavity length, $\Delta/2$, and couples into an image fiber whose axis is aligned with the lead-in fiber (this equivalence does not strictly hold in terms of the intensity and phase of the light, this will be addressed during the following mathematical deduction). The propagation distance inside the cavity is thus the OPD of the interferometer, and is denoted as Δ. We denote the electric field at the first fiber end plane with complex amplitude E_1 and that at the second plane (image fiber end-face) with E_2. In the following analysis, all fields are treated as scalar wave functions as in most diffraction problems. Such an approximation is adequate for the model considered[61] and from now on we neglect the influence of the light polarization. Because for the current study we only care about the relative intensity, in order to simplify the mathematical expressions we take out a constant ($1/2\eta$, η being the vacuum impedance) from the expressions for optical intensity. For the sake of simplicity without losing its generality, the mirror is assumed to have the same reflectivity as the fiber end-face, we also neglect the power loss due to the Fresnel reflection at the fiber end-face (such an approximation will introduce some calculation error, which can be easily compensated, see discussion below. As in Ref [15], we adopt this approximation for the clarity and simplicity of the mathematical expressions), thus the two interfering fields become rE_1 and rE_2, where r is the field reflectivity. For the same reason stated above, we take out the constant r and consider the interference between E_1 and E_2.

The detected power is the intensity on the fiber end-face integrated over the fiber core area S_0, and can be expressed as

$$P = \iint_{S_0} \left(E_1 + E_2\right)^* \left(E_1 + E_2\right) ds \tag{2.3}$$

The integration in Eq. 2.3 can be split into four terms,

$$\iint_{S_0} E_1 E_1^* ds = P_1 \tag{2.4.1}$$

$$\iint_{S_0} E_2 E_2^* ds = \nu P_1 \tag{2.4.2}$$

$$\iint_{S_0} E_1 E_2^* ds = \iint_{\infty} E_1 E_2^* ds \tag{2.4.3}$$

$$\iint_{S_0} E_2 E_1^* ds = \left(\iint_{S_0} E_1 E_2^* ds \right)^* \tag{2.4.4}$$

In the above expressions, P_1 denotes the reflected power by the fiber end-face, v is the power coupling coefficient into the mirror fiber. We substitute the integration region S_0 with infinity in Eq. 2.4.3 because E_1 is approximated as only present in the fiber core.

We define the plane of the fiber end-face to be $z = 0$, and the plane of the image fiber end-face to be $z = \Delta$, for the following derivation we confine our calculation to a monochromatic wave with wavevector k, and expand the field E_1 as the superposition of plane waves (2-D Fourier-transform)

$$E_1(x, y, 0) = \iint E(k_x, k_y) \cdot \exp\left[i\left(k_x x + k_y y\right)\right] dk_x dk_y \tag{2.5}$$

In the above expression, k_x and k_y are the x and y components of the wavevector. Explicit expression of the field at the $z = \Delta$ plane stems from the diffraction of E_1 to the $z > 0$ free space (considering propagation along the z axis) [62]

$$E_2(x, y, \Delta) = \iint E(k_x, k_y) \cdot \exp\left[i\left(k_x x + k_y y - k_z \Delta - \pi\right)\right] dk_x dk_y \tag{2.6}$$

where $k_z = \sqrt{k^2 - k_x^2 - k_y^2}$ is the z component of the wavevector and the phase delay π arises from the reflection from the second mirror. Inserting Eq.2.5 and Eq.2.6 into Eq.(2.4.3), we obtain

$$\iint_{\infty} E_1 E_2^* ds = \iint\iint\iint E(k_x, k_y) E^*(k_x', k_y') \cdot$$

$$\exp\left\{ i\left[\left(k_x - k_x'\right) x + \left(k_y - k_y'\right) y + k_z \Delta + \pi \right]\right\} dk_x dk_y dk_x' dk_y' dx dy \tag{2.7}$$

Notice that the integrations over x and y are performed in the entire infinite plane, and the following equation should hold to simplify the integration in Eq.2.7

$$\int_{\infty} \exp\left[i\left(k_{\mu} - k_{\mu}'\right)\mu \right] d\mu = \delta\left(k_{\mu} - k_{\mu}'\right) \tag{2.8}$$

where $\mu = x$, y and $\delta(x)$ denotes the Dirac delta function. Inserting Eq.2.8 into Eq. 2.7 gives

$$\iint_{\infty} E_1 E_2^* ds = \iint \left| E\left(k_x, k_y\right) \right|^2 \cdot \exp\left[i\left(k_z \Delta + \pi\right) \right] dk_x dk_y \tag{2.9}$$

Combining Eq.2.9 and Eq.2.4.4 results in

$$\iint_{S_0} \left(E_1 E_2^* + E_2 E_1^* \right) ds = -2 \iint_{\infty} \left| E\left(k_x, k_y\right) \right|^2 \cdot \cos\left(k_z \Delta\right) dk_x dk_y \tag{2.10}$$

The integration in Eq. 2.10 is in the k-space Cartesian coordinate. We then convert it to integration in the polar system and further integrate over k_φ to remove the azimuthal dependence on φ (φ denotes the angle between the polar vector and the x-axis) as long as mathematical separation of variables between k_r and k_φ holds (which is a reasonable assumption for most cases). Also bear in mind that the square of the absolute value of the E-field gives the intensity

$$\iint_{S_0} \left(E_1 E_2^* + E_2 E_1^* \right) ds = -2 \int I\left(k_r\right) \cdot \cos\left(k_z \Delta\right) k_r dk_r \tag{2.11}$$

In the above equation, $I(k_r)$ can be interpreted as power density distribution projected onto the radial direction (i.e., spatial density distribution projected onto the x-y plane), by using the relationship $k_r^2 + k_z^2 = k^2$, the integration over k_r can be converted to integration over k_z; by combining Eq.2.11 with Eqs. (2.4.1~2.4.2), the total received power can be expressed as:

$$P = \left(1 + \nu\right) P_1 - 2 \int_0^k I\left(k_z\right) \cdot \cos\left(k_z \Delta\right) k_z dk_z \tag{2.12}$$

In Eq. 2.12, $I(k_z)$ is the optical power density distribution along the fiber axis (z) in the FP cavity (not in the fiber). Eq. 2.12 is the general expression for the received power. Before

stepping forward to calculate the fringe visibility and additional phase in the interferogram, it is interesting to explore the physical message encoded in this equation.

If the optical beam inside the FP cavity has a sufficiently small divergence angle, such that $I(k_z)$ is distributed over a very narrow k_z range, Eq. 2.12 can be simplified as

$$P(\Delta) = C_0 \int_0^\infty I(k_z)\left[1-\cos(k_z z)\right] dk_z \tag{2.13}$$

with C_0 being a constant. The second term on the right-hand-side of Eq. 2.13 shows the Fourier cosine transform relationship between the power density distribution of a monochromatic light projected onto the z axis and the OPD dependent output power from the low-finesse EFPI. It manifests the Fourier cosine transform relationship between the spectral density distribution and the output intensity from a Michelson interferometer, which is the basis for Fourier-transform spectroscopy[63]. Eq.2.13 can be regarded as a k-domain counterpart of the Wiener-Khintchine theorem.

Eq. 2.12 can be written as

$$P(\Delta) = (1+v)P_1 - 2\int_0^k I(k_z)\cdot\cos\left((k_z-k)\Delta + k\Delta\right)k_z dk_z \tag{2.14}$$

After expanding the cosine term in the above integration and some mathematical rearrangement, the spectrum obtained from the EFPI is expressed as

$$P(\Delta) = Q(\Delta)\left[1+\frac{\sqrt{C^2(\Delta)+S^2(\Delta)}}{Q(\Delta)}\cos\left(k\Delta+\theta(\Delta)+\pi\right)\right] \tag{2.15}$$

In the above equation

$$\theta(\Delta) = \tan^{-1}\left(-\frac{C(\Delta)}{S(\Delta)}\right) - \frac{\pi}{2} \tag{2.16}$$

is the additional phase term stems from the optical beam free space beam propagation, the fringe visibility of the spectrum $FV(\Delta)$ is expressed by

$$FV(\Delta)=\frac{\sqrt{C^2(\Delta)+S^2(\Delta)}}{Q(\Delta)} \tag{2.17}$$

in which

$$C(\Delta)=2\int_0^k I(k_z)\cdot\cos\left((k_z-k)\Delta\right)k_z dk_z \tag{2.18}$$

$$S(\Delta)=2\int_0^k I(k_z)\cdot\sin\left((k_z-k)\Delta\right)k_z dk_z \tag{2.19}$$

$$Q(\Delta)=(1+\nu)P_1 \tag{2.20}$$

It is interesting to compare the result in Eq. 2.15 with the calculated spectrum from a Michelson interferometer used as a Fourier-transform spectrometer in [61], where the source spectral distribution was treated by considering the fringe induced by each monochromatic spectral component and adding up the interference pattern generated by each component incoherently. Similarly, Eq.2.12 inherently suggests the same physics for an optical source with certain spatial power density distribution (divergent from unidirectional): the overall interference spectrum is the incoherent superposition of the interference patterns generated by individual plane wave components with different propagation directions. Surprisingly, the fringe visibility shown in Eq. 2.17 depends neither on spatial nor on spectral coherence, as one may expect that the visibility would decrease as the degree of coherence drops. In other words, the conclusion drawn here is in contradiction to our common sense: intuitively, the fringe visibility should be larger for EFPIs illuminated by a highly coherent laser than for those excited by a incoherent broadband source; also the visibility should be larger for light with higher spatial coherence (such as a single mode fiber) than light which is nearly incoherent spatially (such as highly multimode fiber); however, in reality the fringe visibility is solely determined by the working wavelength and spatial power density distribution (projected onto *z* axis) as shown in Eq. 2.17. It is predicted possible that a SMF-EFPI illuminated by a highly coherent laser can have less fringe visibility than a MMF -EFPI illuminated with a halogen light bulb, as is experimentally demonstrated in 2.3.4.

2.2.3 Calculation of $I(k_z)$

The fringe visibility and additional phase are shown to be determined by the power density distribution projected onto z axis (Eqs.2.15~2.19). Notice that the "distribution projected onto z axis" subjects to a monochromatic light (with a fixed wavenumber k); light with a different wavelength may have a different z-distribution, thus the fringe visibility and additional phase are wavelength-dependent, as will be demonstrated in 2.3.3. In order to calculate the fringe visibility and additional phase according to Eq. 2.17 and Eq. 2.16 respectively, the $I(k_z)$ distribution needs to be determined in advance. Calculation of $I(k_z)$ employs different approaches for SMF-based and MMF-based EFPIs.

$I(k_z)$ calculation for SMF-EFPI

For a typical SMF, the field distribution on the fiber cross section can be well-approximated as a Gaussian[64]

$$E(x,y) = \exp\left[-\left(x^2+y^2\right)/w_0^2\right] \tag{2.21}$$

where w_0 denotes the mode field radius of the fiber. The 2-D Fourier-transform of Eq. 2.21 can be readily obtained as

$$E\left(k_x,k_y\right) = \frac{w_0^2}{8\pi^2}\exp\left[-w_0^2\left(k_x{}^2+k_y{}^2\right)/4\right] \tag{2.22}$$

By inserting the relationship $k_z^2 = k^2 - \left(k_x{}^2+k_y{}^2\right)$ into Eq.2.22, we get the $I(k_z)$ distribution as

$$I\left(k_z\right) = I_0\exp\left[-w_0^2\left(k^2-k_z^2\right)/2\right] \tag{2.23}$$

where I_0 is a constant, k is the wavenumber, and k_z is in the range between 0 to k.

$I(k_z)$ calculation for MMF-EFPI

For MMF-based EFPI, analytical expression for $I(k_z)$ is extremely difficult to obtain. With hundreds, even thousands of modes being excited, accurate calculation of the relative intensity and phase of each mode can be too complex to be practical. One can assume the absolute value of the general field profile to be approximated by a well-

defined function (e.g., a Gaussian as in the SMF case), but calculating the Fourier-transform is also impractical due to the unknown phase profile across the fiber end-face. Fortunately, only the power density distribution (instead of the field distribution) is needed for the calculation of the fringe characteristic, and this power distribution can be directly calculated by measuring the output angular power distribution, as shown in Figure 2.3.

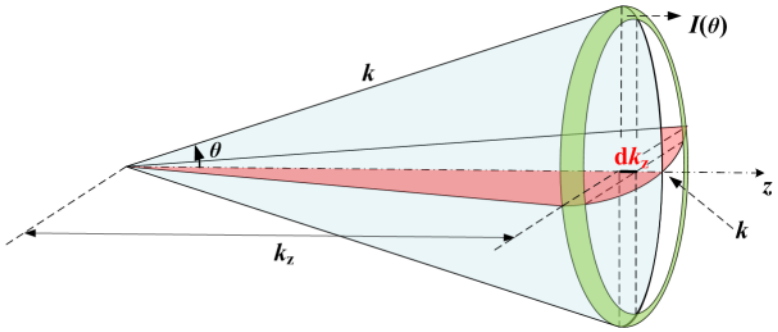

Figure 2.3. Conversion schematic from angular power density distribution to the k_z density distribution. The total power distributed from k_z to k_z+dk_z is equal to the power flux in the ring area (in green color) defined by divergence angle from θ to θ + dθ.

As shown in Figure 2.3, light with k_z component falling within the range between k_z to k_z+dk_z has total power of

$$I\left(k_z\right)dk_z = 2\pi \cdot k \cdot I\left(\theta\right)dk_z \tag{2.24}$$

with $I(\theta)$ being the power density distribution with respect to divergence angle θ. Eq.2.24 directly leads to the following relationship between the power density distribution projected onto the z axis and along θ direction

$$I\left(k_z\right) = 2\pi k \cdot I\left(\theta\right) = 2\pi k \cdot I\left[\text{acos}\left(k_z/k\right)\right] \tag{2.25}$$

Eq.2.25 demonstrates that the $I(k_z)$ distribution can be obtained by the knowledge of the angular distribution $I(\theta)$, as will be shown in 2.3.3; $I(\theta)$ can be determined by measuring the optical far field power distribution of the multimode fiber.

2.2.4 Wafer-based EFPI

The modeling of the dielectric wafer cavity shown in Figure 2.1 (b) is similar to the air-gap cavity, however several modifications need to be made. When light enters the dielectric material with refractive index n, the total wavenumber is modified from $k = k_0$ (k_0 being the vacuum wavenumber) to $k = nk_0$. The transversal wavenumbers k_x and k_y conserve when entering the wafer, leading to a modified value of k_z: $k_z|_{wafer} = [(nk_0)^2 - k_x^2 - k_y^2]^{1/2}$.

In order to measure $I(k_z)$, the angular power distribution of the field emanating from the fiber is measured (denoted as $I(\theta)$). Because typically the measurement is made by a beam profiler, the $I(\theta)$ distribution is characterized in air. For the air-gap cavity, to map $I(\theta)$ to $I(k_z)$, one needs only to determine a set of angles $\theta_{kz} = \cos^{-1}(k_z/k)$, and subsequently do an interpolation $I(k_z) = \text{interp}(\theta, I(\theta), \theta_{kz})$, where interp() denotes interpolation.

A modification is required when applying the above $I(k_z)$ characterization process for the wafer-based EFPI. Within the dielectric wafer, the angular distribution is changed according to:

$$\theta_{wafer} = \sin^{-1}\left(\frac{1}{n}\sin\theta_{air}\right) \tag{2.26}$$

as required by the Snell's law. This has significant influence on the fringe visibility, as will be discussed in the next section. Because of this "focusing" effect described in Eq. 2.26, the power distribution $I(k_z)$ tends to concentrate better towards $k_z = k$. Such a focus-induced-concentration dictates an increased fringe visibility at larger OPD values through the Fourier-like transformation in Eqs. 2.18~2.19.

For the air-gap cavity, only two reflections contribute to the interference spectrum. The "incoherent" power contribution is expressed in Eq. 2.20 and the information-bearing term is encoded with the cosine "coherent" term. For the wafer cavity, there will be an additional reflection from the lead-in fiber's end face. Typically the fiber is place in close vicinity to the wafer, so the coupling loss within the region formed by fiber and wafer is

neglected; for MMF-EFPI, the critical parallelism between the fiber end face and the wafer required to generate significant interference is mostly unsatisfied. The above conditions lead to the following treatment of the additional reflection: only another P_1 is incoherently added to Eq. 2.20, resulting in

$$Q(\Delta) = (2 + \nu) P_1 \tag{2.27}$$

The above model sets the upper limit of the fringe visibility given a certain excitation condition (as dictated by $I(k_z)$). In real practice, the visibility is expected to be less due to imperfection such as non-parallelism and additional reflections in the optical link.

2.3 Results and discussion

2.3.1 Air-gap SMF-EFPI: simulation and experimental results

Figure 2.4 shows the experimental setup to measure the fringe visibility curves for both SMF and MMF-EFPIs. The two reflections of the low-finesse Fabry-Perot interferometer were formed by a polished distal end of the lead-in fiber and an optical-quality surface on a silica pentaprism. We chose the pentaprism to eliminate the back-reflection from the far-end, which might affect the measurement accuracy of the fringe visibility. Parallelism of the two surfaces forming the FP cavity was guaranteed by maximizing the fringe visibility at a given cavity length; tuning of the mirror angles was achieved by two rotation stages in perpendicular planes, as shown in Figure 2.4. Two types of fibers were used in the experiment: Corning SMF-28 standard single mode fiber and Nufern UHNA7 ultra-high NA single mode fiber. Light from a highly-coherent tunable laser (coherent length ≈ 30 cm, tuning range from 1520 nm to 1570 nm) was coupled into the lead-in fiber via a fiber circulator, and the reflected interference signal was sent to the spectrometer through the same circulator. The spectrometer used was the high precision Component Testing System (*Si-720,* Micron Optics, Inc.), spectral resolution rating of the instrument was below 5 pm. During the measurement, the cavity length of the FP interferometer was adjusted using a one-dimensional translation stage; fringe visibility at 1550 nm was calculated at each cavity length (OPD), the cavity length was calculated based on the interferogram with estimated accuracy well below 50nm[27].

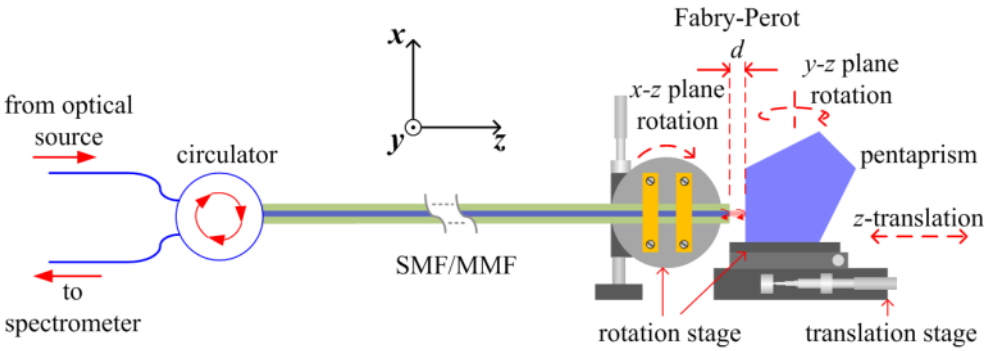

Figure 2.4. Experimental setup for measurement of the fringe visibility curve. Parallelism of the two reflection surfaces are guaranteed by tuning the two rotation stages, and the cavity length can be finely tuned by a 1-D translation stage.

The visibility measurement results for both types of single mode fibers are plotted in Figure 2.5; also plotted in the same figure are the simulation results. For the simulation we used Eq. 2.17 to calculate the visibility; prior to the visibility calculation, $I(k_z)$ was determined using Eq. 2.23. The value of the unknown parameter w_0 (fiber mode field radius) in Eq.2.23 was adjusted during the simulation to acquire best agreement with experiment. The mode field radii calculated for SMF-28 and UHNA7 fibers were 4.9 and 1.7 μm, respectively; they agreed well with their corresponding specifications, which were 5.2+/-0.4 μm and 1.6 +/- 0.15 μm. In Figure 2.5, circles and dots are experimental data; solid and dashed curve are simulation results. The discrepancy between the theoretical (solid) and experimental (circle) data for SMF-28 fiber at shorter OPD is attributed to the error induced by the Fresnel reflection loss at the two F-P mirror surfaces; a theoretical curve with the loss considered is plotted in the figure for comparison, which shows better agreement with experiment. The sensitivity of the fringe visibility to the mode field diameter of the input fiber suggests potentially a novel method to characterize the mode field diameter of single mode fibers: by characterizing the visibility curve, w_0 can be calculated by fitting the experimental data using Eqs. 2.17 and 2.23.

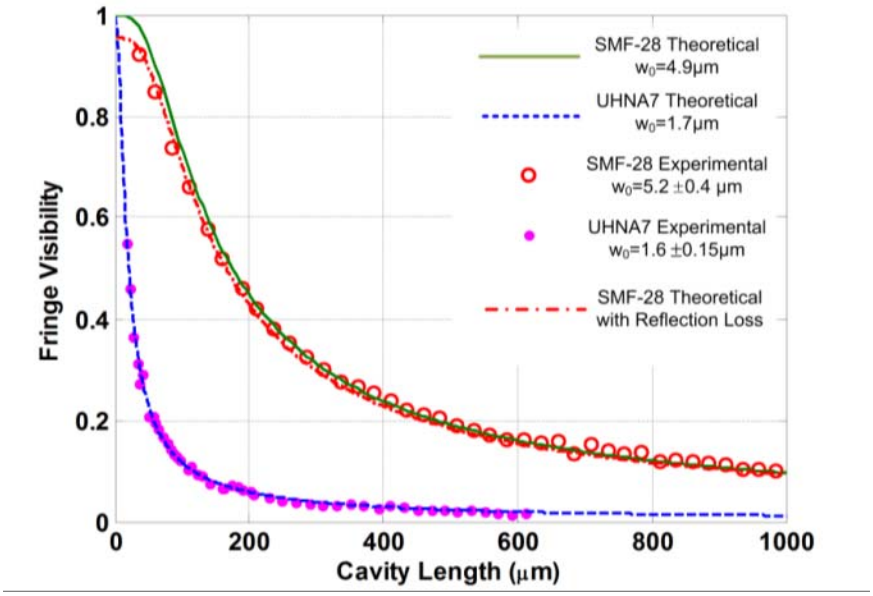

Figure 2.5. Fringe visibility plotted as a function of FP cavity length. Solid and dashed curves represent simulation results, circles and dots are experimental data. The calculated mode field radii of the fibers are labeled and compared with the values in their specifications.

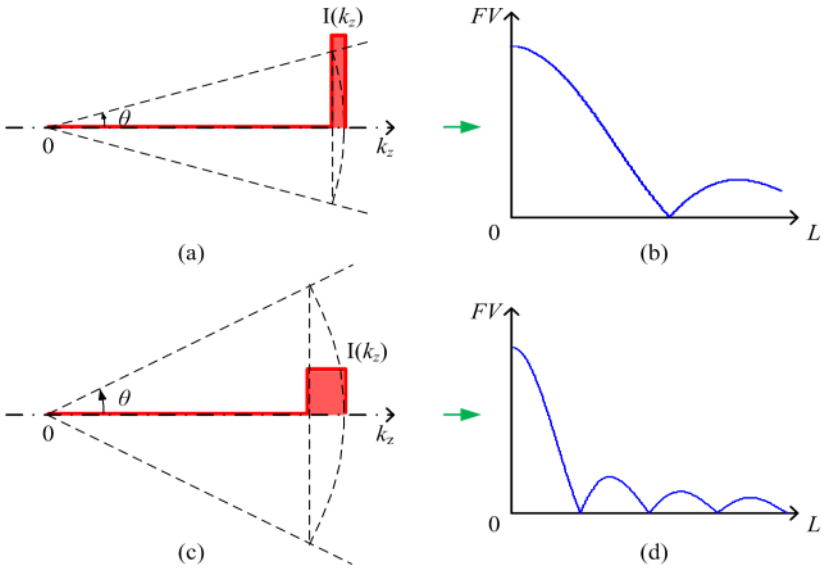

Figure 2.6. Conceptual illustration of the relationship between output divergence angle and the visibility curve. (a) I(k_z) distribution of a beam with less divergence angle. (b) Visibility curve corresponding to the distribution in (a). (c) I(k_z) distribution of a beam with larger divergence angle. (d) Visibility curve corresponding to the distribution in (c). The figures show qualitatively that the visibility curve gets broader as I(k_z) becomes sharper.

The fringe visibility of the UHNA7 fiber based EFPI drops much faster than the SMF-28 fiber based EFPI as the cavity length increases, which can be explained as follows. The high NA fiber has a smaller mode field diameter, in other words, the Gaussian profile used to approximate the field has a narrower width. With the waist of the output Gaussian beam coincides with the fiber distal end, the fiber mode field radius can be regarded as the Gaussian beam waist size. The divergence angle of the Gaussian beam is inversely proportional to its beam waist size w_0 by[62]

$$\theta = \frac{\lambda}{\pi w_0} \tag{2.28}$$

According to Eq.2.28, light divergence angle is much larger for the UHNA7 fiber than the SMF28 fiber due to its smaller waist size. A larger divergence angle leads to a broader $I(k_z)$ distribution, as shown in Figure 2.3 and Eq. 2.25. As discussed in 2.2.2, the Fourier-transform pair formed by the interferometer output power and the $I(k_z)$ distribution implies a simple relationship: the broader the $I(k_z)$ distribution, the sharper the visibility curve (means the visibility drops faster with increasing OPD). This is analogous to the case of Fourier transform spectroscopy: for optical source with higher temporal coherence, its narrower spectral density distribution results in more slowly dropping visibility. Figure 2.6 conceptually illustrates the above conclusion.

The extra phase delay θ in Eq.2.15 has also been studied using SMF-28 based EFPI. Theoretical and experimental data are provided in Figure 2.7. To calculate the phase term, Eqs.2.16,2.18,2.19, and 2.23 were employed. Notice the good agreement between the result shown in Figure 2.7 with that reported in [40], in which the phase term was attributed to free space beam propagation and re-coupling back to the fiber. Eq. 2.12 gives another physical interpretation of this extra phase shift. Plane waves (at a fixed wavelength) with different k_z components, when propagating inside the FP cavity, will experience different OPDs (thus different total phase delay) due to various divergence angles. The component normal to the reflection mirrors has no extra phase delay, but other components tend to manifest additional phase shifts depending on their injection angles; the overall effect is the superposition of all these extra phases as an effective

phase term in the total fringe pattern. In plotting Figure 2.7, when the cavity length is short, θ is difficult to be accurately measured from the fringe pattern due to signal processing limitations; whereas at longer cavity lengths, the fringe visibility is very low resulting in poor signal to noise ratio (SNR), which is responsible for the relatively large noises in the experimental data.

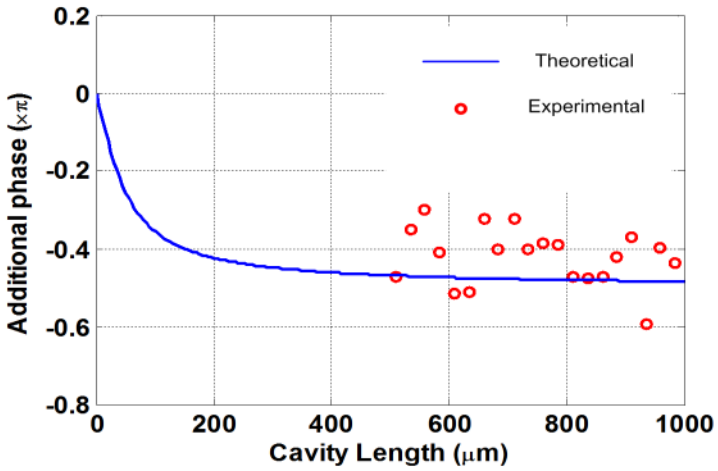

Figure 2.7. Theoretical and experimental data showing the extra phase delay of an EFPI with SMF-28 as the lead-in fiber.

2.3.2 Air-gap MMF-EFPI: comparison with previous literatures

In this subsection, multimode fiber with 'uniform mode excitation' will be studied. Under this condition, all the modes in the multimode fiber will be excited with equal power which will generate a top-hat shaped output angular distribution[50]. In reality, this condition is unlikely to occur due to mode filtering and mixing effects during wave propagation in the fiber which tends to build up a steady 'equilibrium' mode distribution[65]. However, analysis of this idealized case is important because: 1. It yields a simple analytical solution and 2. It sets a theoretical standard to characterize and compare the performances of different MMFs. Thus previous theoretical works paid considerable attention to analyze this situation[50, 51].

We will apply Eq. 2.25 with Eq. 2.17 to calculate the fringe visibility. At such excitation condition, $I(k_z)$ distribution can be expressed as

$$I(k_z)=\begin{cases}\text{constant}, & 0<\text{acos}(k_z/k)<\text{asin}(\text{NA})\\ 0, & \text{others}\end{cases} \tag{2.29}$$

When inserting Eq.2.29 into Eqs.2.17-2.20, the calculation can be dramatically simplified by assuming the beam to diverge gently (with small output angle), which helps to drop the k_z terms in the integrations in Eq.2.18 and Eq.2.19 and lead to ν=1 in Eq.2.20. Under such approximations, Eq.2.17 is transformed to

$$FV(\Delta)=\frac{\sqrt{C^2(\Delta)+S^2(\Delta)}}{P(\Delta)}=\frac{\left|\int_0^k I(k_z)e^{jk_z\Delta}dk_z\right|}{\int_0^k I(k_z)dk_z} \tag{2.30}$$

in which

$$C(\Delta)=2\int_0^k I(k_z)\cdot\cos\left((k_z-k)\cdot\Delta\right)dk_z \tag{2.31}$$

$$S(\Delta)=2\int_0^k I(k_z)\cdot\sin\left((k_z-k)\cdot\Delta\right)dk_z \tag{2.32}$$

$$P(\Delta)=2\int_0^k I(k_z)dk_z \tag{2.33}$$

The second equation in Eq.2.30 can be demonstrated by inserting Eqs.2.31-2.33 into the left hand side of the equation followed by some mathematical rearrangement. Inserting Eq.2.29 into Eq.2.30, and denoting θ_d=asin(NA) (NA is the numerical aperture of the MMF), the fringe visibility is analytically expressed as

$$FV(\Delta)=\frac{\left|\int_{k\cos\theta_d}^k e^{jk_z\Delta}dk_z\right|}{k(1-\cos\theta_d)}=\left|\text{sinc}\left(\frac{\phi}{2}\right)\right| \tag{2.34}$$

where $\phi = \frac{k\Delta\left(1-\cos\theta_d\right)}{2}$, Δ is the OPD of the FP cavity. Eq. 2.34 is in complete agreement with Eq.8 in Ref.[50], the deduction of which is based on ray-optics. Eq. 2.34 predicts that under 'uniform mode excitation' condition, the visibility curve is solely determined by the numerical aperture of the fiber. In Ref.[51], the authors analyzed three types of fibers, whose parameters are listed in Table 2.1.

Table 2.1. MMF Parameters[a].

Parameter	Fiber		
	1	*2*	*3*
$2a$ (μm)	100	50	50
n_1	1.448	1.448	1.448
n_2	1.440	1.416	1.440
NA	0.15	0.30	0.15
V number	30.80	30.68	15.40

[a]Numbers obtained from Appl. Opt. 43,4659 (2004)

Fiber 1 and 3 have the same NA but fiber 1 has a much larger mode volume; fiber 1 and 2 have similar mode volumes, but the NA of fiber 2 is twice that of fiber 1. Computer simulation results based on the exact mode analysis [51] and based on Eq.3.34 are compared in Figure 2.8. It is clearly shown that the results from the two theories agree well, except little discrepancies due to inaccuracy of Eq.2.34 induced by the approximations. The fringe visibility for Fiber 2 drops much faster than Fiber 1 and 3 cases due to its larger NA; in contrast, the visibility curve is not affected directly by mode volume. Although Fiber 1 has a much larger mode volume, its fringe visibility appears to be similar to that of Fiber 3; Fiber 2 shows much worse fringe visibility compared to fiber 1, yet they have similar mode volumes.

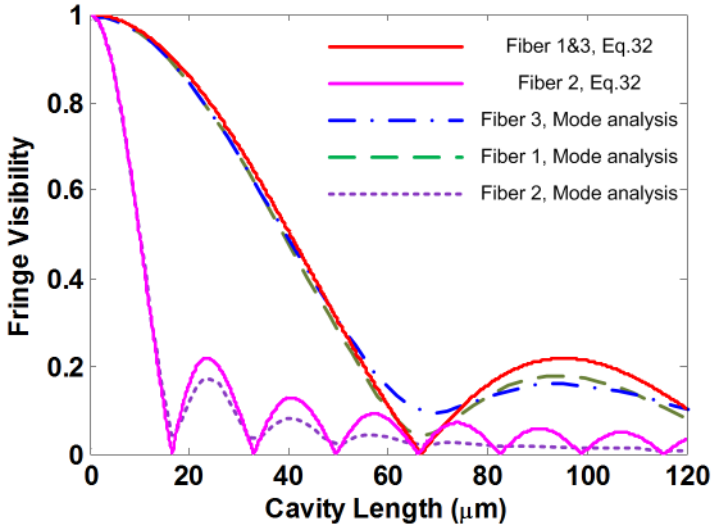

Figure 2.8. Fringe visibility versus FP cavity length for fiber 1,2 and 3, all modes are equally excited. Simulation is based on Eq.3.34 and the fiber mode analysis method in [51].

2.3.3 Air-gap MMF-EFPI: simulation and experimental results

We use the system configuration shown in Figure 2.4 for the measurement of the fringe visibility of MMF-EFPIs. A fiber coupled thermal light source (HL-2000 Tungsten Halogen Source, Ocean Optics, Inc.) with broadband incoherent radiation was used to illuminate a multimode fiber (MM-S105/125-22A, Nufern) with core diameter of 105μm and NA=0.22. We used a 50/50 MMF coupler (MMF:100 μm core, 0.29NA) to replace the circulator, the extra arm of the coupler was immersed in refractive index matching fluid for anti-reflection. The signal from the EFPI was recorded using an Optical Spectrum Analyzer (AQ6315A, Ando Electric Co., Ltd.) with spectral resolution set to 1 nm; the fringe visibilities at 800nm, 1200nm and 1550nm were measured.

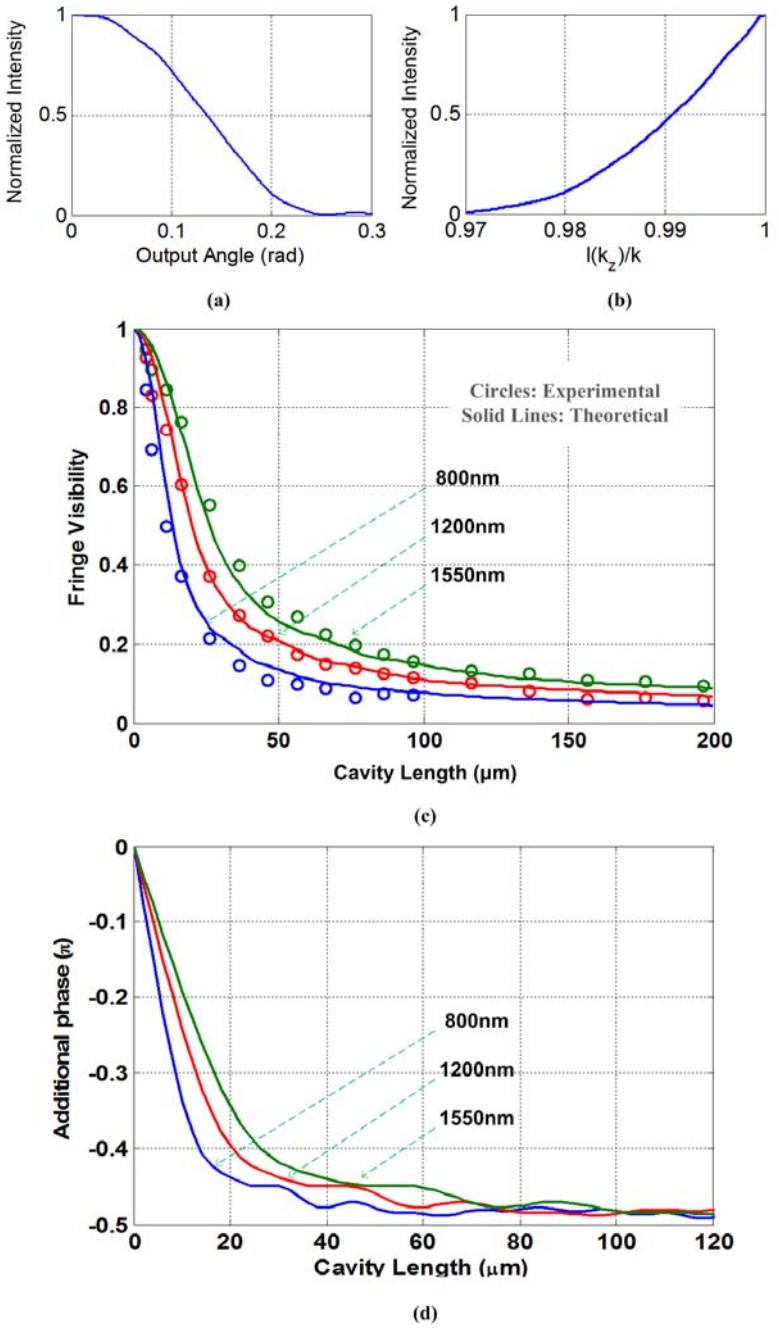

Figure 2.9. Theoretical and experimental results of the fringe visibilities and additional phases versus OPD for MMF-EFPI. MMF has core diameter 105μm and NA=0.22. (a) Measured angular distribution. (b) Calculated I(k_z) distribution based on (a). (c) Fringe visibility versus OPD curve for 800nm, 1200nm and 1550nm light, theoretical and experimental. (d) Additional phase θ versus OPD for 800nm, 1200nm and 1550nm light, theoretical.

Due to mode filtering and mixing, the uniform mode excitation condition discussed in 2.3.2 is rarely satisfied in reality; instead, the power distribution among the excited modes tends to stabilize during propagation, establishing an equilibrium mode distribution, and creating a far-field intensity distribution similar to a Gaussian. However, assuming the angular distribution as Gaussian and use Eq. 2.25 to calculate $I(k_z)$ leads to large errors in the calculated fringe visibility. In fact, the fringe visibility curve is very sensitive to the shape of the angular intensity distribution; as a result, we used measured angular distribution to deduce $I(k_z)$, based on which the fringe visibility was calculated.

In order to measure the angular distribution, we measured the far-field intensity distribution using a beam profiler (BP104-IR, Thorlabs, Inc.), the linear intensity distribution was then mathematically converted to angular distribution by characterizing the distance between the fiber distal end and the profiler; the $I(k_z)$ distribution was then calculated using Eq.25, fringe visibility was then calculated based on $I(k_z)$ and Eqs.2.17-2.20. In Eq.2.20, light coupling coefficient ν was calculated by[66]

$$\nu = a^2 \Big/ \left(a + \Delta \cdot \tan \theta_d \right)^2 \tag{2.35}$$

where a is the fiber core radius, and Δ and θ_d are defined in Eq.2.34. The measured angular distribution, measured $I(k_z)$ distribution and the calculated/measured fringe visibility curves are plotted in Figure 2.9 (a)-(c) respectively. Figure 2.9 (c) demonstrates a good agreement between the theory and experiment. The calculated additional phases (based on Eq.2.16) for the three wavelengths were plotted in Figure 2.9 (d). Due to the insufficient SNR in the experiment, we were unable to provide reliable measurement results for the additional phase. From the results, it is interesting to note that both the fringe visibility and the additional phase are dependent on wavelength. This is a natural outcome due to the fact that $I(k_z)$ varies with wavelength. The same principle shown in Figure 2.6 also applies here: longer wavelength corresponds to narrower $I(k_z)$ distribution, which implies broader fringe visibility curve.

2.3.4 Relationship with degree of coherence

The most distinctive and important conclusion of the theory developed in this chapter is that the fringe visibility of a fiber optic EFPI is determined by the power density distribution projected onto the z axis ($I(k_z)$ distribution) and the working wavelength. Temporal and spatial coherences of the illumination light, however, do not affect the fringe visibility.

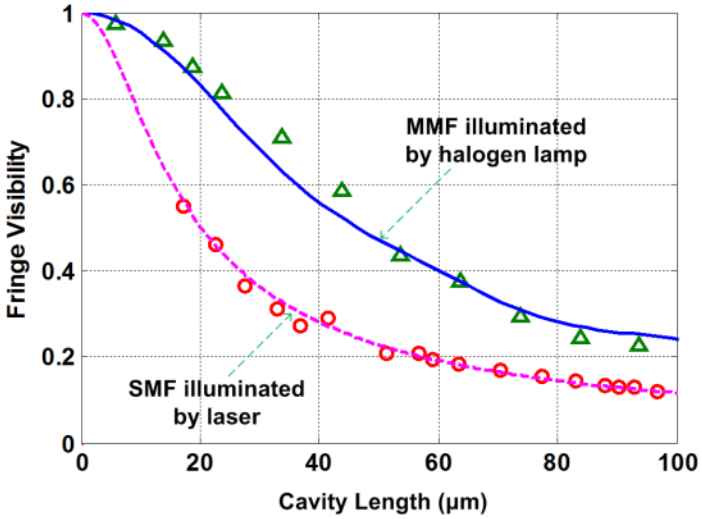

Figure 2.10. Comparing the fringe visibility curves of two EFPIs. Due to its smaller output divergence angle, an MMF-EFPI illuminated by halogen lamp shows better fringe visibility than a SMF-EFPI illuminated by a highly-coherent laser.

Figure 2.10 shows the fringe visibility versus OPD curves for two types of EFPIs, both working at 1550nm. The first type is a single mode fiber based EFPI (SMF: UHNA7, Nufern), illuminated with a tunable laser whose coherent length is over 30cm (built-in fiber laser from the Component Testing System, Si-720, Micron Optics Inc.). The second is based on a multimode fiber (MM-S105/125-12A, Nufern) with core diameter of 105μm and NA=0.12. The mode volume of the fiber is estimated as ~240 at 1550nm. The fiber was illuminated using a fiber-coupled halogen lamp (HL-2000 Tungsten Halogen Source, Ocean Optics, Inc.). The first EFPI configuration had perfect temporal and spatial coherences, while the second configuration was regarded as incoherent both temporally

and spatially. However, due to the larger output divergence angle, the fringe visibility of the first EFPI was worse.

We also envision some potential applications and engineering impacts rest on the theory. The transform pair formed by the k_z distribution and the interferometer output enables us to characterize the output mode profile of an optical fiber by measuring the output intensity from a FP interferometer formed by the fiber endface and another partial reflection mirror. For example, for SMF, by fitting the visibility curve shown in Figure 2.5, the mode field diameter of the fiber can be calculated at principally any wavelength above cutoff given the capability to measure the fringe visibility at that wavelength. For MMF, the visibility curve was observed to be very sensitive to the far-field intensity distribution of the fiber. Fitting the visibility curve thus provides an alternative means to characterize the output pattern of the fiber at any given wavelength.

The theory also implies some major considerations for optical fiber EFPI sensing system design. In order to have higher fringe visibility (higher SNR), the output divergence angle of the fiber needs to be decreased, either by reducing the NA or suppressing higher-order modes in the fiber; longer working wavelength also helps to increase the fringe visibility. For applications with critical SNR requirements, the near infrared range would be a better choice for sensing system design. For most EFPI sensor geometries, the OPD change within the full measurement range will not be large. The model also dictates that the additional phase shift will always stay within [-π/2,0] for both MMF-EFPIs and SMF-EFPIs, which initiates the hope for complete elimination of the signal demodulation jumps [60].

2.3.5 Results for wafer-based EFPI

The air-gap EFPI was investigated in the previous subsections, where the theoretical fringe visibility curve (fringe visibility plotted against OPD) showed good agreement with experimental results. In this subsection, the results for wafer-based EFPIs will be presented. MMF-EFPIs are investigated because a practical model has already existed for SMF-EFPIs [40].

Silica MMF excitation

The silica fiber used in the experiment was a five meter long 0.22 NA MMF (AFS105/125Y, Thorlabs, Inc.). The optical source was a 850 nm light-emitting diode (LED), and a beam profiler (BP 104-VIS, Thorlabs, Inc.) was used to capture the far field power distribution. In calculating the fringe visibility curve, the refractive index of the wafer cavity was assumed to be 1.77 (representing sapphire). Figure 2.11 (a) shows the measured angular distribution of the output beam. The distribution resembles a Gaussian as a result of mode equilibrium, instead of being a top-hat shape. Figure 2.11 (b) shows the calculated FV curve, according to the measured power distribution. Two features are distinctive for the wafer cavity: 1) due to the incoherent contribution of the fiber end face reflection, the fringe visibility is less than unity at OPD equals to zero, in contrast to the air-gap cavity. 2) At larger OPD, the visibility of the wafer cavity drops much slower, resulting in higher fringe visibility. This is a natural manifestation of the focusing effect described in Eq. 2.26.

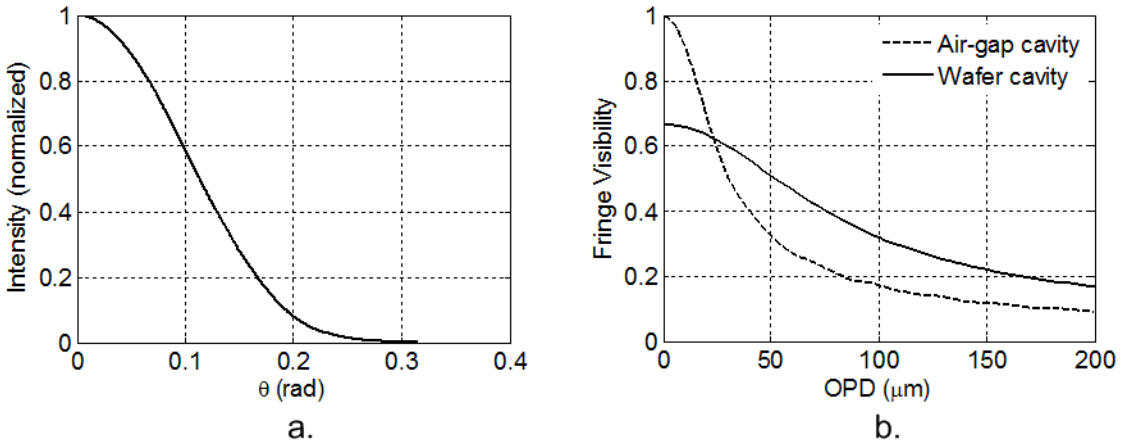

Figure 2.11. Visibility curve calculation: (a) Measured beam angular distribution from a 0.22 NA silica fiber. (b) Calculated fringe visibility for both air-gap and wafer FP cavities based on the characterized angular distribution.

Sapphire fiber excitation

Fiber-optic sensors based on silica fibers generally work below 1000^{o}C due to thermal diffusion of the dopant and degraded mechanical integrity associated with the high temperature. Single-crystal optical fibers have demonstrated favorable optical and mechanical properties under harsh environment, e.g., a sapphire wafer EFPI excited with

a single-crystal sapphire fiber was tested to 1600°C without observable signal degradation [14]. Such single-crystal fibers are typically cladding-less fibers (optical guidance is supported by air cladding), resulting in extremely high mode volume (e.g., for a 75μm diameter sapphire fiber the V number at 850 nm is ~400, resulting in a mode volume ~66000). The large number of excited modes impose tremendous computational complexity if exact fiber modal analysis ([51]) is to be employed, rendering such an approach unpractical. The ray-optics-based approach [50], on the other hand, is over simplified in which fiber mode mixing and filtering are completely neglected, and could only be applied when the output angular distribution resembles a top-hat shape (a condition rarely satisfied in real applications).

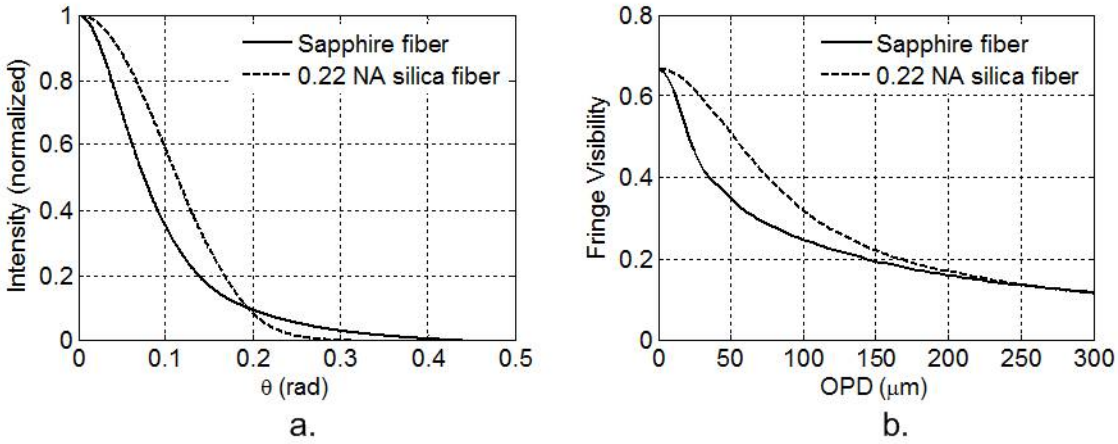

Figure 2.12. Visibility curve calculation: (a) Comparison of measured beam angular distribution from a sapphire fiber and a 0.22 NA silica fiber. (b) Fringe visibilities of a sapphire wafer EFPI with sapphire fiber and 0.22 NA silica fiber excitations, calculated based on the characterized angular distribution in (a).

The theory is extremely powerful in modeling the sapphire fiber based EFPI, as the only required input parameter is the far field power distribution. Once the distribution is obtained, it is inserted into Eqs. 2.15~2.20 to directly predict the fringe visibility and additional phase in the spectrum at a given OPD value. Figure 2.12 (a) compares the measured angular distribution of light outputting from a sapphire fiber (75 μm thick, 50 cm long, excited by a 105/125 μm 0.22 NA silica fiber) and a 105/125 μm 0.22NA silica fiber. It should be noted that the distributions exhibit significant differences: the silica fiber has a bell-shape (Gaussian) angular distribution with a cut-off at ~0.25, representing

its numerical aperture. The sapphire fiber, having a NA > 1 (full angle acceptance) and excited by the 0.22NA fiber, shows a significantly modified angular distribution, with both concentration towards small angle and extension into larger angles. The power redistribution exhibited by the sapphire fiber is a manifestation of strong mode mixing and filtering within the waveguide. The difference in the angular distribution results in slight divergence of the fringe visibility curves, as shown in Figure 2.12 (b).

2.3.6 Influence on WLI-based signal processing

As shown in Eq. 2.16, the additional phase term in the spectrum is a function of OPD, instead of being a constant as assumed in many WLI-based signal processing algorithms. Assuming a constant phase, while in reality it is not would eventually lead to abrupt demodulation jumps. A similar case has been analyzed for intrinsic FP interferometers (see 3.4.2, 4.2.2). This implies one must be very careful when making the constant phase assumption to avoid the demodulation jumps. As will be discussed in the following two subsections, the constant additional phase assumption is theoretically safer for the air-gap EFPI than the wafer-based EFPI.

Air-gap EFPI

With the measured angular distribution, the additional phase at any given OPD is straightforwardly calculated from Eq. 2.16. Using an air-gap EFPI excited by the 0.22 NA MMF (AFS105/125Y, Thorlabs, Inc.) whose output angular distribution is depicted in Figure 2.11 (a), the additional phase evolution as a function of OPD is plotted in Figure 2.13 (a), solid curve. The measured additional phase was drawn in the same plot as triangles. It is observed that for EFPI, as long as the OPD change stays small during the full measurement range, the change of the additional phase is negligible (well below 0.5π), and the dominate contribution to a potential jump is the demodulation noise. Thus, provided the signal to noise ratio is high and fringe order estimation is accurate, assuming a constant additional phase for the air-gap based EFPI is secure.

Wafer-based EFPI

Similar to the air-gap EFPI, the OPD-dependent additional phase change is also small for the wafer-based EFPI. However, the temperature-dependent material dispersion will introduce another phase term which evolves with OPD. For the spectrometer being used

in the research (Ocean Optics Inc. Model USB2000), the ~200 nm spectral range (centered at 850 nm) is wide enough to manifest a strong influence from dispersion. As a result, the frequency component in the interference spectrum is tuned dispersively, resulting in a chirped sinusoid. The chirp will eventually show up as a phase term that depends on the dispersion condition, which is a function of temperature (recall that OPD is also temperature-dependent). Consequently, the dispersion induced additional phase is OPD-dependent, when used as a temperature sensor. The measured and simulated phases as a function of OPD for a wafer-based EFPI are co-plotted in Figure 2.13 (b). The measurement was based on continuous monitoring of a 57.5μm thick C-plane sapphire wafer as temperature increased from room temperature to 1600^{o}C. The simulation was based on a 69.5μm fused silica wafer (CTE: 0.6 ppm/^{o}C) and temperature-dependent Sellmeier model [67]. Standard periodogram was used for OPD and phase demodulation (see 4.3.1). The choice of silica wafer was due to the absence of relevant data for sapphire, but the agreement between the simulation and experimental results are evident. The ripple in the measurement result was analyzed to be contributed by the fixed-pattern noise from the charge-coupled device (CCD) of the spectrometer. We concluded that for wafer-based EFPIs as temperature sensors, large additional phase change may result as a function of dispersion. Consequently, assuming a constant additional phase in the WLI algorithm embraces high risk of demodulation jumps (See 4.2.2).

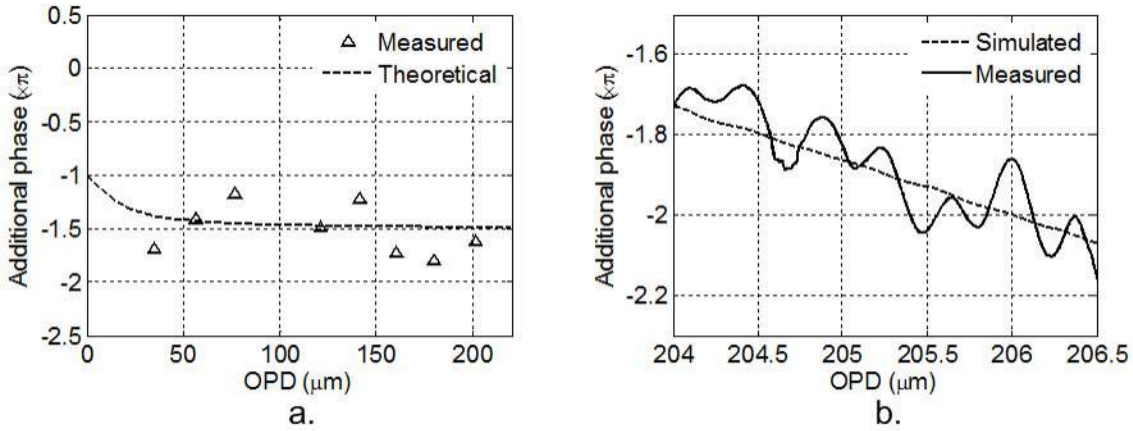

Figure 2.13. Additional phase as a function of OPD for EFPI cavities. (a) Experimental and theoretical additional phases captured as a function of OPD for an air-gap EFPI. (b) Experimental and theoretical additional phases of a wafer-based EFPI show strong OPD-dependence as a result of material dispersion.

2.4 Conclusion

A theoretical effort to model the interference spectra of low finesse fiber optic Fabry-Perot interferometers is presented in the chapter. The deduction of the theory was based on a rigorous diffraction treatment of the field in the FP cavity, and through some reasonable approximations, we reached a transform pair between the interferometer output and the spatial power density distribution projected onto the direction normal to the reflection mirrors. After some further approximations, it was found that the above relationship reduced to a Fourier-transform problem, which was analogous to the Fourier transform pair formed by the output intensity of a Michelson interferometer and the spectrum of the optical source used to illuminate the interferometer. The theory was experimentally proven using both single-mode fiber and multimode fiber based EFPIs, and we sought to establish relationships between the new model with previously published theoretical approaches. We found that the fringe visibility and additional phase in the interferogram were strongly influenced by the output spatial power density distribution and working wavelength, but were not directly related to either temporal or spatial degree of coherence. We further analyzed the visibility curves of a wafer-based EFPI, excited with different fibers. According to the model, different excitation condition results in quite distinctive features of the visibility curve, and maximizing the fringe contrast relies on designing the excitation to yield a minimized beam divergence. At last, we analyzed the OPD-dependent additional phase terms separately for air-gap and wafer-based EFPIs, and found that in principle, the additional phase of an air-gap cavity changes very moderately while that of a wafer-based cavity is dominantly affected by material dispersion.

Chapter 3 Modeling of Fiber Optic Low-Finesse IFPI Sensors

3.1 Introduction

The Single-/multi-/single mode (SMS) fiber optic structure is formed by fusion splicing a section of multimode (MMF) fiber sandwiched into a single-mode fiber (SMF) link [68]. When used in transmission mode, such structures are applied as sensors, filters, modulators, switches, and fiber lenses [69-77], and both step-indexed (SI-) [76, 78] and graded-indexed multimode fibers (GI-MMF) [72, 79] have been studied in the past. In these configurations, modal interference plays a central role in generating desired interference signal.

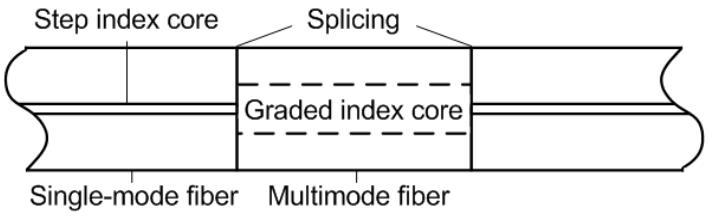

Figure 3.1. Schematic of the SMS-IFPI sensor.

When used in reflection mode, the SMS structure is typically referred to as a (low-finesse) fiber optic intrinsic Fabry-Pérot interferometer (IFPI) [80, 81]. The desired interference is formed by the two reflections generated at the splicing boundaries. The sinusoidal sensor signal is suitable for harmonic-analysis-based signal processing, in which multiple IFPIs with various cavity lengths can be fabricated along a single fiber-optic link. Each sensor contributes to the total spectrogram a harmonic component with distinct frequency defined by its cavity length [27, 80]. The subject of the work is GI-MMF based SMS-IFPI sensor (IFPI infers reflection mode, see Figure 3.1). Through a combination of analysis and experimentation, this work presents a comprehensive picture of the SMS-IFPI sensor structure. A variety of design considerations are addressed to optimize sensor strength, SNR, transmission loss, multiplexing capability, and signal stability.

The first consideration in IFPI is the compromise between SNR and sensor mechanical integrity. This chapter addresses these practical design issues by presenting an analytical

solution for reflectivity at the splicing junction for a given refractive index transition width.

It is well accepted that the SMS-IFPI sensor has the potential for very low transmission loss due to the selective modal excitation in the MMF [70]. However, sensors reported to date have exhibited high transmission loss (roundtrip about -3dB on average), which contradicts the established belief. The loss results in an attenuation of almost 20dB through 6 inline sensors, yielding an insufficient signal-to-noise ratio (SNR) for any additional sensors to be multiplexed. In 2003 Kumar *et al.* attributed this insertion loss problem to the large mismatch between the fundamental modes of SMF and MMF [72]. Practically the roundtrip insertion loss needs to be reduced to below 1 dB in order to multiplex ten sensors.

On the other hand, modal interference in GI-MMF has been employed to fabricate a variety of fiber optic lenses and collimators since 1987 [82-85]. This work expands on the principle of a gradient-index lens, using controlled modal interference to dramatically reduce sensor insertion loss. Section 3.2.2 contains a rigorous analysis of cavity refocusing using both the traditional ray matrix approach and fiber mode theory. Though experimentation (Sections 3.2.3), the resulting optimized IFPI sensor demonstrated greatly reduced roundtrip loss below 0.5 dB. A novel multiplexing scheme, based on the analysis results of multiple MMF types, is presented in 3.2.3. Modal interference is shown to complicate the sensor signal, obscuring the sinusoidal Fabry-Pérot fringe pattern. The issue of modal interference is analyzed to shed light on IFPI sensor signal demodulation, as will be discussed in 3.3.

3.2 Basic models for sensor reflection and transmission

3.2.1 Reflectivity of the cavity mirrors

The upper bound of the reflectivity of a planar splicing surface can be roughly estimated by the Fresnel reflection formula [86]

$$R = \frac{\left(n_1 - n_2\right)^2}{\left(n_1 + n_2\right)^2} \tag{3.1}$$

where n_1 and n_2 are the highest refractive indices of the fiber cores. During a real fusion splice process, the extremely high temperature and finite arc duration give rise to diffusion of the dopant across the splicing plane, which tends to smear any index difference across the boundary, thus reducing reflectivity. In order to model the complex index profile, numerical methods have been used [86]. Here we consider a simple analytical solution to show how the reflectivity decreases with widening index transition length.

Suppose a complex index distribution along the fiber axis n(z), and assume the index is uniform on the fiber cross section for any given z. For the above index profile, at location z the amplitude reflectivity is given by Eq.3.1. Assuming the total change of n is small, r(z) = n'(z) dz/2n(z), where n'(z) = dn/dz is the changing rate of n with respect to z. Let z = 0 represent the point at which the total reflected field is detected, and the field reflected at z = z_0 will pick up a phase term exp[-$j2\beta z_0$] at z = 0. The term β denotes the optical propagation constant in the fiber (here for simplicity the fiber is assumed to be single-mode). The total field reflectivity, defined by the ratio between the reflected field and the input field at z = z_0 can thus be expressed as

$$r_{tot} = \int_{-\infty}^{\infty} m(z) e^{-j(2\beta)z} dz \tag{3.2}$$

where $m(z) = n'(z) / 2n(z)$ and the power reflectivity is found by $R = |r_{\text{tot}}|^2$. Eq. 3.2 shows the Fourier transform (FT) relationship between m(z) and r_{tot}. It should be noted that such mathematical relationship has been used for frequency domain distributed sensing [8]. The reflection spectrum of an IFPI with finite index transition length is modeled by applying Eq.3.2 and some basic properties of FT.

The splice point with diffusion-induced finite transition width is modeled by a half-period cosine function, and the index profile along the z-axis of an imperfect IFPI is shown in Figure 3.2 (a). The FP cavity length is L, the transition width is Δ, and the total index change is δn. The corresponding m(z) distribution is calculated and shown in Figure 3.2 (b). This distributed reflectivity profile can be represented as the convolution of two functions (f_1 * f_2) (z), where f_1 is a rectangular-windowed cosine (Figure 3.2 (c)), and f_2 is

formed by two Dirac delta functions at $\pm L/2$ with amplitude (-/+) unity (Figure 3.2 (d)). The above procedure assumes a constant n in the denominator of m, which is reasonably accurate for small index changes. The final power spectrum, by using Eq.3.2 and some mathematical manipulations, is

$$I = \frac{\pi^2}{2}\left(\frac{\delta n}{4n}\right)^2 \Gamma^2(\beta\Delta)\left[1-\cos(2\beta L)\right] \tag{3.3}$$

where $\Gamma(x)=\text{sinc}(x-\pi/2)+\text{sinc}(x+\pi/2)$ and sinc(x) = sin(x)/x. The result is shown in Figure 3.3, in which the relative reflectivity (reflectivity normalized to the maximum reflectivity defined in Eq.3.1) is plotted as a function of the transition width Δ for three different wavelengths. n is assumed to be 1.46. When the transition length approaches λ/2 (λ being the vacuum wavelength), the reflectivity drops more than 20 dB from its maximum value.

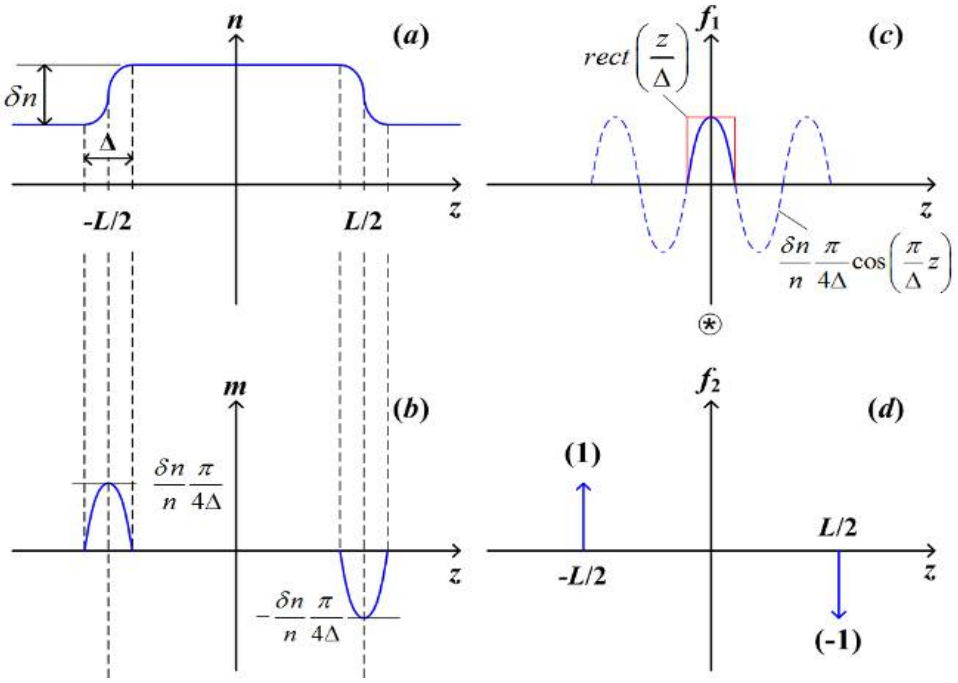

Figure 3.2. Computation procedure to calculate m(z) for the index profile shown in (a). The m profile, shown in (b), can be decomposed as a convolution of the functions shown in (c) and (d).

In practice, the optimal splicing condition is found by compromising splicing strength and the reflectivity. In Table 3.1, two splicing conditions are compared (with fusion splicer Sumitomo Type-36): a standard MMF-MMF splice setting ("hot"), and an optimized splicing condition for IFPI fabrication ("cold"). Splicing was performed using SMF (SMF-28, Corning Inc.) and GI-MMF (GIF625, Thorlabs, Inc.).

Table 3.1. Splicing parameters for SMS-IFPI sensors.

Type	Duration (second)	Prefusion (second)	Gap (μm)	Overlap (μm)	Power [a] (level)	Strength[b] (με)	Reflectivity (dB)
Hot	4.5	0.1	10	15	20	9,800	<-70
Cold	0.5	0.2	5	10	22	6,700	-50

[a]Power level is relative, the maximum level is 40.

[b]Strength was found by the average value of breakage strain.

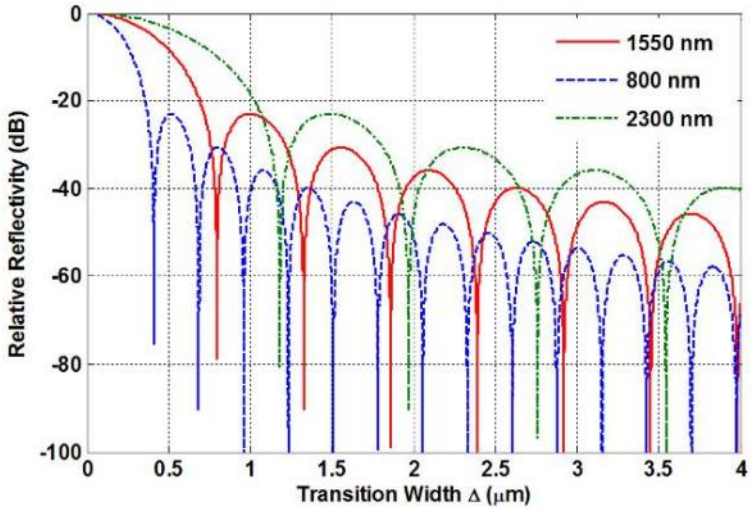

Figure 3.3. Relative reflectivity as a function of index profile transition width. Solid, dashed and dot-dash curves represent 1550, 800 and 2300 nm, respectively.

3.2.2 GI-MMF cavity refocusing

The theoretical analysis begins with the traditional ray matrix method, and is further extended to the more rigorous fiber modal analysis. Both methods are shown to give similar results.

The ray matrix approach adopts the treatment by Emkey and Jack [82]. The modeling process begins with the complex q parameter of a Gaussian beam with curvature radius R_C(z) and beam radius ω(z)

$$\frac{1}{q(z)} = \frac{1}{R_C(z)} - i\frac{\lambda}{\pi\omega^2(z)n} \tag{3.4}$$

The q parameter at the SMF-MMF boundary is defined as q_1, and the input field is the LP_{01} mode of the SMF. The planar wavefront at the z = 0 splice interface requires $R_C(0)\rightarrow\infty$. In order to calculate the q parameter in the MMF at z = l, the transformation is readily obtained by

$$q_2 = (Aq_1 + B)/(Cq_1 + D) \tag{3.5}$$

the elements A, B, C and D are determined by the GI-MMF through

$$\begin{bmatrix} A & B \\ C & D \end{bmatrix} = \begin{bmatrix} \cos(gl) & \frac{1}{g}\sin(gl) \\ -g\sin(gl) & \cos(gl) \end{bmatrix} \tag{3.6}$$

where the g parameter is defined as

$$g = \frac{\sqrt{\delta}}{a_{MMF}} \tag{3.7}$$

where δ = 1-(n_2 / n_1)^2, (notice δ is twice the value of the fractional refractive index difference), in which n_1 and n_2 denote the maximum refractive index of the MMF core, and the refractive index of the MMF cladding, respectively; a_{MMF} denotes the radius of the GI-MMF core. Inserting Eq.3.4 into Eq.3.5 and applying $R_C(0)\rightarrow\infty$ for q_1, we get

$$\frac{1}{q_2(l)} = A - iB \tag{3.8.1}$$

$$A = \frac{g(\lambda^2 - \pi\omega_0^4 n_1^2 g^2)\sin(gl)\cos(gl)}{\lambda^2\sin^2(gl) + \pi^2\omega_0^4 n_1^2 g^2\cos^2(gl)} \tag{3.8.2}$$

$$B = \frac{\lambda \pi \omega_0^2 n_1 g^2}{\lambda^2 \sin^2(gl) + \pi^2 \omega_0^4 n_1^2 g^2 \cos^2(gl)} \tag{3.8.3}$$

where ω_0 is the Gaussian beam radius of the SMF LP_{01} mode. In seeking of the position where planar wavefront along the MMF is located, we set $A = 0$ and find two sets of solutions for l

$$l_r = \frac{\pi}{g} N \text{ , where } N = 1,2,3, \ldots \tag{3.9.1}$$

$$l_c = \frac{\pi}{g}\left(\frac{1}{2} + N\right), \text{ where } N = 1,2,3,\ldots \tag{3.9.2}$$

For the first set of solutions (l_r), substitution into Eq.3.8.3 yields a spot radius equal to ω_0, which is identical to that of the SMF fundamental mode. We refer such locations as "refocusing points". The second set of solutions (l_c), when inserted into Eq.3.8.3 gives rise to a spot radius of

$$\omega(l) = \frac{\lambda}{\pi \omega_0 n_1 g} \tag{3.10}$$

It can be easily shown that $\omega(l) \approx (NA_{SMF}/NA_{MMF})a_{MMF}$, where NA_{SMF} and NA_{MMF} are the numerical apertures of SMF and MMF. For typical GI-MMF, the value of Eq.3.10 is approximately 2~3 times of ω_0. We refer l_C as "collimating points", which are employed to fabricate fiber lenses.

Equations 3.9.1 and 3.9.2 imply a series of periodic focusing and defocusing when light propagates in a SMF-excited GI-MMF. For an SMS-IFPI, when the cavity length is cut to the neighborhood of l_r (Eq. 3.9.1), light in the FP cavity is refocused into the lead-out SMF, leading to minimum transmission loss. On the contrary, when the FP cavity has a length near to l_c (Eq. 3.9.2), due to the significant mode field diameter (MFD) mismatch, coupling of the cavity mode into the lead-out fiber can be very lossy.

In reality, periodic refocusing effect only exists at the beginning of the MMF section (within several centimeters), and the pattern becomes increasingly blurry along the fiber.

The periodicity is dictated by the "beating" of the excited modes (as will be discussed below), and eventually all the modes become desynchronized during propagation. In order to better understand and more accurately analyze such phenomena, fiber modal analysis is necessary.

For the GI-MMF whose index profile is radially parabolic, the transverse mode profile can be well approximated by the Laguerre-Gaussian function [87]. If the MMF is excited by standard SMF, modes with azimuthal index other than zero ($LP_{\nu\mu}$ mode, $\nu \neq 0$) annihilate due to mode orthogonality, which greatly simplifies the following analysis. In this case the mode profile can be expressed as

$$\psi_\mu(r) = Ae^{-\left(r^2/\omega_1^2\right)} L_\mu\left(\frac{2\rho^2}{\omega_1^2}\right) \tag{3.11}$$

with an effective Gaussian spot size defined through

$$\omega_1^2 = \frac{2a_{MMF}}{k_0 n_1 \sqrt{\delta}} \tag{3.12}$$

and the mode number μ = 0,1,2,…. In Eq.3.11 ρ denotes radial coordinate and L_μ is the Laguerre polynomial of degree μ. The constant A is calculated by mode power normalization:

$$\int_0^\infty \left|\psi_\mu(\rho)\right|^2 \rho d\rho = 1 \tag{3.13}$$

The effective refractive index for mode μ is found to be

$$n_{e,\mu} = n_1\left[1 - \frac{2\sqrt{\delta}}{k_0 n_1 a_{MMF}} M\right]^{1/2} \tag{3.14}$$

where $M = 2\mu+1$ and the propagation constant is defined by $\beta_\mu = k_0 \cdot n_{e,\mu}$. The mode functions in Eq.3.11 are orthogonal, and the LP_{01} mode of the SMF may couple into multiple core modes of the MMF at the first splicing plane. The field in the MMF is thus decomposed into the orthogonal modes as

$$\psi_{MMF}(\rho) = \sum_{\mu=0}^{N-1} c_\mu \psi_\mu(\rho) \tag{3.15}$$

ψ_{MMF} is the field profile in the MMF, N is the total number of modes excited, and the coupling coefficients c_μ are found by the overlapping integral:

$$c_\mu = \int_0^\infty \psi_{SMF}(\rho)\psi_\mu^*(\rho)\rho d\rho \tag{3.16}$$

where ψ_{SMF} is the normalized field profile of the SMF LP_{01} mode. The field profile at any location along the MMF (assume z = 0 is the first splicing plane) is found by summing the individual orthogonal modes:

$$\Psi(z) = \sum_{\mu=0}^{N-1} c_\mu \psi_\mu(\rho)\exp(-j\beta_\mu z) \tag{3.17}$$

Table 3.2. Fiber parameters used for the simulation.

Fiber Type	Core Diameter (μm)	Cladding Diameter (μm)	Core Index (RIU)	Cladding Index (RIU)	δ (%)
SMF	8.4	125	1.4504	1.4447	0.78
MMF1	50	125	1.4760	1.4615	1.96
MMF2	62.5	125	1.4760	1.4500	3.49

Table 3.3. Power coupling coefficients of five MMF modes

Fiber	1 LP_{00}	2 LP_{01}	3 LP_{02}	4 LP_{03}	5 LP_{04}
MMF1	0.8259	0.1115	0.0413	0.0132	0.0051
MMF2	0.8457	0.1002	0.0371	0.0108	0.0040

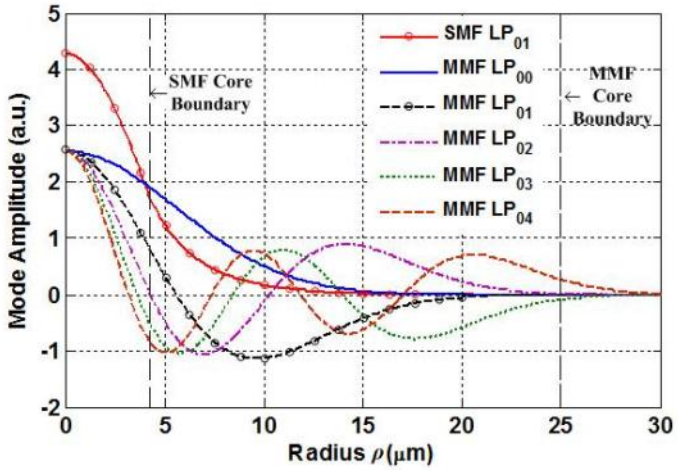

Figure 3.4. Five lowest order mode profiles of MMF1. The fundamental mode profile of the excitation SMF is also plotted for comparison. All the modes are normalized, and SMF and MMF core boundaries are marked.

Numerical solutions of the field distribution in the MMF were generated using the fiber parameters listed in Table 3.2, with $\lambda = 1.55\mu m$. The excitation fiber was a SMF (as listed in the table on the row "SMF"), and two types of MMF's were studied, the parameters of which were provided in the table as row "MMF1" and "MMF2". The normalized mode profiles of the five lowest MMF modes (LP_{00} to LP_{04}) were calculated and are depicted in Figure 3.4 for MMF1. Co-plotted is the normalized profile of the excitation SMF LP_{01} mode. The figure clearly shows the MFD mismatch between the SMF and MMF fundamental modes. Under this particular excitation condition, the power excitation coefficients ($|c_\mu|^2$) for five lowest order modes of MMF1 and MMF2 were calculated based on Eq.3.16 and are summarized in Table 3.3. For both fibers, the fundamental mode carries more than 80% of the total power, and less than 20% of the power is carried by higher order modes with significantly different propagation constants. The splitting of power into different modes, which propagate individually with distinct phase delays, causes interference among the modes during propagation to create particular field patterns along the fiber, as expressed by Eq.3.17. In Figure 3.5 (a), the amplitude of the field along MMF2, with z = 0 as the splicing boundary, is plotted. In Figure 3.5 (b), the field distribution for a SI-MMF, with fiber parameters identical to MMF2 is illustrated for comparison. The field distribution in the GI-MMF manifests periodic focusing along

the z axis, whereas the field in the SI-MMF is rather complex. The reason causing this disparity lies in a special relationship among the MMF propagation constants, as discussed below.

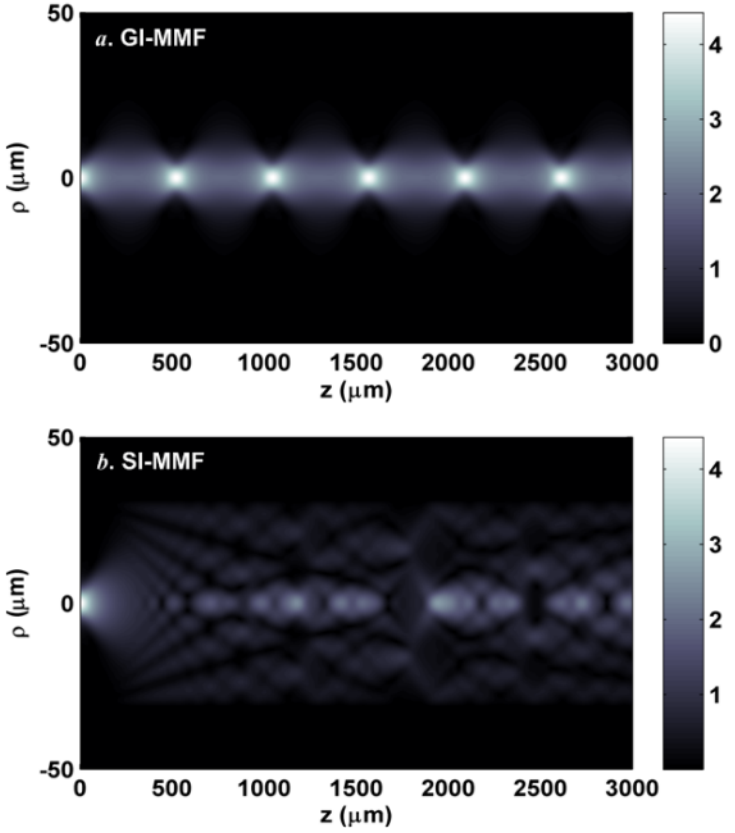

Figure 3.5. Light propagation in multimode fibers. (a) Field amplitude distribution in GI-MMF (MMF2). (b) Field amplitude distribution in SI-MMF, whose parameters are identical to MMF2.

The periodic focusing effect in GI-MMF gives rise to periodic transmission loss. An investigation of the loss using fiber mode theory gives a clearer physical interpretation of the refocusing phenomenon. The coupling loss of the MMF can be expressed as [78]

$$\alpha(z) = \left| \sum_{m=1}^{N} c_m^{\,2} \exp\left(j\beta_m z\right) \right|^2 \tag{3.18}$$

where $m = \mu + 1$. Through binomial expansion of Eq.3.14, the difference between two neighboring values of the effective refractive index is calculated as:

$$\Delta_n = n_{e,n} - n_{e,n+1} = 2\sqrt{\delta} \Big/ \left(k_0 a_{MMF} \right) \tag{3.19}$$

Inserting Eq.3.19 into Eq.3.18 leads to

$$\alpha(z) = \left| \sum_{m=1}^{N} c_m{}^2 \exp\left[-j(m-1) k_0 \Delta_n z \right] \right|^2 \tag{3.20}$$

With some mathematical manipulations, the loss is obtained as

$$\alpha(z) = \sum_{p=1-N}^{N-1} \xi_p \exp\left(jpk_0 \Delta_n z \right) \tag{3.21}$$

in which the expansion coefficient is expressed as

$$\xi_p = \sum_{n-m=p} \left(c_n c_m \right)^2 \tag{3.22}$$

As clearly shown in 3.21, the z dependent transmission loss is a Fourier series with fundamental angular frequency k0Δn, which predicts the spatial period as

$$\Lambda = \frac{2\pi}{k_0 \Delta_n} = \frac{\pi a_{MMF}}{\sqrt{\delta}} = \frac{\pi}{g} \tag{3.23}$$

The periodicity shown in Eq.3.23 is in complete agreement with the one deduced by the ray matrix method as in Eq.3.9.1. In fact the effective index relationship in Eq.3.19 dictates a spatial frame with which the field repeats itself according to the Fourier series Eq.3.21; this serves as an alternative interpretation of the refocusing effect. In applying Eq.3.19, only the first two terms in the expansion of Eq.3.14 are retained. However, neglecting the higher order terms in Eq.3.14 will eventually cause significant error at larger *z*, and the Fourier series in Eq.3.21 will fail. Thus the refocusing can only held for a certain distance before reaching an unfocused equilibrium state, which, together with the decay of the leaky modes, sets up a steady-state propagation within centimeters [88].

3.2.3 Verification of the refocusing model

Insertion loss reduction by cavity refocusing

To verify the theory in Section 2B, standard SMF (SMF 28e, Corning Inc.) was fusion spliced to a section of MMF (InfiniCor600, Corning, Inc.) and re-spliced back to the lead-out SMF. According to the technical specs, the MMF is similar to MMF1 in Table 3.2. The transmission loss of the device was characterized as a function of the MMF length. For the fusion splicing, we used both of the splicing conditions in Table 3.1.

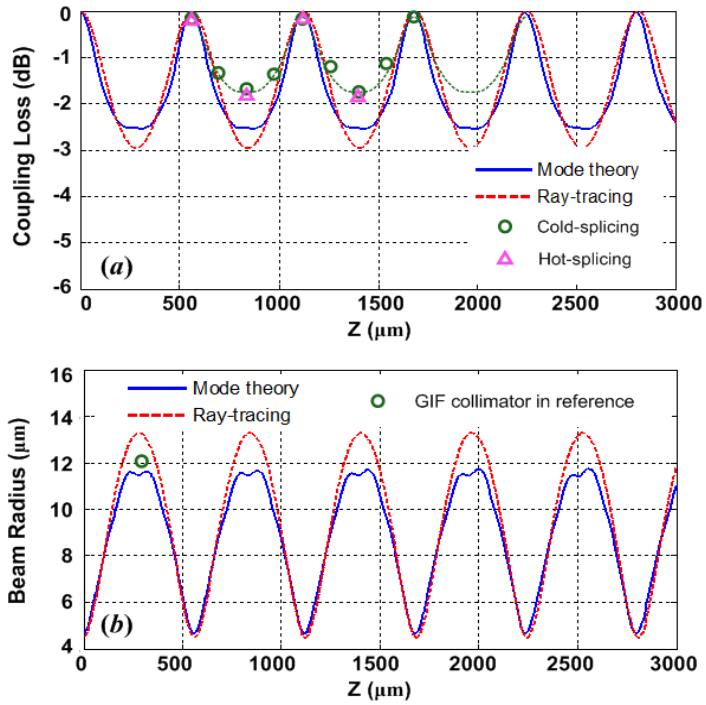

Figure 3.6. Calculated and experimental results for the coupling loss and beam radius of the GI-MMF. (a) Coupling loss variation as MMF length and (b) Beam radius variation as MMF length. For the simulation, the MMF1 fiber is selected. Corning InfiniCor600 was used for the experiment.

For comparison, we used both the ray matrix method and the fiber modal analysis to determine the transmission loss and the beam radius of MMF1. The calculated and measured transmission loss (one-way) are co-plotted in Figure 3.6 (a). Notice the splicing condition does not strongly affect the transmission loss, in contrast to its influence on the reflection. In Figure 3.6 (b), the calculated beam radius, using both ray matrix and modal analysis, are shown to have good agreement. We also compared the calculation result to

the experimental result published in [84], in which the fiber is cut to designed length for beam collimation. The beam spot size shown in the figure in green circle was deduced from the divergence angle as reported in the paper.

The influence of the loss reduction on sensor signal demodulation was further studied with real sensors. A link with ten IFPI sensors was fabricated using standard SMF and a GI-MMF (GIF625, Thorlabs Inc.). The MMF selected has fiber parameters similar to that of MMF2 as listed in Table 3.2. Based on simulation results, the refocusing length was determined to be 517μm, according to Eq. 3.9.1. Subsequently, the cavity lengths of the sensors were cut to multiples of 517μm to minimize the transmission loss. The spectrum of the link was interrogated using a swept-laser spectrometer (Si-720, Micron Optics Inc.) which offered 20,000 interrogation points from 1520 to 1570nm spectral range. All the sensors were co-located inside a furnace and temperature calibration was performed. The calibration curve was fitted with a third-order polynomial, and the fitting error was characterized by its standard deviation as an estimation of the 1-σ estimation error. Notice that the calibration was based on calculating the OPD of the sensors, and we used the "direct OPD" approach, as elaborated in [60], Eq. 21, for the signal demodulation.

For comparison, another link with six sensors was fabricated and tested. Instead of having controlled length to minimize the transmission loss, the sensors were cut into lengths in rough multiples of 1000 μm (from 1000 to 6000um). The link had significantly increased transmission loss (roundtrip loss averaged nearly 3dB per sensor), in vivid contrast to the first link whose average loss was <0.5 dB per sensor. This is clearly shown in the Fourier transform of the sensor spectra in Figure 3.7 (a), where the harmonic peaks due to each individual sensor are visible.

In Figure 3.7 (b), the relative OPD estimation error (normalized to OPD) for the sensors in both links is plotted. While the sensors in link 1 demonstrate no quality reduction toward the end of the link, the last three sensors in the non-optimized link show dramatically increased inaccuracy as a result of reduced SNR. A natural benefit from the loss reduction is an increase in multiplexing capacity.

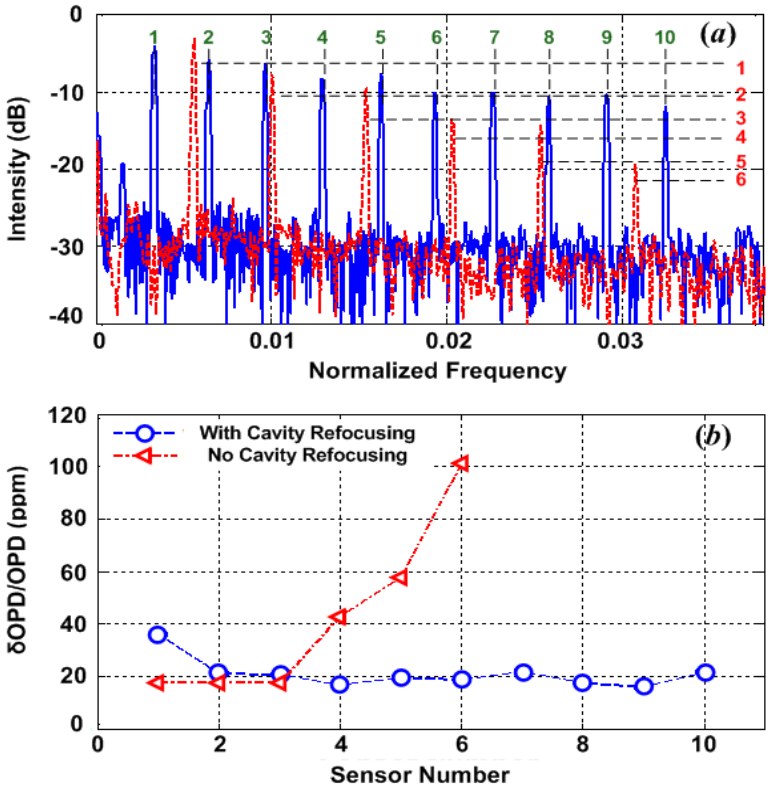

Figure 3.7. Experimental results showing the benefit of IFPI cavity length control. In (a), the FFT of the spectra for a link with (solid) and without (dashed) refocusing are compared. The relative OPD estimation error for each sensor in the links is plotted in (b).

Increasing the multiplexing capacity

As discussed in 3.2.2, by controlling the SMS-IFPI cavity lengths, the roundtrip insertion loss of each sensor can be reduced to less than 0.5dB. For a twenty-sensor link, this results in a total insertion loss of less than 10dB, which is sufficient for reliable demodulation of all the sensors. However, this requires some of the sensors to have very long cavity lengths: the twentieth sensor will have a cavity length exceeding 1 cm. Such long cavity length tends to impose signal demodulation challenges stemming from environmental fluctuations. To address this problem, different types of MMF can be employed. Table 3.4 lists some key properties of three types of GI-MMF. The diverse optical properties of different MMFs lead to distinct pitches, allowing multiplexing of more than twenty sensors with a maximum cavity length of around 6 mm. The designed

cavity lengths should bear enough separation to allow minimum crosstalk and enough dynamic range. Figure 3.8 conceptually illustrates a potential design.

Table 3.4. Key properties of three types of MMF.

Fiber	NA	Δ (%)	Pitch (μm) Theoretical	Pitch (μm) Measured
GIF625	0.275	1.8	517	520
InfiniCor600	0.200	1.0	555	563
OFS100/140	0.298	2.1	764	840

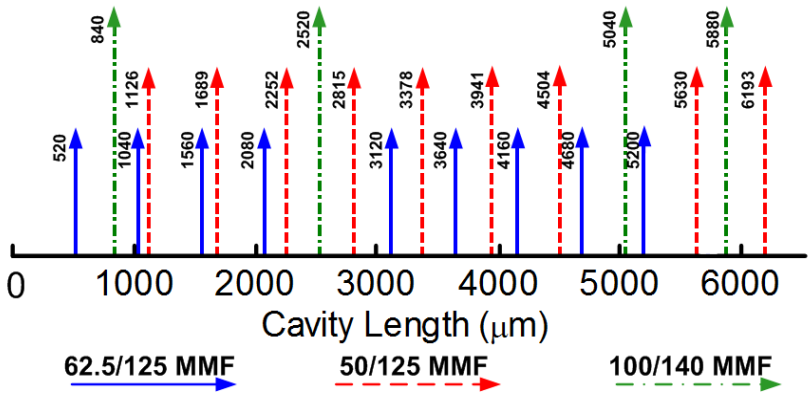

Figure 3.8. Design of a sensing link with 22 IFPI sensors multiplexed with three different types of MMF. 62.5/125 MMF: Thorlab GIF-625; 50/125 MMF: Corning InfiniCor600; 100/140 MMF: OFS-100/140.

3.3 Analysis of the IFPI additional phase

Whitelight interferometry has been proven to be perhaps the most practical way for the demodulation of fiber F-P sensors. Typical signal demodulation aims at finding the optical path difference (OPD, defined as $OPD = 2nL$, where n is the refractive index and L is the physical length of the cavity) according to the sinusoidal spectral information given by [27, 39, 89] :

$$I \sim \cos\left(k \cdot OPD + \pi + \varphi\right) \tag{3.24}$$

In the above formula the DC component has been removed already. The sinusoidal nature of the spectrum comes from the interference generated by the two cavity mirrors, k is equal to $2\pi/\lambda$ where λ is the light wavelength in vacuum, the term π comes from the

reflection from an optically denser medium, and the term φ is an additional phase term, which has been investigated in the case of SMF-EFPI and MMF-EFPI by Han *et al.* [40, 52] and further in chapter 2 (2.3.6). This additional phase term is explained as a result of wave-front distortion of the light during propagation in free-space. The OPD demodulation accuracy can be greatly enhanced by measuring the additional phase term φ in advance (the so-called OPD demodulation with known phase), which requires the phase term to be a constant for any given FP cavity [27]. In reality, the phase term is dependent on the cavity length in EFPI [40] and is also dependent on the mode-field distribution (MFD) in the lead-in multimode fiber for MMF-EFPI [52] (the dependence is further analytically expressed by a transform of $I(k_z)$ as in chapter 2), which means one needs to be very careful before assuming the phase term to be constant during OPD measurement. In this subsection, by taking into account the overall effect exerted by the multiple transmission modes in the cavity, we analyzed the interference spectrogram of SMS-IFPI sensor and concluded that a non-constant phase term also existed. Similar to the EFPI case, the phase term was generated by the field wave-front distortion, yet for EFPIs the distortion comes from free space propagation while for IFPIs it is a side effect of inter-modal dispersion.

3.3.1 Modal analysis of the SMS-IFPI

Exact field expression

A typical SMS-IFPI sensor is illustrated in Figure 3.1. Instead of applying Eq.3.24 to obtain the sensor spectrum, a more accurate model employs analysis of modal coupling and propagation in the multimode waveguide [51, 72, 90, 91]. Light in the SMF is carried by LP_{01} mode of SMF with normalized mode profile Φ_0. At the interface R_1, the mode energy is split into several parts carried separately by LP_{0k} modes with normalized mode profile Φ_k in the MMF (here we made the assumption that the MMF is weakly guided, step-index fiber for simplicity of analysis). Modes in the MMF with azimuthal number other than zero will not be exited due to mode orthogonality. For each mode, the coupling coefficient is defined as $\eta_{0\to k} = \iint_{R_1} \phi_0 \phi_k^* dxdy$. Being reflected by R_2 and propagating to R_1, the k'th mode profile can be expressed as $r\eta_{0\to k}\phi_k \exp\left[j\left(2\pi OPD_k / \lambda + \pi\right)\right]$, where

$OPD_k = 2n_k L$, n_k is the effective index of the *k'*th mode. At interface R_1, all these modes will be re-coupled into the fundamental LP_{01} mode of the single mode fiber with coupling coefficient $\eta_{k\to 0} = \iint_{R_1} \phi_k \phi_0^* dxdy = \eta_{0\to k}^*$. As a result, the contribution to the total mode profile by each mode can be described as $r\left|\eta_{0\to k}\right|^2 \phi_0 \exp\left[j\left(\frac{2\pi}{\lambda} OPD_k + \pi \right)\right]$, and the total field profile at R_1 can be expressed as:

$$\phi_s = r\phi_0 \left(1 + \sum_{k=1}^{N} \eta_k^2 \exp\left[j\left(\frac{2\pi}{\lambda} OPD_k + \pi \right)\right]\right) \tag{3.25}$$

where $\eta_k = \left|\eta_{0\to k}\right|$ is a real number and *N* modes are assumed to be excited in the MMF. Based on the expression for the total field above, we can find the reflection intensity from the sensor as:

$$I = \iint_{R_1} \phi_s \phi_s^* dxdy = r^2 \left|1 + \Sigma\right|^2 \tag{3.26}$$

where $\Sigma = \sum_{k=1}^{N} \eta_k^2 \exp\left[j\left(\frac{2\pi}{\lambda} OPD_k + \pi \right)\right]$ is an effective vector to be discussed in more details in the following section. Also we have already applied the normalization condition $\iint_{R_1} \phi_0 \phi_0^* dxdy = 1$. Note that if only one mode is excited in the MMF, Eq.3.26 will be automatically reduced to Eq.24 after canceling the DC component.

Two-mode excitation

The expression for the total field intensity deduced from the last section (Eq.3.26) is comprehensive but relatively complicated. In this section we consider a much simpler case in which only two modes are excited in the MMF with similar effective refractive indices; this analysis can provide us with illustrative understanding of how intermodal dispersion affects the sensor spectrum.

Assume that the effective indices of the two modes to be n_1 and n_2, respectively, and accordingly the *OPD* experienced by the two modes to be $OPD_1=2n_1L$ and $OPD_2=2n_2L$, define $\Delta OPD = OPD_1 - OPD_2$ such that OPD_2 can be expressed by $\mathrm{OPD}_2 = \mathrm{OPD}_1 - \Delta\mathrm{OPD}$.

The total reflected spectrum can be expressed as

$$I =$$

$$1+\eta_1^4+\eta_2^4+2\eta_1^2\cos\left(OPD_1\cdot k_0\right)+2\eta_2^2\cos\left(\left(OPD_1-\Delta OPD\right)k_0\right)+2\eta_1^2\eta_2^2\cos\left(\Delta OPD\cdot k_0\right) \quad (3.27)$$

In the above equation, the fourth and fifth terms on the right hand side describe the interference of the modes with themselves, and the last term accounts for the interference between the two modes. After some mathematical manipulations, Eq.3.27 can be rewritten as:

$$I = r^2\left\{1+\Gamma+2\sqrt{\Gamma}\sin\left[OPD_1k_0+\varphi\left(\Delta OPD,k_0\right)+\pi\right]\right\}$$

Where

$$\Gamma=\eta_1^4+\eta_2^4+2\eta_1^2\eta_2^2\cos\left(\Delta OPD\cdot k_0\right)$$

$$\varphi\left(\Delta OPD,k_0\right)=\begin{cases}\arctan\left(\dfrac{\eta_1^2+\eta_2^2\cos\left(\Delta OPD\cdot k_0\right)}{\eta_2^2\sin\left(\Delta OPD\cdot k_0\right)}\right), & \sin\left(\Delta OPD\cdot k_0\right)\ge 0\\ \pi-\arctan\left(\dfrac{\eta_1^2+\eta_2^2\cos\left(\Delta OPD\cdot k_0\right)}{\left|\eta_2^2\sin\left(\Delta OPD\cdot k_0\right)\right|}\right), & \sin\left(\Delta OPD\cdot k_0\right)<0\end{cases} \quad (3.28)$$

It is not difficult to find that at the limit $\eta_2^2 << \eta_1^2$ (which means the second mode is excited so weakly that almost all the power is carried by the first mode), Eq.3.28 reduces to Eq.3.24 with the additional phase term equal to zero. As the second mode emerges, the amplitude and phase of the sinusoid will be modulated. The phase term $\varphi\left(\Delta OPD,k_0\right)$ as a function of $\Delta OPD\cdot k_0$ has been plotted in Figure 3.9. To plot the figure, the wavelength span was set from 1400 to 1700 nm, the effective refractive indices of mode 1 and mode

2 were set to be 1.448 and 1.441, respectively, the cavity length was set to 1mm, and four different cases with excitation ratio (η_1^2 / η_2^2) of 6:4, 7:3, 8:2 and 9:1 were compared.

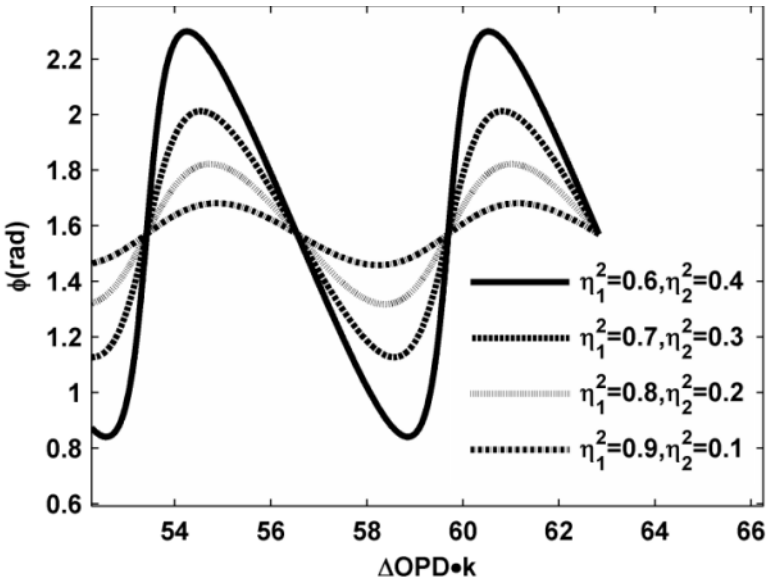

Figure 3.9. Additional phase term for a two-mode cavity at different excitation ratios.

Rotating vector picture

In the previous section we only considered the excitation of two modes inside the MMF cavity. In reality, the number of modes excited can be much more, which complicates the problem. From Eq.3.26, the received intensity is proportional to $\left|1+\Sigma\right|^2$ where the vector Σ is defined as $\Sigma = \sum_{k=1}^{N} \eta_k^2 \exp\left[j\left(\frac{2\pi}{\lambda} OPD_k + \pi \right) \right]$. The received power can be expressed as:

$$I \sim \left|1+\Sigma\right|^2 = 1 + \left|\Sigma\right|^2 + 2\left|\Sigma\right|\cos\left(\psi\right), \text{ where } \psi = \angle\Sigma \tag{3.29}$$

Equation 3.29 leads to the conclusion that the total phase in the interference spectrogram can be directly obtained from the angle of the vector Σ. In the following discussion, for simplicity without losing generality, we omit the phase term π in the expression of vector Σ:

$$\Sigma = \sum_{k=1}^{N} \eta_k^2 \exp\left[j\left(\frac{2\pi}{\lambda} OPD_k \right) \right] \tag{3.30}$$

where $OPD_k = 2n_k L$, n_k is the effective refractive index of the kth mode. It is straightforward to find out that Σ is the sum of N vectors representing N orthogonal modes (define mode vector $\upsilon_k = \eta_k^2 \exp\left[j\left(\frac{2\pi}{\lambda} OPD_k \right) \right]$), the modulus of each vector is the square of the magnitude of the mode coupling coefficient between the given mode and the LP_{01} mode of the SMF; the phase of each vector is simply the product of the vacuum wavenumber and the effective *OPD* of that mode. Figure 3.10 illustrates how the total field vector is related to each individual mode vector. Totally five modes were assumed to be excited.

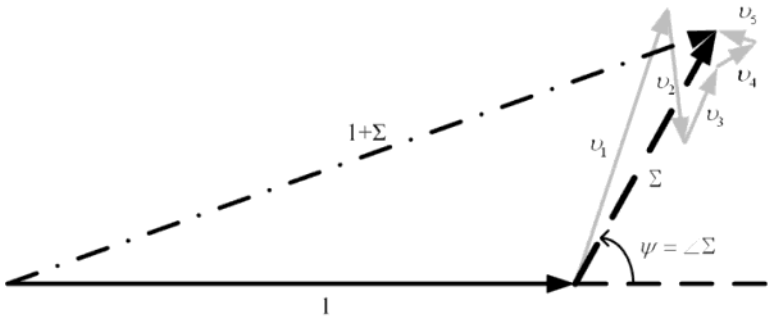

Figure 3.10. Relationship between the total field vector and five individual mode vectors.

In the interference spectrogram, as the wavenumber k increases, all the N individual mode vectors (υ_k) will rotate at different angular speed $OPD_k=2n_kL$, the mode vector of the fundamental LP_{01} mode rotates at the fastest speed (corresponding to the largest effective refractive index), while the mode vector of LP_{0N} mode rotates the slowest; the differences among rotational speeds of all the mode vectors are very small because n_k's have very similar values. Although the individual vectors rotate at similar speeds, their pointing directions are almost arbitrary because the wavenumber k and the cavity length L are both very large numbers. The effective vector Σ rotates at a speed that depends simultaneously on the rotational speed of each vector and their relative orientations. If most of the mode vectors align at similar directions, the rotating speed of the effective vector can be slower than any of the individual vectors; there are also occasions where its

rotational speed is faster than any of the individual vectors (see Figure 3.11for an example).

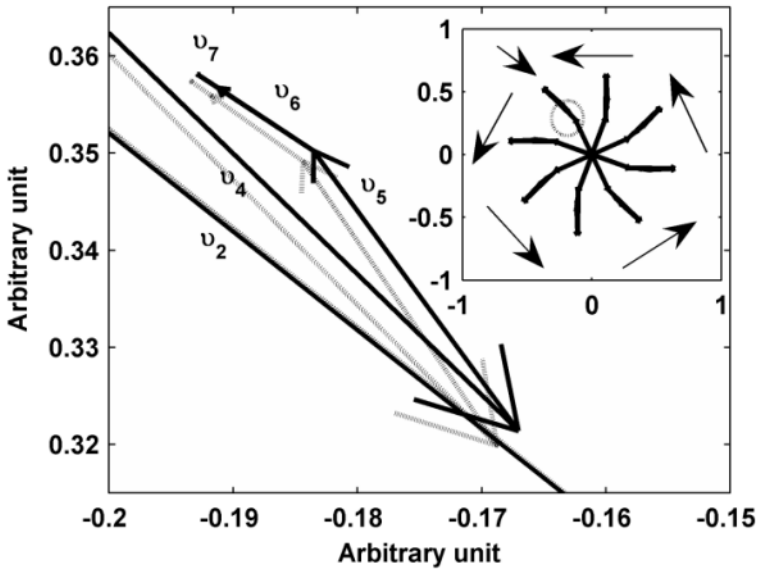

Figure 3.11. Zoom-in view of the rotating vectors. Nine groups of vectors are plotted with equal angular spacing such that υ_1 rotates exactly 2π. Dark lines: first group of vectors (beginning position); gray lines: last group of vectors (end position: υ_1 coincides with υ_1 in the first group, υ_2 is a little behind υ_2 in the first group; the effective vector Σ is ahead of Σ in the first group). Inset: global view of the vector rotation. Upper-left arrow: position of the first and last groups of vectors; other arrows illustrate the rotational direction of the vectors.

Figure 3.11 plots the mode vectors of all the seven excited modes in a step-index MMF with n_{core}=1.448, n_{clad}=1.434, *and* r_{core}=25um, excited by SMF with n_{core}=1.445, n_{clad}=1.440, and r_{core}=4.2um. In the simulation, the cavity length is 2 mm, and the wavelength is set to be λ=1550 nm. Increasing wavenumber k results in rotation of mode vectors, while the effective vector rotates correspondingly. Totally nine groups of vectors are plotted with equal angular spacing, such that the fundamental mode vector (υ_1) of the ninth group coincides with that of the first group, which means by increasing k, υ_1 rotates exactly 2π. Since the fundamental mode travels the fastest, all the higher order modes rotate at slower rates; none of the higher order modes rotates as far as 2π. However, the effective vector rotates faster than the fundamental mode vector, as shown in Figure 3.11.

The end of the cascaded gray arrows (which represents the effective vector after υ_1 rotates by 2π) falls ahead of the end of the cascaded dark arrows (which represents the effective vector before rotation), indicating a faster rotational speed of the effective vector than the fundamental mode vector υ_1.

As k increases, all the vectors begin to rotate; while each individual mode vector rotates at constant speed, the effective vector does not, even though the speed variation is not significant if k scans in a narrow range (within the spectral range of the interference spectrogram). Taking the rotational speed of υ_1 as reference, the relative speed for any other vector can be obtained by subtracting the speed of υ_1 from its own speed. At any given wavenumber k, this relative speed is proportional to the phase difference between that vector and the LP_{01} vector. For the cavity we examined to plot Figure 3.11, when the wavelength is scanned from 1520-1570 nm, the relative phase shift (taking LP_{01} vector as the reference) of the following vectors are plotted in Figure 3.12: LP_{02} (at a lower rotating speed), the effective vector Σ (at a faster, varying speed), and the linear fitting of the rotating speed of Σ (represents a virtual mode vector that best approximates the rotating speed of the effective vector). The angular rotating speed of the virtual vector is actually the first-step estimated $OPD^{(1)}$ of the cavity, as will be discussed in the following section.

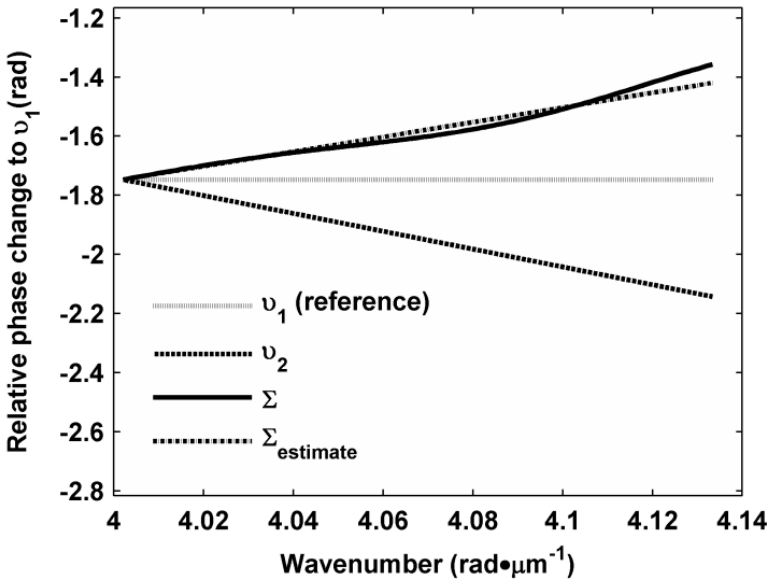

Figure 3.12. Relative phase shift to LP_{01} mode as k increases. Plotted are phase shifts of LP_{02} mode, the effective vector Σ, and a virtual mode with $n_{eff}=n_{estimate}$.

3.3.2 Further discussion of the additional phase

In an actual sensor application, a change in the measurand such as strain or temperature varies the *OPD* of the SMS-IFPI sensor; by detecting with high accuracy the *OPD* change, the change in the measurand can be decoded correspondingly. For example, strain changes the *OPD* of the cavity as

$$\frac{\Delta OPD}{OPD} = \left(1 - p_e\right)\varepsilon \tag{3.31}$$

where p_e is the effective strain-optic constant and ε is the applied strain [92]. Temperature modifies both the dimension and the refractive indices of the cavity according to:

$$\frac{\Delta OPD}{OPD} = \left(\alpha_T + \sigma_T\right)\Delta T \tag{3.32}$$

where α_T is the coefficient of thermal expansion (CTE) of silica, and σ_T is the thermal-optic coefficient of the fiber core [92]. Hence the key of measurement accuracy and resolution lies in the *OPD* decoding quality.

Most of the *OPD* decoding algorithms assume the sensor spectrogram to be purely sinusoidal [27, 39] . According to Eq.3.24, the total phase in the interference spectrum is:

$$\varphi_{tot} = k \cdot OPD + \varphi_0 \tag{3.33}$$

where φ_0 is the additional phase term introduced in section one (the phase term π is omitted). Eq.3.33 indicates that the *OPD* of the cavity equals the angular rotational speed of the total phase φ_{tot} with k. The wavenumber k_m corresponding to the peak locations of the interference pattern should satisfy the phase relationship: $k_m \cdot OPD + \varphi_0 = 2\pi m$, where m is the fringe order of the corresponding peak; let's denote the smallest fringe order on the spectrogram to be m_0, we have: $k_m \cdot OPD + \varphi_0 = 2\pi\left(m_0 + N\right)$ where *N=0, 1, 2, ...* The above relationship can be rewritten as:

$$k_m \cdot OPD + \varphi_0' = 2\pi N\ ,\ \varphi_0' = \varphi_0 - 2\pi m_0\ ,\ N=0,\ 1,\ 2,\ \ldots \tag{3.34}$$

By linearly fitting k_m with N, one can find the first-step estimation of the optical path difference $OPD^{(1)}$. Multiple measurements can be performed to accurately find the phase term φ_0' in advance so that for any measurement follows, we can predict the location of the mth fringe peak by:

$$k_m^{(1)} OPD^{(1)} + \varphi_0' = 2\pi N \tag{3.35}$$

The OPD estimation error (δOPD) is related to a phase shift $\delta\varphi$ by:

$$\delta OPD = \frac{\delta\varphi}{2\pi}\lambda_m \tag{3.36}$$

By setting λ_m=1550 nm, one can calculate that a phase shift of $\pm\pi$ can be induced by an OPD estimation error of ± 775 nm, which is very large. According to computer simulation results, the first step OPD estimation errors fall within ± 200 nm, which correspond to a phase shift of ± 0.26π. If we predict the peak locations by inserting the first-step estimation result $OPD^{(1)}$ into Eq.3.35, the phase difference between the real spectrum and predicted spectrum will have a phase difference within the range [-0.26π, +0.26π]. Figure 3.13 illustrates this situation.

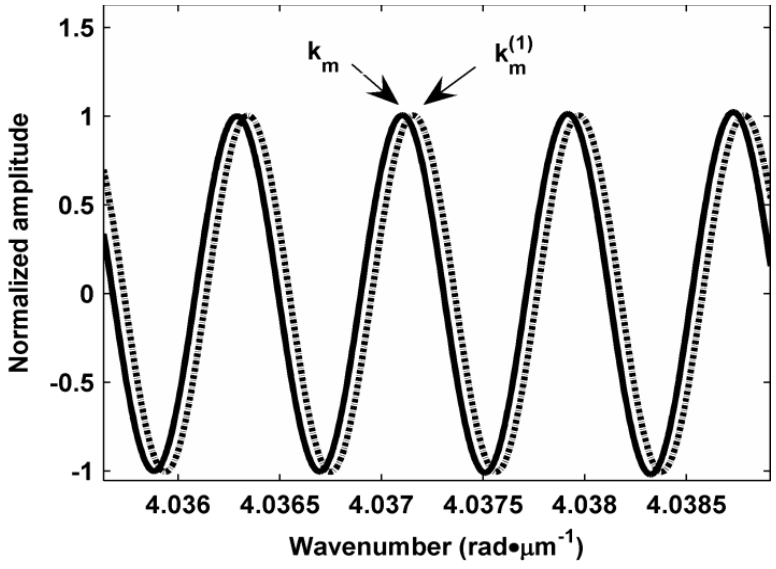

Figure 3.13. Spectral phase shift induced by OPD estimation error

As shown in Figure 3.13, the predicted peaks appear at the vicinity of the real peaks within the phase range [-0.26π, +0.26π]. Mathematically this can be written as:

$$k_m^{(1)} OPD^{(1)} = k_m \cdot OPD \tag{3.37}$$

And we can obtain a better estimation of the value for *OPD* by:

$$OPD^{(2)} = \frac{k_m^{(1)}}{k_m} OPD^{(1)} \tag{3.38}$$

This second step estimation of the *OPD* has much better accuracy, according to computer simulation. The *OPD* estimation error is within ± 1 nm.

The *OPD* demodulation algorithm described above assumes that the additional phase term in Eq.3.33 is a constant. However, as mentioned in 3.3.1, this term is not a constant and can vary with the *OPD*, which adds to the complexity of the signal decoding. We use Eq.3.26 to calculate the interference spectrogram for our computer simulation. To calculate the refractive indices of different modes in the SMF and MMF with tolerable computational complexity, we assumed the fibers to satisfy the weakly guiding condition and the orthogonal modes supported by the fibers are linearly polarized modes (LP modes) [51]. The fiber characteristic equation used for calculation of the effective refractive index n_{eff} is given by [51]

$$\frac{J_l(u)}{uJ_{l-1}(u)} + \frac{K_l(w)}{wK_{l-1}(w)} = 0 \tag{3.39}$$

where $J_l(x)$ is the Bessel function of the first kind, and $K_l(x)$ is the modified Bessel function of the second kind, l corresponds to the azimuthal number of the mode (in our case $l=0$, see discussion in 3.2.2), $u=(2\pi a/\lambda)(n_1^2-n_{eff}^2)^{1/2}$, $w=(2\pi a/\lambda)(n_{\text{eff}}^2-n_2^2)^{1/2}$, in which a is the radius of the fiber core, n_1 and n_2 are the refractive indices of the fiber core and cladding, respectively.

In order to calculate the mode coupling coefficient $\eta_k = \left| \iint_{R_1} \phi_0 \phi_k^* dxdy \right|$, in which ϕ_0 is the mode profile for the fundamental mode in the SMF, and ϕ_k is the *k*th mode profile in the MMF, we applied the mode profile formula [51]:

$$\phi_k = \begin{cases} AJ_0\left(u_k r/a\right)/J_0\left(u_k\right), r < a \\ AK_0\left(w_k r/a\right)/K_0\left(w_k\right), r > a \end{cases} \tag{3.40}$$

where k denotes the kth root of Eq.3.39 and the value of A can be obtained by the normalization condition: $\left| \iint_{R_1} \phi_k \phi_k^* dxdy \right| = 1$.

Another approximation used to simplify the calculation is to consider only inter-modal dispersion in the MMF, the intra-modal dispersion (which accounts for the fact that n_{eff} of each mode also depends on wavenumber k) is ignored; this is a reasonable assumption because in real applications one obtains the spectral information only in a narrow spectral range (for example, in our simulations and experiments, from 1520 to1570 nm) in which n_{eff} can be regarded as a constant.

Equation 3.31 will be applied for simulation of quantities that induce only fiber dimensional change while setting p_e to a constant and Eq.3.32 will be applied for simulation of the temperature effect when dimensional and refractive indices changes coexist. The fiber parameters used for all the simulations are: step-index MMF with n_{core}=1.448, n_{clad}=1.434, r_{core}=25um, excited by step-index SMF with n_{core}=1.445, n_{clad}=1.440, r_{core}=4.2um.

Physical meaning of the OPD dependant phase term

By using Eq.3.34 to estimate the *OPD* or equivalently, the angular speed of the total phase with k, one assumes that the rotational speed (*OPD*) is a constant such that least-square (LS) linear fitting gives the best estimation. As concluded in 3.3.1, the measurable (obtainable) rotational speed is actually represented by the rotation of the effective vector Σ. From the discussion in 3.3.1, the rotational speed of this vector depends on the alignments of all the mode vectors υ_k; at a constant *OPD*, all the mode vectors (υ_k) rotate

at different but constant speeds, resulting in evolution of the relative alignments of the mode vectors, and the rotational speed of the vector Σ will undergo a change as k increases. This means the rotation of the effective vector has acceleration. As shown clearly in Figure 3.12, the phase change is not linearly related to k. If we carry out LS linear fitting applying Eq.3.34, instead of getting fitting errors evenly distributed around zero (which corresponds to a constant rotation speed), the fitting error shows a dispersive pattern. This is illustrated in Figure 3.14.

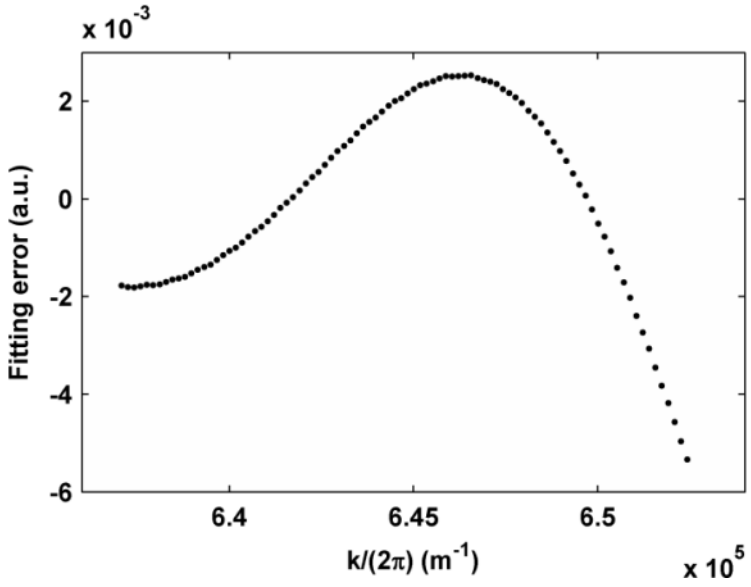

Figure 3.14. Simulated linear fitting error as a function of wavenumber.

Because the rotational speed of the effective vector is affected strongly by the relative alignments of all the mode vectors, the best one can do is to look at the spectrum and estimate its speed by linear fitting. As a result, the first step estimation $OPD^{(1)}$ can be misleading: the cavity can appear to be longer, or shorter than it really is, if the observation is made simply based on looking at the interference spectrogram generated by the cavity. Consequently, if Eq.3.35 is used to predict the peak positions, large phase error can occur; as the OPD changes, the relative alignments of the mode vectors also change, resulting in varying 'estimation quality' of the OPD, and the additional phase term will vary accordingly.

OPD change solely due to fiber dimensional change was studied by computer simulation, the cavity length was changed from 2000μm to 2010μm; at a given cavity length, the total phase difference between the real spectrum and predicted spectrum based on $OPD^{(1)}$ was calculated; for the cavity length range studied, this phase difference was plotted as a function of the cavity length. During the simulation, no noise was added to the signal in order to remove phase ambiguity generated by external noise. As shown in Figure 3.15, a nearly $-\pi$ phase change occurred during this process.

Assume that during the above simulated experiment, the exact value of the cavity length is known in advance. Based on the OPD estimation result, we are able to calculate the effective index of the cavity by $n_{eff}=OPD^{(1)}/(2L)$, where $OPD^{(1)}$ is the first-step OPD estimation, and L is the physical cavity length. In principle the value of n_{eff} should not vary during the simulation process because all the refractive indices were set to constants; however, as discussed previously, the information obtained by looking at the spectrum can be misleading because the estimation of n_{eff} indeed varied a lot. In Figure 3.16, the estimated n_{eff} was plotted as the cavity length increases from 500 to 2500μm while all the refractive indices of the fibers were kept constant. As shown in the figure, the variation in the measured effective refractive index is significant in this process.

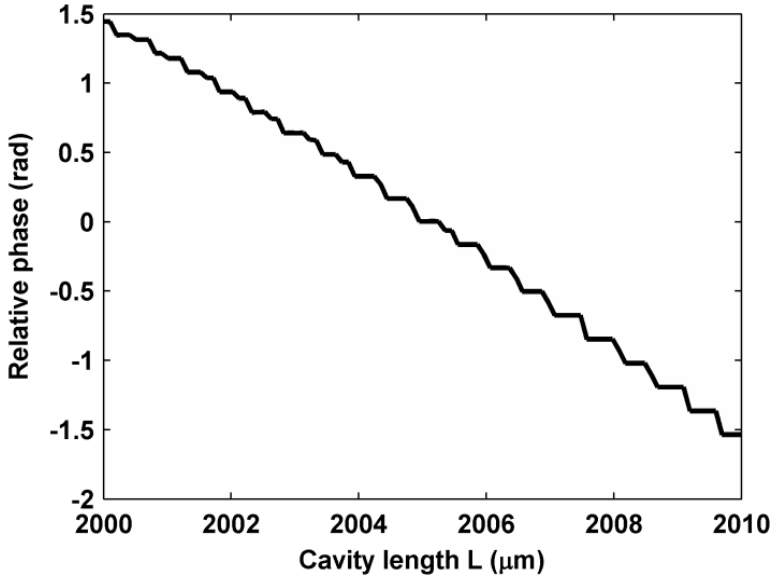

Figure 3.15. Computer simulated relative phase change as cavity length increases.

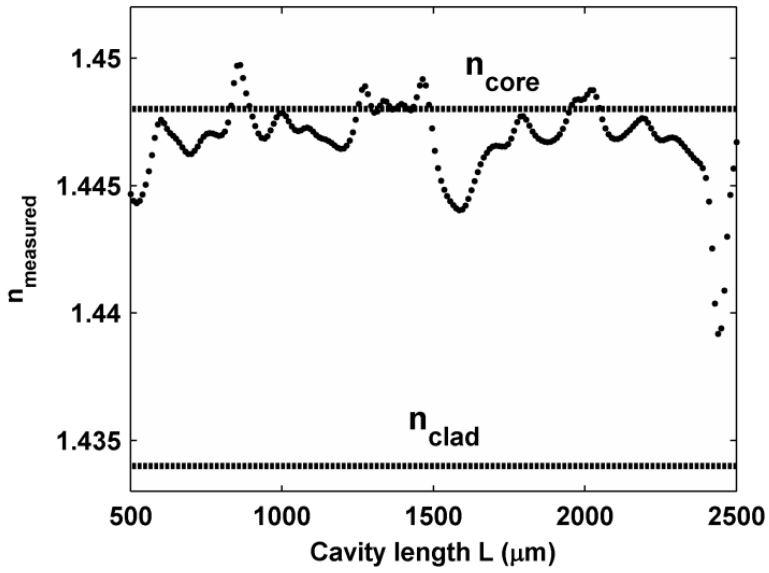

Figure 3.16. Estimated n_{eff} as the cavity length increases while all the refractive indices stay unchanged. Two horizontal lines mark the refractive indices of the MMF core and cladding.

Based on Eq.3.29, the total phase can be expressed as:

$$\varphi = \angle\Sigma = \angle\left\{\sum_{k=1}^{N} \eta_k^2 \exp\left[j\left(2kLn_k\right)\right]\right\} \tag{3.41}$$

We can approximate the rotational speed of the total phase with respect to k by:

$$\frac{d\varphi}{dk} = \frac{d\varphi}{d(kL)}\frac{d(kL)}{dk} \approx 2\overline{n}_{est}L = OPD^{(1)} \tag{3.42}$$

where $\overline{n}_{est}$ is the estimation of the effective refractive index. From Eq.3.42, we have $\frac{d\varphi}{d(kL)} = 2\overline{n}_{est}$. Also, similar to Eq.3.42, the following equation can be obtained:

$$\frac{d\varphi}{dL} = \frac{d\varphi}{d(kL)}\frac{d(kL)}{dL} \approx 2\overline{n}_{est}k \tag{3.43}$$

Base on Eq.43, we have:

$$d\varphi \approx d(2k\overline{n}_{est}L) = 2k\left(Ld\overline{n}_{est} + \overline{n}_{est}dL\right) \approx 2k\overline{n}_{est}dL \tag{3.44}$$

The total phase term can be estimated with better accuracy to be

$$\varphi_1 \approx \int_0^L 2k\bar{n}_{est}dl \tag{3.45}$$

while the total phase is routinely predicted by:

$$\varphi_2 = 2k\bar{n}_{est}L \tag{3.46}$$

The relationship between φ_1 and φ_2 can be graphically illustrated as shown in Figure 3.17. Because the increasing rate of the total phase is not constant, using Eq.3.46 to estimate the total phase will result in an additional phase term, and this error term keeps changing with increasing L. If the OPD change during the full measurement is small, the slope of the total phase change in that range can be regarded constant, whereas the additional phase term will change very little accordingly; for applications where the change of OPD is large so that the slope can no longer treated as constant, the additional phase term will change with OPD. The total phase difference is illustrated in Figure 3.17 according to Eqs. 3.45 and 3.46.

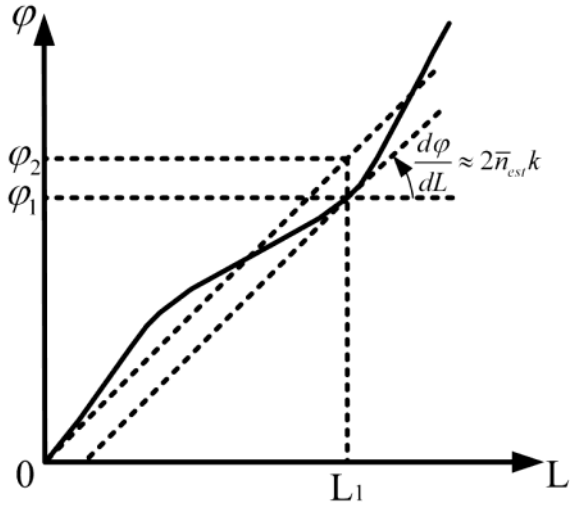

Figure 3.17. Graphical explanation of the additional phase term

From Figure 3.17, the OPD dependent phase term appears as a result of non-constant slope of the φ-L curve, which is equivalent to a non-constant $\bar{n}_{est}$. Based on Eqs.3.45 and 3.46, the phase estimation difference as a function of cavity length L is plotted in Figure

3.18. To emphasize the relationship between the phase difference and the non-constant value of the estimated n_{eff}, the range of L is set to the same as that in Figure 3.16. Shown clearly in Figure 3.18 is the strong relationship between the change rate of the additional phase and the value of the estimated n_{eff}. At regions where n_{eff} changes rapidly, the additional phase term also changes rapidly. Also evident from Figure 3.18 is the fact that there are regions where the phase changes very slowly. These regions are good for sensor application. There are also bad regions in which the phase changes rapidly, working in such regions will lead to large errors and even measurement failure.

Not only the physical dimension but also the refractive indices of the MMF will be varied during temperature measurement, which adds additional complexity problem to the sensor signal demodulation. To have a better understanding of the temperature dependent phase term, a similar procedure can be followed as in the previous example. By employing Eq.3.32 and Eq.3.42, we get

$$\frac{d\varphi}{dT} = \frac{d\varphi}{dOPD^{(1)}} \frac{dOPD^{(1)}}{dT} \approx k\left(\alpha_T + \sigma_T\right) OPD^{(1)} \tag{3.47}$$

It is straightforward to obtain a better estimation of the phase term by integrating Eq.3.47:

$$\Delta\varphi_1 \Big|_{T_1}^{T_2} \approx k\left(\alpha_T + \sigma_T\right) \int_{T_1}^{T_2} OPD^{(1)}(T) dT \tag{3.48}$$

This estimation is more accurate than the direct estimation by:

$$\Delta\varphi_2 \Big|_{T_1}^{T_2} = k\left(OPD^{(1)}(T_2) - OPD^{(1)}(T_1)\right) \tag{3.49}$$

To simulate the temperature induced phase shift, a computer simulated experiment was performed using a 4 mm cavity, temperature was increased to 600ºC from room temperature, and two methods were applied to obtain the total phase change as a function of temperature. The first approach compared the real phase with the predicted phase (by inserting $OPD^{(1)}$ into Eq.33), the second approach directly compared the value of Eqs.48 and 49. The results are provided in Figure 3.19. The results obtained by these two approaches agree well except a little discrepancy in their magnitudes.

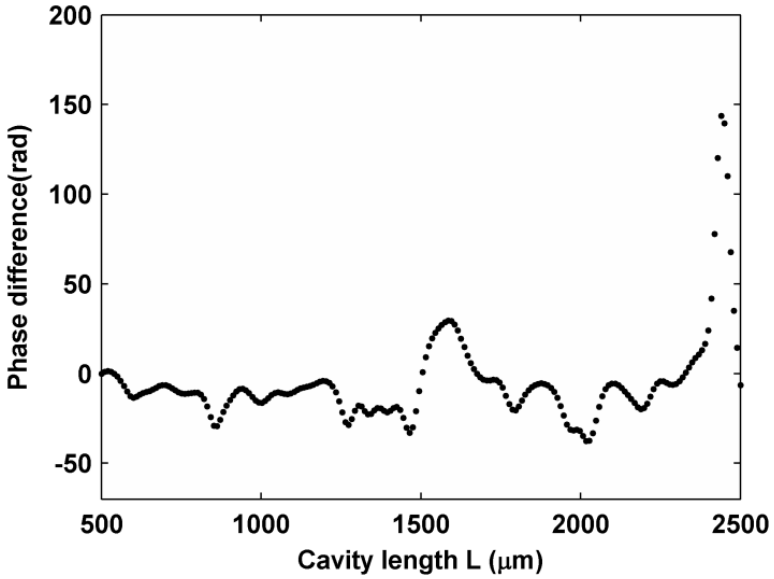

Figure 3.18. Phase difference as a function of cavity length

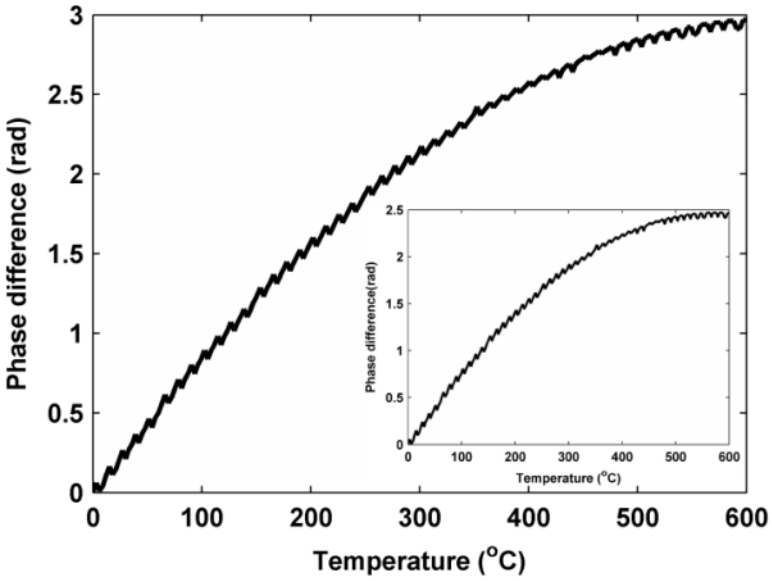

Figure 3.19. Phase difference as a function of temperature, measured by direct comparison of the predicted spectrum and the real spectrum. Inset: measured by using Eqs.3.48 and 3.49.

3.3.3 Verification of the additional phase

The mode theory is extended in this subsection to treat the graded-index fiber (GI-MMF) based SMS-IFPI, the field expression has been developed in 3.2.2. The spectrum of the SMS-IFPI, normalized with respect to the input power, is expressed as

$$I = R\left|1-\sum_{m=1}^{N} c_m{}^2 \exp\left(-j2\beta_m L\right)\right|^2 \tag{3.50}$$

where R is the reflectivity of the splicing point and L is the length of the FP cavity. For WLI based signal demodulation, the optical path difference (OPD), defined as

$$OPD = 2\overline{n}L \tag{3.51}$$

is found by estimating the frequency of the spectrogram [21], in which $\overline{n}$ is the estimated index. By removing the phase term associated with $\overline{n}$ out of the superposition in Eq.3.50 and rearranging the rest terms, applying Eq.3.19 for GI-MMF, the spectrum is subsequently found as

$$I = R\left[1+\left|\xi\right|^2+2\left|\xi\right|\cos\left(2\overline{n}k_0 L+\theta+\pi\right)\right] \tag{3.52}$$

where the complex variable ξ is defined by

$$\xi = \left|\xi\right|e^{j\theta} = \exp\left[j2\delta_n k_0 L\right]\cdot$$

$$\sum_{m=1}^{N} c_m{}^2 \exp\left[-j2\left(m-1\right)k_0\Delta_n L\right] \tag{3.53}$$

with $\delta_n = n_{e,1} - \overline{n}$ being the difference between the estimated index and the highest effective index of the MMF. The absolute value of ξ affects the fringe visibility of the spectrum as

$$FV\left(L\right) = \frac{2\left|\xi\right|}{1+\left|\xi\right|^2} \tag{3.54}$$

The additional phase term θ, which plays very important role in WLI signal processing [60], is defined by the phase of ξ. This additional phase, according to Eq.3.53, is

composed of two terms, a linear term (with respect to L) associated with δ_n and an oscillatory one associated with the superposition term. Our numerical analysis for both GI-MMF and SI-MMF yields several conclusions regarding the phase terms in Eqs.3.52 and 3.53. Because c_1 is typically significantly larger than the rest of the coupling coefficients, the oscillatory phase is trivial compared with the linear phase in Eq.3.53. For GI-MMF, the index difference δ_n is stable with L, in contrast to the case of SI-MMF in which δ_n changes drastically. As a result, for GI-MMF, the additional phase term θ changes nearly linearly with L (slope defined by the linear phase term in Eq.3.53 with little ripples superimposed. Such phenomena are illustrated in Figure 3.20, where the additional phase term in the spectrum of a SMS-IFPI employing MMF2, as a function of cavity length is plotted. The phase term of an IFPI employing a SI-MMF, with all the fiber parameters identical to MMF2 is also plotted for comparison. In plotting these curves, for both GI-MMF and SI-MMF, one thousand spectrums were created based on Eq.3.50, with L evenly distributed from 500 to 3500 μm and the other parameters fixed. Then, the OPD estimation algorithm in [60] was applied for both groups of data to calculate the phase terms, and the results were plotted as a function of cavity length.

Equation 3.53 indicates that the additional phase term in the SMS-IFPI sensor spectrum Eq.3.52 is composed of two parts. The linear part $2\delta_n k_0 L$ is generated by the difference between the refractive index of the MMF fundamental mode ($n_{e,1}$) and the estimated refractive index ($\overline{n}$), denoted as δ_n. For GI-MMF, δ_n is stable, and the contribution by $2\delta_n k_0 L$ is almost linear with L. The other component in the additional phase is

$$\theta_{osc}(L) = \angle\left\{\sum_{m=1}^{N} c_m{}^2 \exp\left[-j2(m-1)k_0\Delta_n L\right]\right\} \tag{3.55}$$

which oscillates around zero with small amplitude due to the dominant coupling coefficient c_1 in the superposition. As such, replacing θ with $2\delta_n k_0 L$ provides reasonably good approximation for the additional phase. Furthermore, the linear term can be written as $(\delta_n/\overline{n})k_0 OPD$, upon which we take the derivative with respect to OPD, and get

$$\frac{d\theta}{dOPD} \approx \frac{\delta_n}{\overline{n}} k_0 \tag{3.56}$$

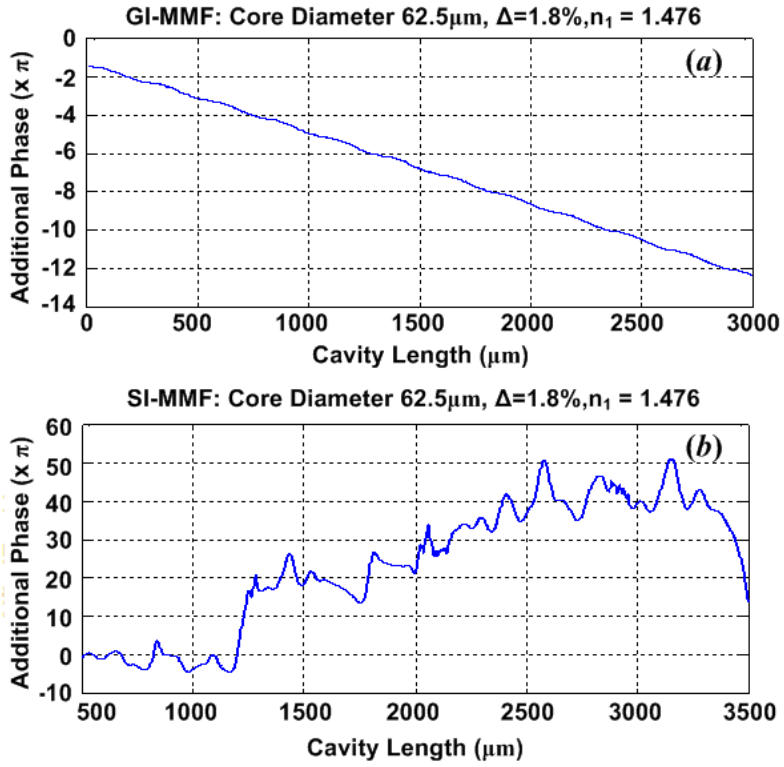

Figure 3.20. The evolution of the additional phase term θ with cavity length L. (a) The additional phase term in GI-MMF (MMF2). (b) The additional phase term in SI-MMF, whose parameters are identical to MMF2.

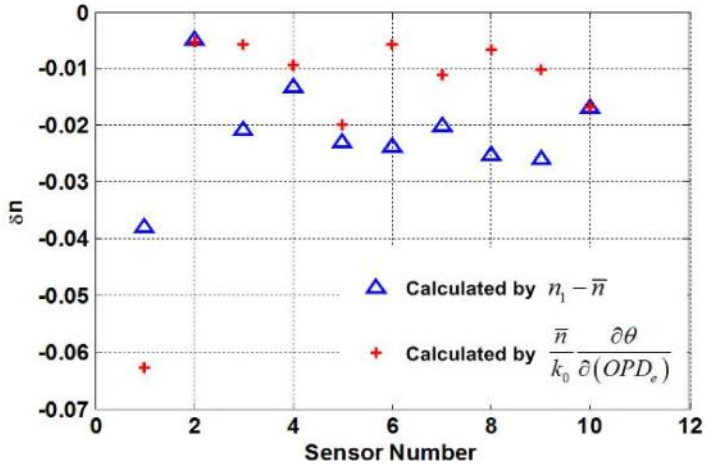

Figure 3.21. Verification of the analysis of the additional phase term θ in (26). The experimental demonstration is achieved by comparing the estimation of δ_n by two approaches for ten sensors multiplexed in a link.

In real measurement, OPD can be estimated with very high accuracy as OPD_e, and θ can also be estimated by the algorithm. Thus the value of $d\theta/dOPD$ is readily obtained after the sensor is calibrated. Because L can be controlled during sensor fabrication with accuracy of $\pm$ 5μm, the value of $\overline{n}$ is estimated by $OPD_e/2L$. From Eq.3.56 the value of δ_n is obtained as $\delta_n = \overline{n}\,(\,d\theta/dOPD)/k_0$.

On the other hand, from the numerical model described in 3.2.2, the calculation of the effective indices of the excited modes of MMF2 provides estimation of $n_{e,1}$, and an alternative estimation of δ_n is readily obtained by its definition $\delta_n = n_{e,1} - \overline{n}$. In Figure 3.21, the δ_n values of the IFPI sensors in the link whose Fourier spectrum is depicted as the solid curve in Figure 3.7 (a) are calculated using the above two methods and co-plotted. The figure shows acceptable accuracy, and the discrepancies are attributed to the uncertainties associated with the estimation of θ, OPD, $\overline{n}$ and $n_{e,1}$.

According to Eq.3.56, the additional phase is proportional to OPD and δ_n. A non-constant additional phase will potentially lead to abrupt discontinuities in the demodulated signal, as analyzed in [60]. As a result, minimizing the value of $d\theta/dOPD$ is essential for reliable sensor performance. As predicted by Eq.3.56 and demonstrated in Figure 3.21, the longer the cavity length, the larger the total additional phase change.

To experimentally visualize the additional phase evolution, a SMS-IFPI sensor was fabricated by fusion splicing a section of MMF (Thorlabs, MMF 625) sandwiched between two SMFs (Corning SMF-28). The OPD of the sensor was measured to be around 7730μm. The reflection spectrum of the sensor was monitored by a spectrometer (Component Testing System, Micron Optics Inc., Si-720) from 1520nm to 1570nm with 2.5pm spectral resolution. The sensor was heated by a home-made mini-furnace; the temperature of the sensor was measured by a thermocouple with 0.1ºC resolution. The temperature was controlled to scan continuously from room temperature to 600 ºC for multiple times and interference spectra were obtained at 25 ºC interval. From each spectrogram recorded, the first-step OPD estimation was performed to obtain $OPD^{(1)}$, and based on the first step predicted value, the total phase was estimated and compared with the phase of the real data to calculate the additional phase term. Figure 3.22 plots the additional phase term as a function of OPD. A phase change up to $-\pi$ was observed.

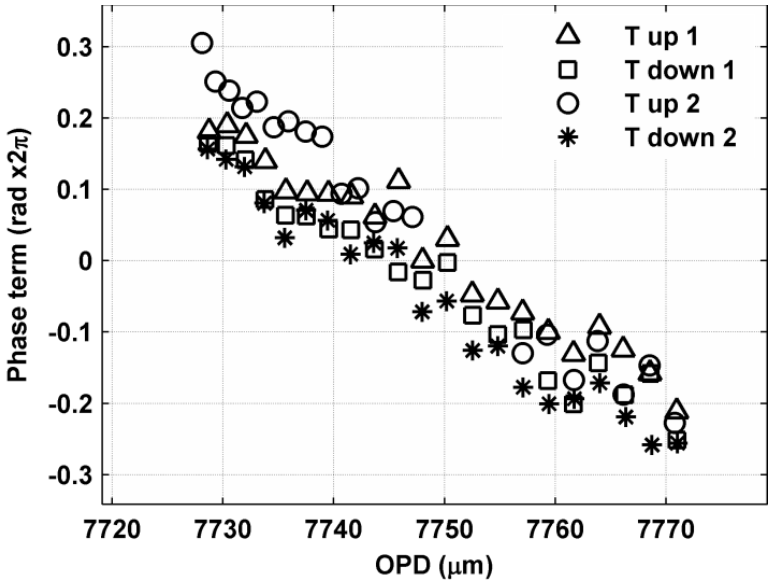

Figure 3.22. Additional phase term as a function of OPD.

3.4 Signal processing of IFPI sensors

A variety of signal demodulation algorithms have been developed for FP sensors, most of which are designed to measure optical path difference (OPD) from the sensor's reflected interference spectrum, where OPD is determined by the refractive index n and physical length L of the sensing cavity.

$$OPD = 2nL \tag{3.57}$$

To interrogate a low-finesse FP sensor, the phase of the periodic fringe pattern (Eq.3.58) is measured at either a fraction or all of the sampling points in the spectrogram. This interference spectrum is represented by $S(k)$, where $k=2\pi/\lambda$ is the optical wavenumber, λ is the wavelength, $\Phi(k)$ is the total interferogram phase, and φ_0 is an additional phase term caused by beam reflection and propagation (see 3.3.1).

$$\begin{aligned} S(k) &\propto \cos\left[\Phi\left(k\right)\right] \\ \Phi\left(k\right) &= k \cdot OPD + \varphi_0 \end{aligned} \tag{3.58}$$

As a transducer, the sensor is designed to relate the measurand to OPD with high sensitivity and repeatability.

The goal of signal demodulation is to extract OPD from the spectral interferogram, thereby making a physical measurement. As they take a succession of measurements in time, practical FP sensors often experience abrupt jumps in demodulated OPD.

These jumps, which are often more pronounced in IFPI sensors, are a symptom of ambiguity in fringe order estimation during the demodulation process, the cause of which has traditionally been attributed to noise [27, 40]. In other words, as long as the noise in the system is suppressed to a sufficiently low level, the fringe-order ambiguity problem is not supposed to appear. However, the experiments described in 3.4.1 have shown such phase jumps to occur in sensors with signal to noise ratio (SNR) as high as 30dB, indicating that factors other than system noise contribute to the phase jump phenomenon. Section 3.4.2 analyzes the cause of these spurious signal jumps, and 3.4.3 presents a novel sensor demodulation algorithm designed to mitigate the phase ambiguity problem. Testing and results of the algorithm are presented in 3.4.4.

3.4.1 Initial phase jump experiment

The SMS-IFPI sensors investigated were fabricated by fusion splicing a short section of multimode fiber (MMF, Corning Infinicore 50/125) into a longer section of single mode fiber (SMF, Corning SMF-28e). The IFPI sensors operate on the weak reflections generated by the small refractive index difference between the SMF and MMF fiber cores.

The sensors were interrogated using a swept-laser interrogation system (Micron Optics Si-720) over a spectral range of 1520-1570nm with spectral resolution of 2.5pm, dynamic range of 70dB, and a scanning rate of 0.5Hz. Each collected spectrum was processed using a peak tracking method, in which local curve fitting is used to identify the exact locations of every fringe peak in the interferogram, and their corresponding fringe orders are determined to measure OPD [39, 42]. The additional phase term φ_0, defined in Eq.3.58, is assumed to be constant in this algorithm.

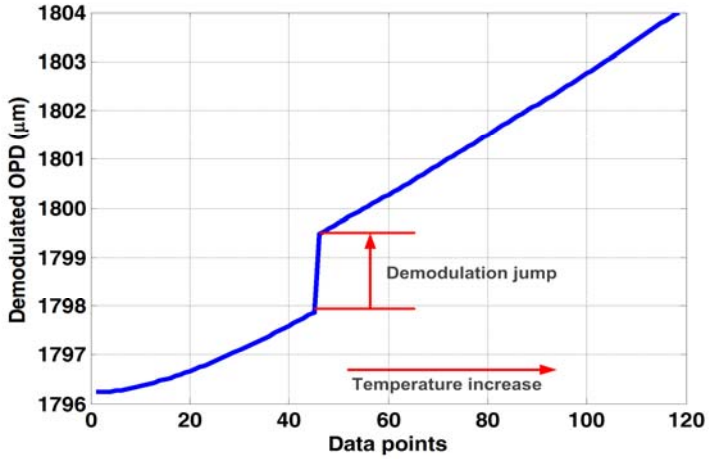

Figure 3.23. Output of a high-quality SMS-IFPI sensor under smoothly increasing temperature. When interrogated using traditional OPD techniques, the sensor experiences an abrupt jump in its demodulated signal.

Table 3.5. Key variables used in the analysis.

$\Phi(k)$	Total phase of spectrum (rad)
$OPD^{(0)}$	Initial reference optical path difference (μm)
$OPD^{(1)}$	Altered OPD after change in measurand (μm)
$k_m^{(0)}$	m^{th} fringe peak wavenumber in initial spectrum (rad/μm)
$k_m^{(1)}$	m^{th} fringe peak wavenumber in altered spectrum (rad/μm)
φ_0	Initial phase of spectrogram (rad)
$\Delta\varphi_0$	Change in initial phase during measurement (rad)
m	Integer fringe order
$n^{(1)}$	Integer shift in fringe order after change in measurand
ψ	Total phase shift between initial & altered spectra (rad)
$\Delta\psi$	Error in measured value of total phase shift ψ (rad)

Several sensors were fabricated and tested under continuously-increasing temperature in a tube furnace. Figure 3.23 clearly shows the OPD of a high-quality sensor beginning to lengthen as the temperature increases. However, even with a SNR of greater than 30dB, the sensor experiences an abrupt jump in its measured OPD. From these results, it is clear that noise is not the sole cause of the OPD discontinuity problem. Section 3.4.2

presents detailed analysis to show that a time-varying initial phase φ_0 is the primary source of the observed OPD jumps.

3.4.2 Analysis of demodulation jumps

Non-constant phase-induced OPD demodulation jumps

The key parameters used in this subsection are listed in Table 3.5. In traditional OPD-based demodulation, the additional phase term φ_0 in Eq.3.58 is usually assumed to be constant during measurement process and needs to be pre-calibrated [27, 39]. However, physical changes in both EFPI and IFPI sensors can cause this term to vary during measurement (see 2.3.6, 3.3.1). In order to better expose the influence of the phase shift on the demodulation process, the analysis begins with recording a reference spectrum and tracking the spectral changes relative to it. At a reference measurement condition (e.g., room temperature), the following equation holds as a result of Eq.3.58:

$$OPD^{(0)}\left[k_m^{(0)}\right]_{N\times 1} + \varphi_0\left[I\right]_{N\times 1} = 2\pi\left[m\right]_{N\times 1} \tag{3.59}$$

where $[k_{\mathrm{m}}^{(0)}]$ denotes a vector containing the N wave-numbers corresponding to N peak positions in the interference spectrum, $[m]$ denotes their corresponding fringe-orders, and $[I] = [1,1,\ldots 1]^{\mathrm{T}}$. At another measurement condition, both the OPD and the phase in the spectrum are modified by the change of the measurand, and accordingly Eq.3.59 evolves into the following equation:

$$OPD^{(1)}\left[k_m^{(1)}\right]_{N\times 1} + \varphi_0\left[I\right]_{N\times 1} + \Delta\varphi_0\left[I\right]_{N\times 1} =$$

$$2\pi\left[m\right]_{N\times 1} + 2\pi n^{(1)}\left[I\right]_{N\times 1} \tag{3.60}$$

where $\Delta\varphi_0$ accounts for the additional phase change and $n^{(1)}$ is an integer denoting the fringe-order shift. By dividing Eq.3.59 by Eq.3.60, the following equation for estimating the modified OPD is obtained:

$$\left[OPD_m^{(1)}\right]_{N\times 1} = \left[k_m^{(0)} / k_m^{(1)}\right]_{N\times 1} OPD^{(0)} + \psi\left[1/k_m^{(1)}\right]_{N\times 1} \tag{3.61}$$

where $\psi = 2\pi n^{(1)} - \Delta\varphi_0$ represents the fringe order shift relative to the reference interferogram, and [$OPD_m^{(1)}$] denotes a total of N OPD values estimated from the N fringe peaks. The OPD can then be defined such that the variance of [$OPD_m^{(1)}$] is minimized, calculated by:

$$\frac{\partial V}{\partial \psi} = \frac{\partial\left[\sum_{m=1}^{N}\left(OPD_m^{(1)} - \overline{OPD_m^{(1)}}\right)^2\right]}{\partial \psi} = 0 \tag{3.62}$$

In an ideal case, the above variance is zero so that the right-hand side (R.H.S.) of Eq.3.61 gives a constant C for any fringe order m:

$$\frac{k_m^{(0)}}{k_m^{(1)}} OPD^{(0)} + \frac{\psi}{k_m^{(1)}} = \mathbf{C} \tag{3.63}$$

If an estimation error exists such that the measured phase shift becomes $\psi' = \psi + \Delta\psi$, and the estimated OPD becomes:

$$OPD_m^{(1)} = \frac{k_m^{(0)}}{k_m^{(1)}} OPD^{(0)} + \frac{\psi}{k_m^{(1)}} + \frac{\Delta\psi}{k_m^{(1)}} \tag{3.64}$$

By substituting (7) into (8), the estimated OPD in the presence of phase error becomes:

$$OPD_m^{(1)} = \mathbf{C} + \frac{\Delta\psi}{k_m^{(1)}} = \mathbf{C} + \frac{\Delta\psi}{2\pi}\lambda_m \tag{3.65}$$

As a result, instead of being a constant, the estimated OPD tends to increase or decrease almost linearly with fringe-order (the $OPD_m^{(1)}$ vs. m curve becomes tilted), and the slope of the tilt is given by κ :

$$\kappa = \frac{OPD_{m+1}^{(1)} - OPD_m^{(1)}}{m+1-m} = -\frac{\Delta\psi}{2\pi}\left(\lambda_m - \lambda_{m+1}\right) = \xi \cdot \Delta\psi \tag{3.66}$$

In Eq.3.66, the term $\xi = (\lambda_{m+1}-\lambda_m)/2\pi$ is a constant relating the $OPD_m^{(1)}$ vs. m tilt angle and the phase estimation error. If the signal demodulation algorithm assumes the phase term φ_0 in Eq.3.58 to be a constant, which suggests that $\Delta\varphi_0=0$ in Eq.3.60, such an

assumption leads to a phase error $\Delta\psi=\Delta\varphi_0$, and consequently, results in tilting of the $OPD_m^{(1)}$ vs. m curve with resulting slope κ defined by Eq.3.66.

The tilt angle ξ can be obtained directly from the spectrum by identifying the wavelength positions of adjacent peaks.

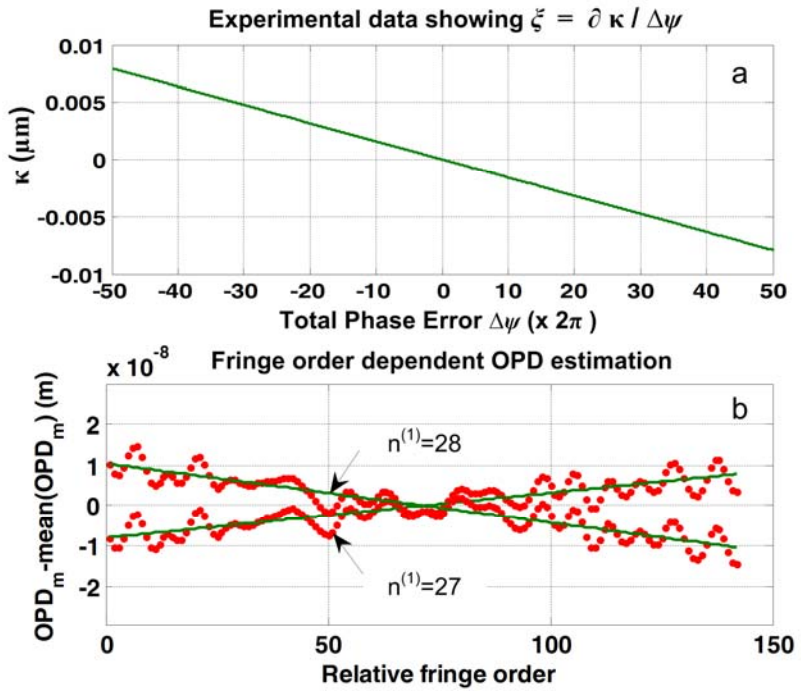

Figure 3.24. (a) Slope κ of the $OPD_m^{(1)}$ vs. m curve as a function of phase estimation error Δ (b) An example of the tilting at a phase shift $\Delta\varphi \approx \pi$, given by the $OPD_m^{(1)}$ vs. m curves for $n^{(1)} = 27$ and $n^{(1)} = 28$.

Figure 3.24 (a) plots the calculated slope as a function of the total phase error from experimentally-obtained IFPI spectral data. After identifying the peaks in the spectrum, the total phase shift ψ in Eq.3.61 was scanned over a broad range by increasing the temperature of the IFPI sensor. Upon inserting each ψ value into the R.H.S. of Eq.3.61, a series of $OPD_m^{(1)}$ values were obtained, and κ was calculated by linear fitting these values to the fringe order m.

As long as $\Delta\varphi_0<\pi$ and noise is sufficiently low that peak positions can be determined accurately, this erroneous assumption of constant initial phase does not cause a jump in

the demodulated OPD. Under these ideal conditions, the fringe-order shift $n^{(1)}$ in Eq.3.60 can be uniquely determined by minimizing $|\kappa|$ in Eq.3.66 without hopping to its nearest integers. However, once $\Delta\varphi_0$ reaches π, two adjacent $n^{(1)}$ values generate two possible solutions for κ with identical absolute values but opposite signs. This degeneracy can cause a demodulation jump to take place at the point where $n^{(1)}$ jumps to a neighboring value.

This inherent fringe order estimation ambiguity problem is demonstrated by analyzing the experimental spectral data near an OPD jump point. Shown in Figure 3.24 (b), when φ_0 is assumed to be constant, it is impossible to distinguish whether the spectrum has shifted 27 or 28 orders from the reference spectrum. Figure 3.24 (b) illustrates the relationship between the ambiguity in minimization of the slope κ and calculating the value of fringe order shift $n^{(1)}$.

Origins of the non-constant phase term

This work investigates two primary causes of variation in spectrogram initial phase: multimode excitation in the sensor cavity and finite-rate scanning of the interrogation wavelength. In both cases, contributions to the varying initial phase are represented by $\Delta\varphi_0$.

In the case of optical fiber EFPI sensors, mode-induced variations in initial phase occur when the wave-front distorted optical wave propagating in free space couples back into fiber core modes [40]. In IFPI sensors, similar modal coupling issues can occur in the multi-mode fiber section that makes up the FP cavity, resulting in an OPD-dependent phase term (see 3.3.1) [59]. The changes of the phase terms of IFPI sensors are generally much greater than that of the EFPIs during measurement processes, as a result of much larger OPD changes. The general expression for a spectrogram obtained from an IFPI sensor is given by Eqs.3.67 and 3.68.

$$I = r^2 \left| 1 + \sum_{n=1}^{N} \left|\eta_n\right|^2 e^{jk \cdot OPD_n} \right|^2 = r^2 \left| 1 + \eta_{eff}^2 e^{jk \cdot OPD_{eff}} \right| \tag{3.67}$$

$$|\eta_n|^2 = \left| \iint_{R_1} \mathrm{A}_0 \, \mathrm{A}_n^* \, dxdy \right|^2 \tag{3.68}$$

In the above expressions, r denotes the amplitude reflectivity at each interface, and $|\eta_n|^2$ is the power coupling coefficient from the fundamental mode of the SMF to the n^{th} mode in the MMF, the normalized mode profiles of which are represented by A_0 and A_n, and the integration in Eq.3.68 is performed on the entire fiber cross-section R_1. OPD_n is the effective round-trip optical cavity length of the n^{th} mode, which is determined by the effective refractive index of that mode and the physical cavity length. From Eq.3.67 the spectrogram is a superposition of N mode vectors representing each mode excited in the MMF section. The superposition results in a rotating effective vector with amplitude η_{eff}^2 and frequency OPD_{eff} (3.3.1). If τ represents the measurand (strain, temperature, etc.), the total phase change of the spectrogram when τ changes from τ_1 to τ_2 can be estimated by:

$$\psi_1 \approx k \frac{\partial \ln\left(2n_c L\right)}{\partial \tau} \int_{\tau_1}^{\tau_2} OPD_{eff}\left(\tau\right) d\tau \tag{3.69}$$

In Eq.3.69, n_c denotes the refractive index of the MMF core (assuming step-index MMF), L is the physical length of the cavity, the $\partial/\partial\tau$ term represents a constant describing the dependence of the OPD on the parameter to be measured (e.g., if τ represents temperature, the $\partial/\partial\tau$ term is the sum of the coefficient of thermal expansion (CTE) and thermo-optic coefficient (TOC); if τ represents strain, that term equals $1\text{-}p_e$, where p_e is the effective strain-optic constant).

If the spectrogram initial phase φ_0 is assumed to be constant throughout the measurement process, when τ changes from τ_1 to τ_2, the estimated total phase change is:

$$\psi_2 = k\left(OPD_{eff}\left(\tau_2\right) - OPD_{eff}\left(\tau_1\right)\right) \tag{3.70}$$

The additional phase shift is due to multimode excitation is given by the difference between mode-dependent total phase shift ψ_1 and the approximate total phase shift ψ_2, the latter of which assumes constant initial phase:

$$\Delta\varphi_0 = \Delta\psi_{\text{modal}} = \psi_1 - \psi_2 \tag{3.71}$$

Equations 3.67~3.71 lead to the conclusion that if there is more than one mode excited in the MMF cavity, Eq.3.71 results in a non-zero additional phase shift. Furthermore, an increased proportion of energy carried by higher order modes results in a more significant shift in initial phase $\Delta\varphi_0$.

According to 3.4.2, once this term exceeds π, it results in a jump in the demodulated OPD. Section 3.4.4 contains simulated and experimental demonstrations of multimode-induced $\Delta\varphi_0$, which show that the multimode nature of the IFPI cavity can produce uncontrolled phase shifts of 1.2π or greater.

In addition to modal excitation, finite sampling rate of the spectrometer also contributes to varying initial phase. Assuming the OPD of the sensor changes with speed R (nm/second) and it takes the data acquisition unit S seconds for a single scan of the probe wavelength over the spectral range, the OPD change during each scan is given by $\Delta OPD = R \cdot S$ [nm]. The expression for total phase in Eq.3.58 is accordingly modified to:

$$\Phi(k) = \left[OPD_1 + \frac{R \cdot S}{\Delta k}(k_1 - k) \right] k + \varphi_0 \tag{3.72}$$

where OPD_1 and k_1 are the OPD and wavenumber at the beginning of each scan, Δk is the spectral range of the spectrometer, and φ_0 represents the initial phase term generated by any other effects. The variation in initial phase $\Delta\varphi_0$ caused by the sampling can be calculated from Eq.3.66, while the L.H.S. of Eq.3.66 can be well estimated by $\Delta OPD/N = R \cdot S/N$ where N is the number of fringes in the interference spectrum. The term $\Delta\psi$ in R.H.S. of Eq.3.66 can be treated as the phase error caused by the finite sampling rate. It is then straightforward to obtain the initial phase shift $\Delta\varphi_0$ due to finite sampling rate using Eq.3.72, where k_0 is the central wavenumber:

$$\Delta\psi = \Delta\varphi_0 \approx \frac{RSk_0^2}{\Delta k} \tag{3.73}$$

Similar to the case for multimode-induced phase shifts, simulations in 3.4.4 show that finite-rate sampling can produce an unwanted phase shift of π or greater.

3.4.3 Total phase interrogation method

In order to avoid jumps caused by the inherent fringe-order ambiguity problem, the additional phase shift $\Delta\varphi_0$ in Eq.3.60 can no longer be treated as zero. Instead, the varying phase term $\varphi_0(\tau) = \varphi_0 + \Delta\varphi_0(\tau)$ in Eq.3.58 needs to be estimated for each measurement. The following algorithm is designed specifically to achieve the required dynamic recalculation of $\varphi_0(\tau)$. We begin by re-arranging Eq.3.59 into the following form, in which the functional dependence on τ is explicitly stated and the fringe order integers are expressed such that $[m(\tau)]_{N\times1} = [0, 1, 2, ..., N(\tau)-1]^T$ and $m_0(\tau)$ is the starting fringe-order in the spectrum.

$$OPD(\tau)\cdot[k_m(\tau)]_{N\times1} + \phi_0(\tau)\cdot[I]_{N\times1} = 2\pi\left([m(\tau)]_{N\times1} + m_0(\tau)\cdot[I]_{N\times1}\right) \tag{3.74}$$

Based on the position of each peak, multiple OPD values can be estimated, as expressed by the following equation:

$$[OPD_m]_{N\times1} = [c_m]_{N\times1} + [d_m]_{N\times1} Y \tag{3.75}$$

In Eq.3.75, we define the [*c*] and [*d*] vectors as: $[c_m]_{N\times1} = 2\pi[m/k_m]_{N\times1}$, $[d_m]_{N\times1} = [1/k_m]_{N\times1}$, and an auxiliary phase $Y = 2\pi m_0 - \varphi_0$. The solution of Eq.3.62 gives the least-square estimation of the auxiliary phase $\hat{Y}$:

$$\hat{Y} = -\sum_{m=0}^{N-1} C_m D_m \Big/ \sum_{m=0}^{N-1} D_m^2 \tag{3.76}$$

where $C_m = c_m - \overline{c}_m$ and $D_m = d_m - \overline{d}_m$, and $\overline{x}$ denotes the average value of x (averaged over m fringe orders in a single spectrum). The OPD can then be estimated from the measured total phase shift $\hat{\psi}$ based on Eqs.3.75 and 3.76:

$$\hat{OPD} = \overline{c}_m + \overline{d}_m \hat{Y} \tag{3.77}$$

From the auxiliary phase $\hat{Y}$, one could also estimate the additional phase term according to:

$$\hat{\varphi}_0 = 2\pi \,\text{floor}\left[\hat{Y}/(2\pi)\right] - \hat{Y} \tag{3.78}$$

Where the function floor(x) denotes rounding the variable x to the nearest integer less than or equal to x. In practice, the estimation of $\hat{\varphi}_0$ and $\hat{OPD}$ can fluctuate with the same trend during measurement, which results in unwanted ripples in the measured value of $\hat{OPD}(\tau)$. This phenomenon is illustrated in the results of experimental testing of the algorithm. To eliminate this problem, we propose a significant departure from existing FP sensor interrogation techniques. Instead of monitoring changes in OPD, we define a new sensor measurement parameter, average total phase $\overline{\Phi}$, calculated by inserting measured $\hat{OPD}$ and $\hat{\varphi}_0$ into Eq.3.58. $\overline{\Phi}$ represents the total phase at a fixed reference wavenumber, taken to be the central point in the wavenumber scan range.

$$\overline{\Phi}(\tau) = \hat{OPD}(\tau)\cdot\overline{k} + \hat{\varphi}_0(\tau) \tag{3.79}$$

As proven by the numerical simulations and experimental results, the use of average total phase $\overline{\Phi}$ as a new measurement parameter allows for dynamic recalculation of initial phase $\varphi_0(\tau)$ while retaining the high measurement resolution of conventional signal demodulation methods.

3.4.4 Algorithm testing and results

Simulation of multimode-induced phase variation

Computer simulation was performed to verify that the total phase measurement algorithm can eliminate demodulation jumps when initial phase changes more than π. The spectrogram of an IFPI sensor was simulated using Eq.3.67 with the step-index optical fiber parameters outlined in Table 3.6.

A total of 180 spectra, with an SNR of 35dB, were generated and evenly distributed over a temperature range from 0 to 800^{o}C. As the simulated temperature increased, a phase shift of about -1.2π was generated due to multimode excitation in the MMF. This phase shift and OPD change were calculated using the algorithm in 3.4.3 and plotted in Figure 3.25. The blue curve in the figure shows the OPD demodulated using an algorithm which assumed constant phase. As shown in the figure, when the phase shifts over π, a series of

jumps occur as a result of fringe-order estimation ambiguity. In contrast, the red curve shows the OPD calculated using the new varying phase algorithm, which is shown to remove the fringe-order-ambiguity induced OPD jumps completely.

Table 3.6. Simulation parameters for SMS-IFPI sensor.

SMF core radius	4.5μm
SMF core refractive index	1.445
SMF cladding refractive index	1.440
MMF core radius	25.0μm
MMF core refractive index	1.448
MMF cladding refractive index	1.434
MMF coefficient of thermal expansion (CTE)	$0.5\times10^{-6}(1/^{o}C)$
MMF thermo-optic coefficient (TOC)	$0.65\times10^{-5}(1/^{o}C)$

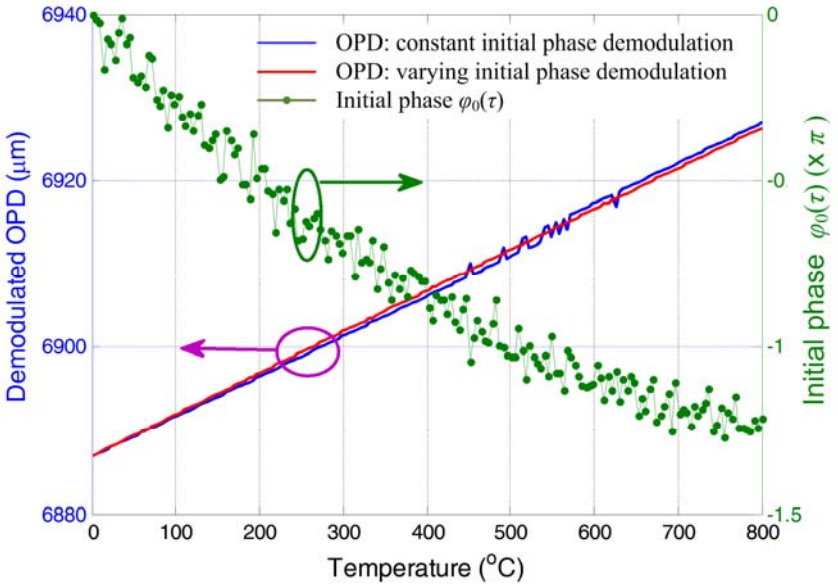

Figure 3.25. OPD of an IFPI sensor (demodulated using traditional constant phase and new total phase algorithms) and its phase shift $\Delta\varphi$ under increasing temperature. Spectral data generated by computer simulation

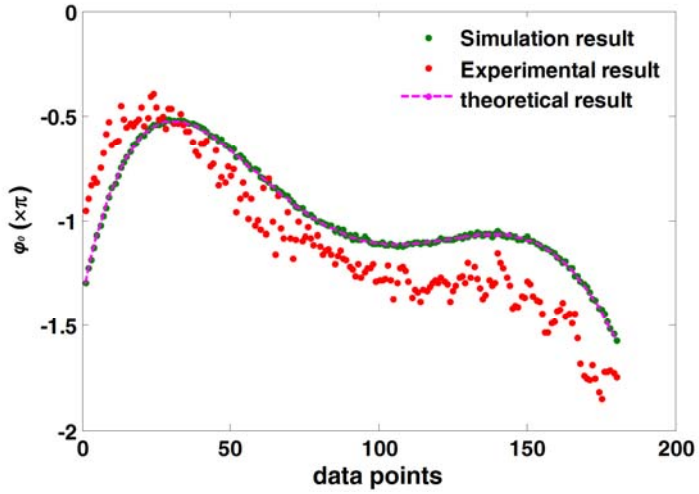

Figure 3.26. Comparison of simulated, experimental and theoretical variations in initial phase $\varphi_0(\tau)$ due to finite wavelength scan rate S.

Simulation of sampling rate-induced phase variation

In order to demonstrate the effects of finite sampling rate on initial phase, an IFPI sensor was heated from room temperature to 600^{o}C in 30 minutes, while a total of 180 spectra were recorded at equal time intervals. The rate of temperature increase varied throughout the heating process, which led to a non-constant OPD changing rate R. The measured OPD and additional phase φ_{0meas} of the sensor were estimated at each sampling point using the algorithm developed in 3.4.3. Next, the rate of OPD change R was estimated by applying a fifth-order polynomial fit to the measured OPD vs. sample number data.

Using Eq.3.72, the estimated R curve was applied to generate a set of simulated spectra containing the theoretical dependence of $\Phi(k)$ on sampling rate S and OPD change rate R. This simulated data was then re-processed to calculate its additional phase φ_{0sim}. Figure 3.26 shows the comparison between measured additional phase φ_{0meas}, simulated additional phase φ_{0sim}, and the theoretical sampling-induced phase shift in Eq.3.73. All three curves clearly have the same shape, confirming the analytical sampling-induced phase shift result. A total initial phase shift of slightly less than π is shown to result from this finite sampling rate phenomenon. The varying total phase algorithm is able to interrogate the sensor without introducing jumps in the demodulated output.

Simulated noise performance

The performance of the total phase algorithm was further evaluated by identifying its OPD estimation accuracy at different noise levels, as shown in Figure 3.27. The evaluation method employed was similar to that in [27]. The Mean-Square-Error (MSE) was evaluated at different cavity lengths and SNR levels by averaging over 1000 measurements at each given condition. An additional phase ranging from 0 to 1.2π was introduced into the simulated spectra and evenly distributed over the 1000 statistical sampling points to demonstrate the robustness of the algorithm against phase drifts larger than π. The corresponding Cramer-Rao bound (see 4.2.2) is also plotted in Figure 3.27 to show that the varying total phase method can reach the upper theoretical bound of linear regression-based algorithms even at the presence of a phase shift as large as 1.2π.

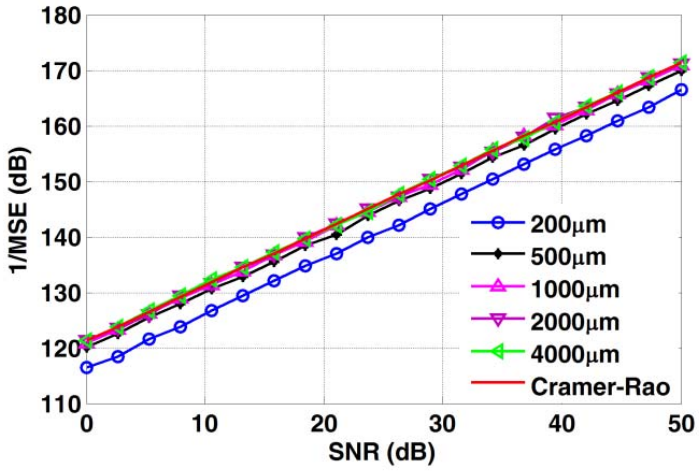

Figure 3.27. Performance of the varying total phase algorithm evaluated at different cavity lengths and SNR levels. MSE errors were calculated based on 1000 sampling points, among which phase shift from 0- 1.2π was evenly distributed. Each spectrum contains 20000 points spaced over 1520-1570nm.

Experimental evaluation of algorithm

The benefits of the varying total phase algorithm are further demonstrated by the following two experiments. In the first experiment, an IFPI temperature sensor with strong multimode excitation was used in order to show the superior performance of the algorithm in an extreme case, in which large phase shift exists due to the modal behavior

of the cavity. The environmental temperature of the sensor was raised from room temperature to 600°C.

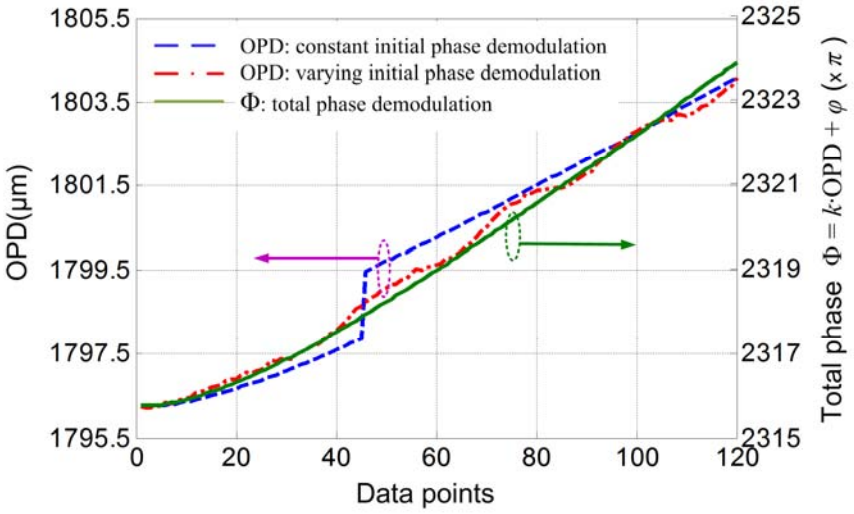

Figure 3.28. IFPI sensor OPD (demodulated using traditional constant phase and new total phase algorithms) and total phase $\Phi=k\cdot OPD+\varphi_0$ during an experimental controlled temperature increase.

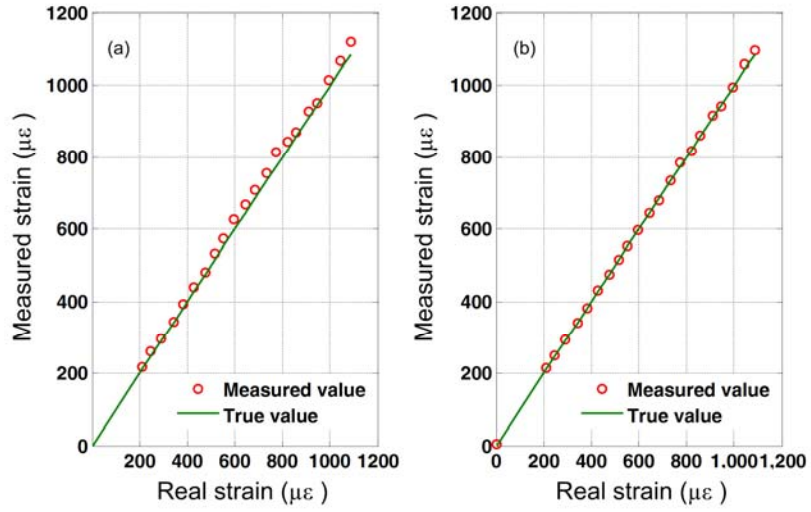

Figure 3.29.IFPI strain sensor evaluation: demodulated by (a) traditional fixed-phase OPD method, (b) new varying total phase method

As shown in Figure 3.28, if the phase term is assumed to be constant, a pronounced OPD demodulation jump is observed at the point where the initial phase shift exceeds π. If the

variable initial phase algorithm in Eqs. 3.76, 3.77 is used to demodulate the sensor, the measured OPD exhibits no demodulation jump. However, the estimated OPD exhibits a strong, quasi-sinusoidal fluctuation, which is attributed to the heavy modal-excitation in the cavity as described in 3.3.1 (not to demodulation error).

These periodic fluctuations clearly demonstrate that OPD is not a usable sensing parameter when initial phase is allowed to vary. Instead, average total phase $\overline{\Phi}$ (Eq. 3.79) is calculated to quantify changes in the IFPI sensor due to external stimuli. The result is a demodulated total phase curve that is entirely free from both jumps and sinusoidal fluctuations (Figure 3.28).

A second experiment was performed to demonstrate the advantage of the total phase algorithm under varying initial phase due to finite laser scan rate. An IFPI sensor was stressed by hanging a dead-weight onto the far-end of the fiber link with burst vibration instabilities caused by swaying of the object. These high-speed fluctuations led to chirp in the spectra due to the limited speed of the wavelength scanning in the optical detection and generated an additional phase term according to Eq. 3.73.

As a result, if OPD is used to characterize the sensor, the strain calibration curve (strain versus demodulated OPD) in Figure 3.29 (a) is full of small fluctuations and suffers from poor repeatability. This is reflected by the large measurement error (RMSE = 19.9$\mu\varepsilon$) obtained using the traditional OPD algorithm. Instead, if the total phase is used to characterize the same fluctuating IFPI data, it results in much better repeatability and measurement accuracy (RMSE = 5.4 $\mu\varepsilon$) as shown in Figure 3.29 (b).

3.5 Conclusion

In this chapter the reflection mode SMS fiber structure employing the GI-MMF (SMS-IFPI) was studied. Splicing reflectivity, IFPI refocusing, and the additional phase in the sensor spectrum were analyzed and discussed. An analytical expression for the SMS-IFPI spectrum, with the reflectivity dictated by the fiber axial index profile was deduced. The model provided a means by which the physical background of the cavity reflection was clearly understood. The IFPI cavity refocusing effect was studied by a ray matrix

approach and fiber modal analysis. The multiplexing capacity of the SMS-IFPI fiber sensors was dramatically increased by promoting refocusing of the propagating light.

Wave-front distortion in the MMF section of a SMS-IFPI sensor is a direct result of the multi-modal nature of the cavity. Similar to EFPI fiber sensors, the wave-front distortion generates an additional phase term in the interference spectrogram of the sensor. The total phase in the spectrogram is modeled by a rotating effective vector. The OPD demodulation process mathematically is the estimation of the rotational speed of the effective vector with respect to wavenumber by looking at the interference spectrum, but the information obtained herein can be misleading to some extent. Hence the error in this first-step estimation amounts to an additional phase shift in the formula used to calculate the total phase. It is predicted that in a real application, if the OPD change is small in a measurement, the change of the additional phase term will not be significant and high measurement accuracy can still be obtained; however, for applications where OPD changes are large, it is possible that the phase term will change very rapidly and accurate OPD decoding will be difficult.

The resultant non-constant phase term in the fiber sensor spectrogram plays an important role in sensor signal demodulation. When a phase shift of π occurs, an ambiguity arises in fringe-order estimation, generating an abrupt jump in the OPD calculated by traditional constant-phase algorithms. These phenomena can cause the resulting measurement to suffer from poor accuracy, even in sensors with high signal-to-noise ratio.

To avoid such jumps, we present a demodulation algorithm based on two key innovations: continuous calculation of a time-varying initial phase, and use of total phase as a measurement parameter instead of OPD. The varying total phase algorithm is shown to have high resolution and to eliminate spurious jumps caused by both multimode excitation and slow wavelength scanning rate. As long as the additional phase shift stays within 2π, no ambiguity exists in the total phase.

Chapter 4 WLI-Based Signal Processing

4.1 Introduction

In the previous chapters, both EFPIs and IFPIs have been theoretically studied. In their applications, the change of the optical path difference (OPD), defined as twice the product of the cavity length and the refractive index of the cavity material, is almost linearly related to the physical parameters being measured; as a result, the key of signal processing is to make accurate measurement of the OPD. The reflection spectrum of the FP sensor is expressed as [93]

$$I(\Phi) = 2R\frac{1-\cos(\Phi)}{1+R^2-2R\cos(\Phi)} \tag{4.1}$$

where R is the reflectance of the cavity mirrors (assume identical reflectivity) and Φ denotes the total phase defined through $\Phi = k \bullet \text{OPD}$, where k is the wavenumber in vacuum. In the regime of "low-finesse", the reflectances of the cavity mirrors are low and multi-reflection is neglected. Such low-finesse FP sensors are more cost-effective, and most importantly, they exhibit outstanding robustness in harsh environments [14]. For such sensors Eq. 4.1 is reduced to

$$\mathrm{I}(\Phi) = 2\mathrm{R}[1-\cos(\Phi)] \tag{4.2}$$

which appears sinusoidal with respect to Φ, and Φ is linear with both OPD and k. In fringe counting mode, a fixed-wavelength laser (or several of them) is injected into the sensor and the reflected power is modified sinusoidally with the OPD (when k is fixed) [22]. Unfortunately as the output is inherently periodic, it provides only relative OPD measurement. Absolute measurement is apparently more desirable and can be achieved using white-light interferometry (WLI) in which a broad-band optical source is used. With WLI, the OPD is measured either by matching the cavity length of a reference interferometer [11] or by direct analysis of the reflected spectrum, the latter is the subject of this chapter.

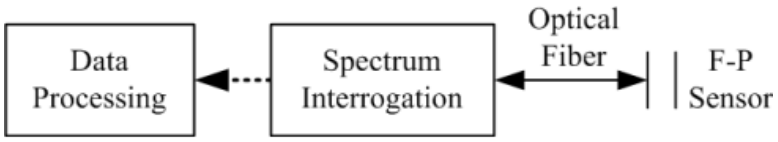

Figure 4.1. Schematic of the fiber optic WLI -FP sensing system.

The schematic of the WLI sensing system is depicted in Figure 4.1. The spectrum interrogation unit comprises of a broadband source and a spectrometer (or a swept-laser spectrometer) which records the reflection spectrum of the FP sensor and sends the data to a processing unit (computer) for demodulation. The spectrum is sinusoidal with wavenumber k according to Eq. 4.2. A variety of demodulation methods have been developed to calculate the OPD directly from the spectrum, and they can be classified into two categories.

The first type is denoted as TYPE I (direct frequency estimation), which relies on the fact that the spectrum is a harmonic function of k, with OPD being the frequency. Estimating the frequency can be achieved by using periodogram (i.e., by Fourier Transform, FT) or phase linear regression. Periodogram is mostly adopted in which the frequency is estimated by tracking the peak position in the FT of the spectrum [37, 45, 94-96], this method is especially powerful for demodulation of multiplexed sensors. An alternative TYPE I approach relies on $\Phi = \mathrm{OPD} \bullet k$ where multiple Φ and k values are obtained from the spectrogram, consequently calculation of OPD is converted to frequency estimation by linear regression. A simple but popular version uses only two points, which usually employs peaks, valleys or zero-crossing points [97-99]. This method offers low resolution and works better for situations where only few peaks exist in the spectrum. If more peaks are available, it is straightforward to use more points to maximize information utilization. In such cases, multiple peak/valley points [42, 100] or the whole spectral data [41, 101] are used for the linear regression.

The second type of algorithm, named TYPE II (total phase), also relies on the relationship $\Phi = \mathrm{OPD} \bullet k$. In a simple version, the spectral position k of one peak is

accurately determined, and the OPD is obtained by Φ/k where the value Φ of the peak is known if the corresponding fringe order is found. Without the knowledge of the fringe order there is an 2π ambiguity in Φ [102]. In order to enable absolute measurement, an improved algorithm estimates the fringe order in the first step by FT or linear regression and subsequently determines the OPD by tracking one peak [39, 103]. This strategy was extended further to utilize the whole spectrum [27]. Apart from estimating only the frequency component in the spectrograph as in TYPE I methods, this approach seeks to estimate the total phase Φ at given spectral points k (or vice versa). Similar task was also accomplished by iterative curve fitting [40, 46, 47].

Despite the success of these developed methods, problems still exist. It is widely accepted (and will be demonstrated later) that the TYPE II approach (total phase) is more accurate than TYPE I (frequency estimation) in calculating the OPD. Unfortunately because the total phase is periodic in nature, a 2π ambiguity may occur during implementation which leads to abrupt discontinuity (or "jumps") in the demodulated OPD [27, 40, 46, 47] (it should be noted that jumps only exist in TYPE II estimations). To date, the cause of the jump is still not thoroughly understood, and consequently eliminating the jump is still not promising. Moreover, a theoretical framework is missing within which the performance of the different algorithms can be evaluated and compared. Due to these reasons, it is reasonable to conclude that the practicality and potentiality of the WLI algorithms are still not fully exploited.

This chapter constructs a set of theories and criteria upon which the performance of the algorithms can be evaluated, and the cause of the jump problem is completely explained (section 4.2). We emphasize the role of an additional phase term which acts as a "hidden killer" to cause the jumps, and propose a more appropriate definition of the total phase with the hope of maximizing noise reduction while maintaining minimum jump risk. In 4.3, the theories will be verified and discussed. Three WLI algorithms will be compared and their pros and cons will be concluded. The physical cause of the additional phase will be further expounded and a solution to minimize the jump occurrence will be demonstrated.

4.2 Theory

4.2.1 Background

In deriving Eq. 4.1, plane wave with normal incidence (parallel to cavity axis) is assumed. In real application, the beam inside the cavity is diffraction limited and its divergence gives rise to a roundtrip power coupling factor ν and accordingly Eq. 4.1 is modified to

$$I(\Phi) = R\frac{1+\nu^2-2\nu\cos(\Phi)}{1+R^2\nu^2-2R\nu\cos(\Phi)} \tag{4.3}$$

with ν<1. $I(\Phi)$ is periodic with Φ and can be subsequently expressed by a Fourier series as

$$I(\Phi) = a_0 + \sum_{n=1}^{\infty} a_n \cos(n\Phi) \tag{4.4}$$

with Fourier coefficients a_n (the sine terms are absent due to symmetry). It is shown that the intensity ratio between adjacent harmonics is (for $n > 0$):

$$a_{n+1}/a_n = R\nu \tag{4.5}$$

which dictates that higher harmonics are orders of magnitude weaker than the fundamental component and can be neglected. As a result we are left with a pure sinusoidal signal which, after normalization appears to be

$$I_{norm}(\Phi) = 1+\frac{2\nu}{1+\nu^2}\cos(k\cdot OPD+\pi) \tag{4.6}$$

The influence of beam divergence is to reduce the signal strength by a factor of $2\nu/(1+\nu^2)$ which is usually referred to as the fringe visibility.

The above discussion only takes into account the loss generated by beam divergence. In fact, divergence also distorts the phase front of the beam, which introduces another phase term φ_0 in the total phase Φ when coupled back into the lead fiber [40]. Eq. 4.6 is finally written in the following form (where $\varphi_0 + \pi$ is combined into φ_0):

$$I_{norm}\left(\Phi\right)=1+\frac{2\nu}{1+\nu^2}\cos\left(k\cdot OPD+\varphi_0\right) \tag{4.7}$$

which best describes the spectrum of a real low-finesse FP sensor. The TYPE I (frequency estimation) approaches calculate OPD directly from the density of the fringes, thus the phase term φ_0 is ignored. On the contrary, this term needs to be considered in the TYPE II approach due to its direct contribution to the value of the total phase, and is usually treated as a constant and pre-calibrated [27, 39]. Nevertheless, this treatment is in most cases not suitable and will result in the demodulation jumps, as will be discussed later.

Most spectrometers provide spectral position readings in unit of wavelength (λ), which result in uneven distribution of k (i.e., $k = 2\pi/\lambda$). It is recommended that the spectrum to be interpolated to yield equal sampling interval in k to take full advantage of standard signal processing techniques. The interpolation error is minimized if "cubic spline" interpolation is used and the associated interpolation error shows negligible influence on the final estimation quality, as will be demonstrated in 4.3.2.

We conclude that the OPD estimation problem is now converted to standard harmonic analysis. Before continuing to the theories, the scope of the subject matter needs to be further clarified. The signal is a discrete, real-valued sequence, with unknown parameters OPD (frequency) and φ_0 (phase) to be estimated. Because the data is real-valued, we define the normalized frequency by $\omega_n = \omega/(2\omega_s)$ where ω_s is the angular sampling frequency, thus

$$\omega_n = OPD\cdot\Delta k/\pi \tag{4.8}$$

where Δk denotes the spectral sampling interval. As can be easily verified, for real systems Eq. 4.8 always yields a number <0.1, which suggests that the signal have "moderately low" frequency. The phrase "moderately low" is picked to distinguish from "extremely low", in which the FT peak in the periodogram is nearly indistinguishable from the direct current (DC) that standard frequency estimation methods (such as the ones to be introduced in 4.3.1) tend to generate large errors. In such cases, the method in [39] is suggested. If the FT peaks are clearly resolvable in the Fourier domain, classical

non-parametric periodgram yields the best performance (i.e., the maximum likelihood estimator) [28], this condition is satisfied for most cases, and is the subject of this chapter. More specifically, this work is confined to single harmonic analysis. For multi-tone analysis usually a filter is used to select the corresponding frequency component, however the problem is complicated by issues such as cross-talk among different channels and the lower bounds of the estimators need to be modified [28]. If multiple harmonic components closely co-exist with deteriorated resolution on the periodogram, parametric methods can be applied [30]. In some applications, the signal is amplitude-modulated by an envelope stemming from the source spectrum. The envelope can be removed by pre-calibrating the source spectrum or by an interpolation process [27, 103]. In sum, after the removal of the envelope and the DC component, the signal is expressed as

$$I_n = A\cos\left(OPD \cdot k_n + \varphi_0\right) + W_n \tag{4.9}$$

where A is the amplitude and k_n is the fixed sampling wavenumber and I_n is the measured intensity at k_n, which is contaminated by zero-mean white Gaussian noise W_n with power σ^2=**var**[W_n] (**var**[•] denotes the variance). The quantities in Eq. 4.9 are all real-valued and n = 1, 2, …N (N is the length of the data). OPD and φ_0 will be the parameters to be estimated, their corresponding estimation values are denoted as $\hat{OPD}$ and $\hat{\varphi}_0$ respectively. The signal to noise ratio (SNR) is defined as $S = A^2/(2\sigma^2)$ [104]. The beginning wavenumber is defined as k_0 and subsequently $k_n = k_0 + (n\text{-}1)\Delta k$, and we define a central wavenumber

$$k_c = (k_1+k_N)/2 \approx k_0 + N\,\Delta k/2 \tag{4.10}$$

which is heavily used throughout the rest of the chapter. Two WLI systems will be applied for simulation and experimental demonstration of the theories. Their system parameters are listed in Table 4.1.

Table 4.1. List of key parameters of the WLI systems used in the research.

System number	Source	Spectrometer	Wavelength range (nm)	N	k_0 (μm^{-1})	Δk (m^{-1})	Remarks
1	LED	OceanOptics Inc.USB2000	715.88-980.64	2048	6.4072	1157.6	Multimode fiber based
2	Micron Optics Inc., Swept laser spectrometer with built-in source, Si-720		1520-1570	20000	4.0020	6.5826	Single-mode fiber based

4.2.2 The theories

Cause of the jump (I): the constant φ_0 assumption

For the TYPE II (total phase) methods, if φ_0 is assumed to be a constant, the jump problem becomes inherent when in fact φ_0 changes during the measurement and the change exceeds π. A detailed analysis of this phenomenon is found in 3.4.2 and Ref.[60]. This can be intuitively understood as follows. While φ_0 shifts, as long as the drift is less than π, the algorithm can find a nearest fringe order (N_0) by a rounding process [39]. However, when the shift is beyond π, the nearest fringe order suddenly moves to $N_0 \pm 1$, and the jump occurs. As a result, assumption of a constant φ_0 should be avoided to prevent jumps.

Total phase estimation with varying φ_0

As stated in the previous subsection, when applying the TYPE II approach (to calculate the total phase), φ_0 cannot be treated as constant. Instead, it should be estimated along with the OPD, and the total phase can be estimated by [60]

$$\hat{\Phi} = k_c \cdot \hat{OPD} + \hat{\varphi}_0 \tag{4.11}$$

where $\hat{OPD}$ and $\hat{\varphi}_0$ are estimated by the TYPE I algorithm and subsequently an estimation of OPD with better resolution is given by:

$$\hat{OPD}_{tot} = \hat{\Phi} / k_c \tag{4.12}$$

The subscript "*tot*" denotes TYPE II OPD estimation by total phase. A major advantage of TYPE II estimation is its superior noise reduction capability. In 4.2.2 and 4.3.5 the

noise reduction mechanism of the TYPE II approach will be analyzed. Moreover, using total phase also benefits from a reduction of bias and demodulation nonlinearity, as will be discussed in 4.3.3, 4.3.5.

Using Eq.4.11, the prerequisite of constant φ_0 is removed. Typically, φ_0 depends on OPD in a deterministic way and can be calibrated within the measurement range (e.g. by polynomial fitting φ_0 = **P**(OPD)). In real practice, one needs to estimate $\hat{OPD}$ and $\hat{\varphi}_0$ in the first step. Similar to Φ, φ_0 is also a phase term and is consequently subject to 2π ambiguity. If φ_0 is pre-calibrated (meaning the relationship of φ_0 = **P**(OPD) is found), one can calculate the expectation value of φ_0 at the given $\hat{OPD}$ as $\tilde{\varphi}_0$ = **P**($\hat{OPD}$), and set a 2π range [$\tilde{\varphi}_0$ - π, $\tilde{\varphi}_0$ + π] to determine $\hat{\varphi}_0$. As will be shown in 4.3.5, this technique can reduce the probability of jump by several orders of magnitude.

The lower bounds

For an estimator its performance can be evaluated by the mean square error (MSE)

$$\mathbf{E}[(\hat{\theta}-\theta)^2] = \mathbf{var}[\hat{\theta}] + \mathbf{bias}^2[\hat{\theta}] \tag{4.13}$$

where **E** denotes average, and $\hat{\theta}$ is the estimated value of the parameter θ. In general the estimator is assumed to be unbiased and the MSE reduces to the variance of the estimator. However unbiasedness is not a straightforward assumption and will be discussed in detail in 4.3.3. In any circumstances, the variance of the estimator cannot be arbitrarily small, the lower bound of which is defined by the Cramér-Rao bound (CRB). Here, without proof, the CRBs for the frequency and phase estimations in WLI are given, the derivations can be found in [105]. Define $P = N(N\text{-}1)/2$, $Q = N(N\text{-}1)(2N\text{-}1)/6$, $n_0 = k_0/\Delta k$, and $Y = n_0^2 N + 2n_0 P + Q$,

The CRB of OPD estimation with unknown φ_0 is (OPD of TYPE I):

$$\mathbf{var}[\hat{OPD}] = \frac{12}{S\cdot(\Delta k)^2 N\left(N^2-1\right)} \tag{4.14}$$

The CRB of OPD estimation with known φ_0 is (this is an approximation of the CRB of TYPE II OPD. See 4.3.5):

$$\mathbf{var}[\hat{OPD}] = \frac{1}{S \cdot (\Delta k)^2 Y} \tag{4.15}$$

The CRB of φ_0 estimation with unknown OPD is (φ_0 of TYPE I):

$$\mathbf{var}[\hat{\varphi}_0] = \frac{12Y}{S \cdot N^2 (N^2 - 1)} \tag{4.16}$$

The CRB of φ_0 estimation with known OPD is (Φ of TYPE II):

$$\mathbf{var}[\hat{\varphi}_0] = \frac{1}{S \cdot N} \tag{4.17}$$

For WLI systems, both OPD and φ_0 are unknown. Eq. 4.14 defines the lower bound of the OPD estimation variance for the TYPE I algorithms ("frequency estimation"), the lower bound of phase estimation variance of TYPE I methods is given by Eq. 4.16. Eq. 4.17 is the CRB of Φ estimation (total phase of TYPE II, Eq. 4.11), and accordingly the TYPE II OPD estimation ($\hat{OPD}_{tot}$) has a variance limit of

$$\mathbf{var}[\hat{OPD}_{tot}] = \frac{1}{S \cdot N \cdot k_c^2} \tag{4.18}$$

To demonstrate that Eq. 4.17 is the CRB of $\hat{\Phi}$, we take the variance on both sides of Eq. 4.11, and notice that when the frequency (OPD) is known, the variances of $\hat{\Phi}$ and $\hat{\varphi}_0$ coincides, which sets the lower bound of the total phase estimation. A more detailed explanation of the noise reduction mechanism of the total phase approach will be given in 4.3.5. The benefit of using total phase is clear when Eq. 4.18 and Eq.4.14 are compared. The root mean square (RMS) error of the direct frequency estimation is much larger than the total phase based OPD estimation by a factor of (by taking the square root of (Eq.4.14)/(Eq.4.18))

$$G = 2\sqrt{3}\left(\frac{n_0}{N} + \frac{1}{2}\right) \tag{4.19}$$

For WLI System I, it is calculated that G ≈ 11.09 and for WLI System II, G ≈ 107.04. This predicts that the OPD estimation resolution using total phase is approximately 10dB and 20dB better than the direct frequency estimation, for system I and II respectively. More benefits of using total phase will be further discussed in section 4.3.5. In general, if high resolution is required, total phase demodulation is recommended. However, one major drawback of the approach is the potential of the demodulation jumps.

Cause of the jump (II): estimation noise of φ_0

The probability density function (PDF) of $\hat{\varphi}_0$ is a Gaussian with mean φ_0 and variance σ_p^2 (the lower bound of the variance is defined by Eq. 16) and is expressed as

$$f\left(\hat{\varphi}_0;\varphi_0,\sigma_p^2\right)=\frac{1}{\sigma_p\sqrt{2\pi}}\exp\left[-\frac{\left(\hat{\varphi}_0-\varphi_0\right)^2}{2\sigma_p^2}\right] \tag{4.20}$$

As discussed in 4.2.2, a 2π range is assigned to φ_0 in order to unambiguously determine its value. A jump event will occur if $\hat{\varphi}_0$ falls out of the assigned range, this would lead to addition or subtraction of multiple 2π's in order to force $\hat{\varphi}_0$ back to the given range. The probability of jump is minimized if the range is centered at φ_0, where the probability is defined by the following inequity:

$$P_{jump}\geq 2F\left(f;-\pi\right)=2\int_{-\infty}^{-\pi} f\left(\hat{\varphi}_0;\varphi_0,\sigma_p^2\right)d\hat{\varphi}_0 \tag{4.21}$$

where F denotes the cumulative distribution function. It should be noted that in principle the jump cannot be eliminated (value of Eq.4.21 is always >0), however it can approach zero if σ_p is small and the 2π range is appropriately selected. The jump probability minimizes when the estimator reaches the CRB and the 2π range is centered at φ_0. One can thus estimate the jump probability by Eqs. 4.16 and 4.21. The probability escalates rapidly if σ_p is large and/or the range is not centered at φ_0, we will illustrate this situation in more detail in 4.3.5.

4.3 Discussion

4.3.1 WLI algorithms

The periodogram (FFT method)

The maximum likelihood estimator of single harmonic is the periodogram which can be regarded as the best algorithm [28, 105]. However, this method has been considered to yield poor accuracy when applied in WLI. The reasons for this belief are: 1) periodogram was used as a TYPE I estimator in the past, i.e., only $\hat{OPD}$ is estimated. As a result of the discussion in 4.2.2, compared with the TYPE II approaches, the resolution of periodogram is worse; 2) the implementation of the algorithm is not optimized.

Because the signal is real, its FT is symmetric about zero and only $N/2$ data points are effective in the periodogram. This basically dictates the normalized frequency resolution to be limited to $2/N$. To improve the resolution, zero padding is widely adopted to increase N [37]. Taking derivative of Eq. 4.8 on both sides, and denoting the frequency resolution as $d\omega_n = 2/N$, it is found that in order to resolve a frequency difference of δOPD, the number of points needed is

$$N = \frac{\lambda_c^2}{\delta OPD \cdot \Delta\lambda} \tag{4.22}$$

in which λ_c is the central wavelength and $\Delta\lambda$ is the wavelength interval of the spectrometer. To achieve resolution of δOPD = 1Å, for WLI System I, $N = 7.4 \times 10^7$ and for WLI System II, $N = 9.6 \times 10^9$. The required data size will lead to unrealistic computational load and result in extremely low efficiency. To improve its efficiency, it is recommended that following a rough estimation of the FT peak position with relatively short N, the normalized frequency in Eq. 4.8 is further determined by the Newton-Raphson method to maximize [28, 105]

$$\left|A\left(\omega_n\right)\right| = \left|\sum_{n=0}^{N-1} I_n \exp\left(-i \cdot \pi n \omega_n\right)\right| \tag{4.23}$$

and the estimations of OPD and φ_0 are obtained by

$$\hat{OPD} = \hat{\omega}_n \pi / \Delta k \tag{4.24}$$

$$\hat{\varphi}_0 = \arg\left[\exp\left(-i\hat{OPD}\cdot k_0\right) A\left(\hat{\omega}_n\right)\right] \tag{4.25}$$

This method is expected to yield the maximum-likelihood estimation to reach the CRB. It is abbreviated as FFT method and will be discussed further in the following subsections.

Linear regression (LR method) and peak tracking (PT method)

In the linear regression method, Φ of all the data points are calculated by solving the angle of the analytical signal, followed by a linear fitting to their corresponding spectral positions k_n, details of the method can be found in [27]. Eq. 4.13 in [27] is used to estimate the OPD and φ_0. This method is abbreviated as LR.

Instead of using all the spectral points for linear regression, the peak tracking method uses only the peak positions in the spectrum. Corresponding details can be found in 3.4.3 ([60]), and Eqs. 3.77 and 3.78 in 3.4.3 are used to determine the OPD and φ_0. This method is abbreviated as PT. At first glance the accuracy of PT should be lower than LR because only a small portion of the spectral data (only the peak points) are used; however this is not true because actually all the points contribute to the determination of the peak positions.

For the LR and PT methods, it is important to use a band-pass filter to clean the signal in advance to increase the breakdown threshold (which is defined as a SNR value beyond which the error of the estimator abruptly becomes significantly larger than the CRB) [27]. It is found that an effective order of the filter is $N_f = N/10$. If N_f is too small, the noise reduction is not sufficiently effective; on the contrary, if N_f is too large, the effective length of the data is sacrificed to an extent that the CRB is apparently lifted. It is also important to shift the filtered data back $N_f/2$ points to compensate the filtering delay, otherwise a large phase bias would occur.

4.3.2 Evaluation of the algorithms

The algorithms in 4.3.1 were evaluated by comparison with the corresponding CRBs using computer simulation. In the simulation, an FP cavity with OPD = 200μm was assumed, and the parameters of WLI System I was used. White Gaussian noise was added to the sensor spectrum according to the required SNR. At each SNR level, one

thousand sets of spectral data were generated, and the variances of the FFT, LR and PT methods were calculated for both TYPE I and TYPE II (by using Eqs.4.11,4.12) estimations. Plotted together are the corresponding CRBs.

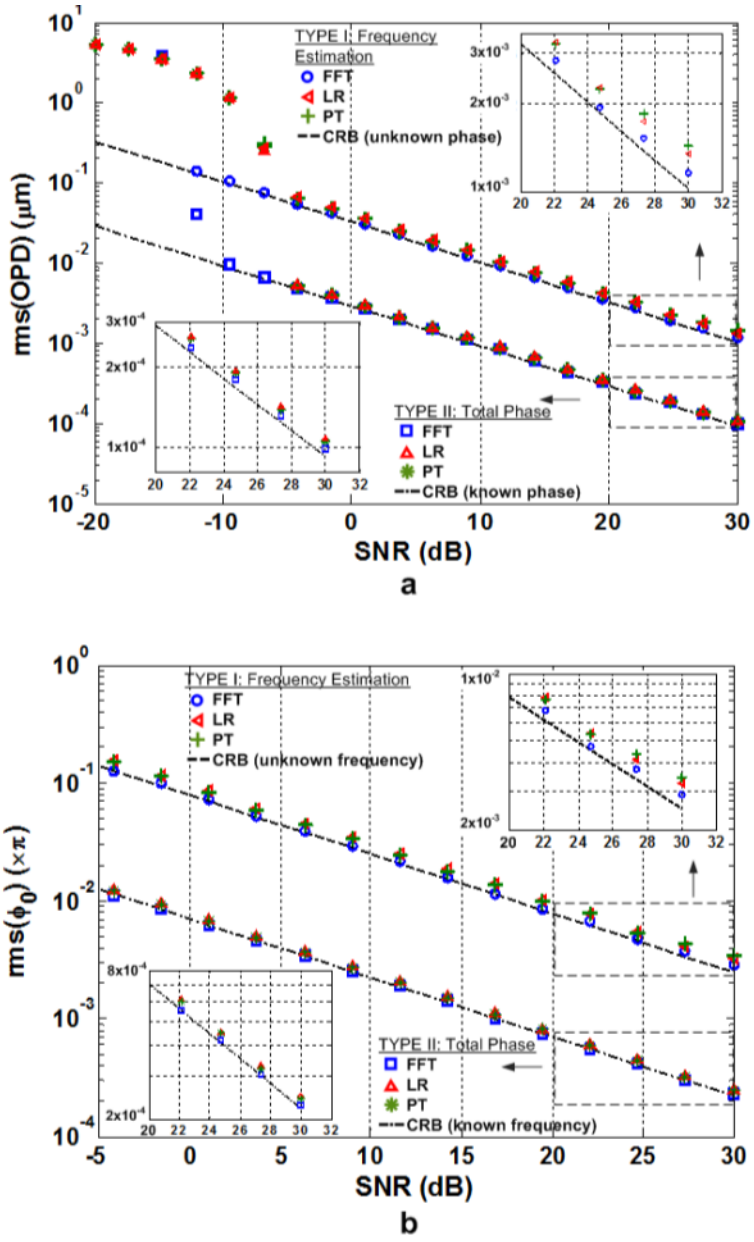

Figure 4.2. Performance evaluation of the FFT, LR and PT methods, plotted together in both figures are the standard deviation of both the TYPE I and TYPE II estimators. a: OPD estimation and b: φ_0 estimation. The CRBs for the corresponding variances are co-plotted. Insets are zoomed-in views of the curves, which provide better visibility of the algorithms' performances.

On the figure of OPD estimation, the CRB for frequency estimation with known phase was plotted, which is sufficiently accurate as the CRB for TYPE II OPD estimator (see 4.3.5). Because the estimators were assumed to be unbiased, the simulation used their standard deviation as the RMS error. The discussion on estimator bias is given in 4.3.3. As demonstrated by Figure 4.2, all three algorithms approach the CRBs nicely. It should be noted that the input spectrum was evenly-sampled in wavelength. Reaching the CRB demonstrated the effectiveness of the interpolation process that evenly sampled the spectrum in wavenumber. The FFT method, as expected, shows the best performance, whereas the LR and PT methods demonstrate nearly identical performances. The threshold of the LR and PT methods take place at SNR~-5dB, the FFT approach shows a lower threshold below -10dB, which suggests better immunity to noise. Reaching the CRB is a manifestation of the performance optimization. In other words, once an algorithm approaches the CRB, it reaches the ultimate limit given the amount of information. Any other WLI algorithms can be evaluated against the CRB under the same framework.

4.3.3 Comparison of the algorithms

Estimator bias

In the previous discussions, the estimators are assumed to be unbiased [105], which is in fact not true for the current situation. The reason is closely related to the properties of the WLI signal. As noted in 4.2.1, the harmonic under analysis is real-valued and bears very low frequency. Unlike complex-valued signal (analytic signal), the real signal is symmetric about zero on the Fourier domain. When the harmonic frequency is low, the positive and negative peaks associated with the harmonic are very close to each other. As the sequence is of finite length, spectral leakage will take place [104, 106], manifesting as side lobes near the FT peaks. The side lobes of the negative peak interfere with the positive peak and slightly change its spectral position. The modification is small but a noticeable bias is incurred when high accuracy is required.

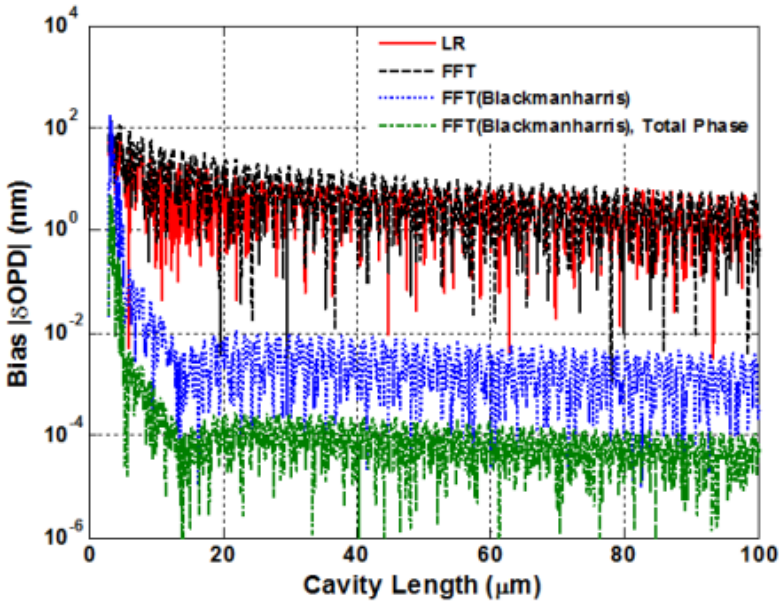

Figure 4.3. Absolute value of OPD bias versus cavity length plotted for TYPE I LR, FFT and windowed FFT (Blackmanharris) estimators. The result for TYPE II estimator using FFT (Blackmanharris) is co-plotted, which demonstrates superior bias suppression.

Windows can be applied to the data to effectively suppress the intensity of the side lobes. The performances of different windows are compared by computer simulation, in which the cavity length of the FP sensor was continuously swept from 3μm to 100 μm, with the cavity refractive index set to unity. During the simulation no noise was added, and the WLI System I parameter was used in the study. The TYPE I OPD estimated using LR, FFT and windowed FFT (with Blackmanharris window) are obtained and the bias of each estimator at the given cavity length was found by comparing with the true value. The results are shown in Figure 4.3. A common feature shown is the tendency toward short cavity, where the influence of spectral leakage surges rapidly for all the estimators, resulting in increased bias. Another feature is the bias's pattern that oscillates with the cavity length, which is apparently a signature of the side lobes. For TYPE I estimation, FFT and LR show unsatisfactorily large bias. Even at cavity length of 100μm, both show a maximum bias of ~10 nm. The oscillatory pattern will promote demodulation nonlinearity. Demonstrated is the effectiveness of windowing to suppress the bias. As shown by the dotted curve, application of Blackmanharris window leads to a bias

suppression ratio over 30dB, the maximum bias was reduced below 10pm for cavity length from 10 to 100μm.

During simulation, φ_0 in the spectrum was set to zero, as a result the TYPE II OPD estimator (Eqs. 4.11, 4.12) becomes unbiased (otherwise TYPE II estimator has an constant bias, which will be discussed in 4.3.5). It is found that the TYPE II estimator shows superior bias reduction, which suppressed the bias further for another ~15dB. The maximum bias for cavity length ranging from 10 to 100μm was uniformly below 1pm, which is of significant importance for high-accuracy applications.

Comparison of the algorithms

In 4.3.2 the performances of the algorithms are evaluated by comparing with the CRBs. In the previous demonstration only the variance is considered. According to Eq. 4.13, the MSE also includes a bias term; as is discussed in the preceding section, the estimators are generally biased which calls for re-examination of their performances. Comparison was made among FFT, LR and windowed FFT (with Blackmanharris window), for both TYPE I and TYPE II estimations by computer simulation, the simulation assumes WLI system I parameters. In order to make the influence of bias more visible, the OPD of the simulated spectrum was shortened to 60μm. At each SNR level, the RMS error was calculated based on comparison of the estimated and true OPD values with 1000 observations. The results are plotted in Figure 4.4. The RMS errors of the TYPE I LR and FFT estimators diverge significantly from the CRB for SNR > 10dB, which is attributed to a big bias. The curve corresponding to windowed FFT in the TYPE I group follows the CRB nicely in the whole SNR range except for a uniform ~3dB degradation. This is attributed to the larger equivalent noise bandwidth associated with the window used [106]. For TYPE II estimators, FFT without windowing shows the worst performance (diverge significantly from CRB starting at SNR ~ 10dB). For the TYPE II LR estimator, significant divergence from CRB happens above SNR ~ 25dB. The performance of the windowed FFT is consistent in the complete SNR range. According to the simulation, for TYPE I estimation, windowed FFT is preferred if SNR is over 20 dB. For TYPE II estimation, for SNR > 30dB, windowed FFT has the best performance, otherwise LR method is sufficient. For applications with high SNR and requiring high accuracy, TYPE

II windowed FFT is the best choice. The simulation predicts that for WLI System I, at SNR =40 dB the RMS estimation error is ~50pm if TYPE II FFT with Blackmanharris window is used.

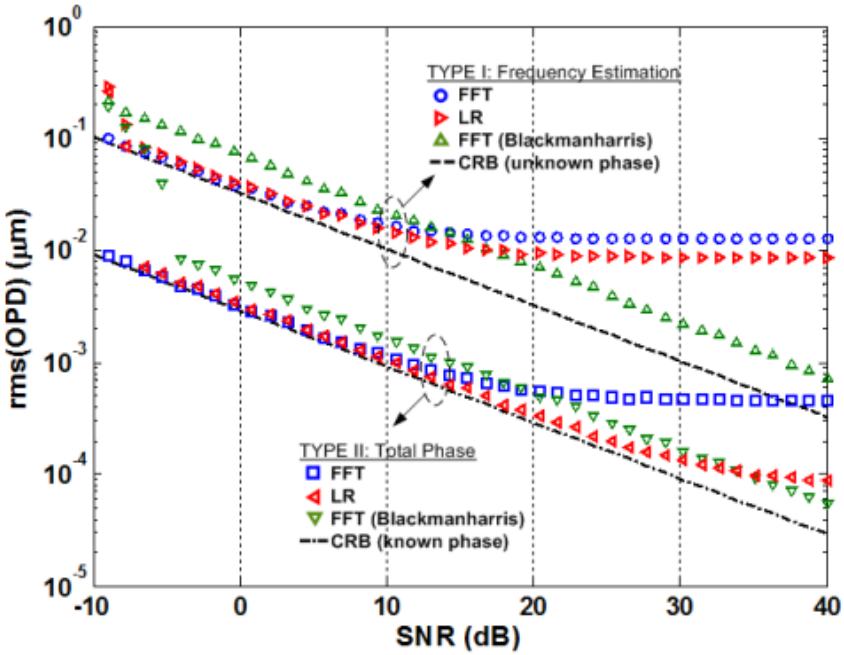

Figure 4.4**.** Performance comparison of the LR, FFT and windowed FFT (Blackmanharris). The RMS error includes the contributions from both the estimator variance and bias. The windowed FFT for both TYPE I and TYPE II estimations manifests superior performance in bias reduction, at the expense of a ~3dB increase in the RMS error.

The computation complexity of the FFT, PT, and LR estimators were compared in terms of computation time. The time was measured by averaging over 1000 executions and as a function of data length (*N*), the result is plotted in Figure 4.5. The investigated algorithms show that the computation time linearly increases with *N*. The LR and PT methods have nearly identical complexity, while the complexity for the FFT method is significantly higher. The calculated complexity can be influenced by a number of factors such as CPU speed and programming skills. However the significantly higher complexity of the FFT estimator is as expected [107].

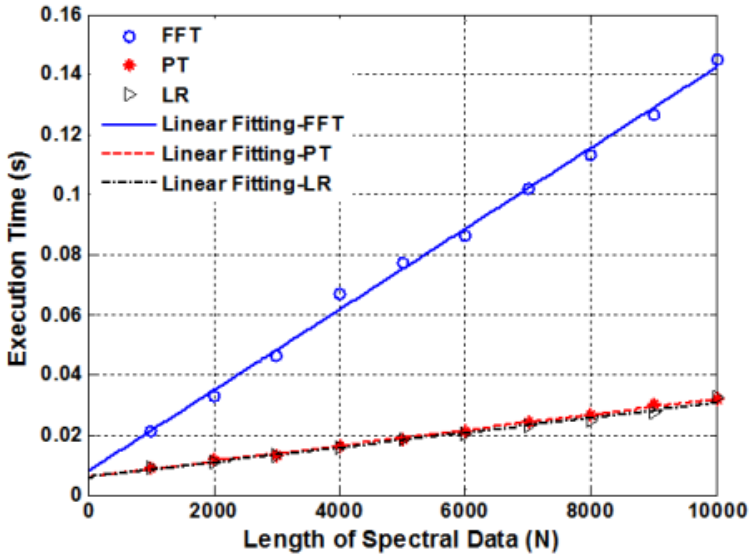

Figure 4.5. Measured computation complexity in terms of execution time, plotted as a function of data length (N). The FFT, PT and LR methods are compared to demonstrate linear relationship with N. The complexity of FFT is the highest while the complexities of PT and LR are almost identical.

4.3.4 OPD-dependent additional phase

We discussed in 4.2.2 that the "constant φ_0" assumption will intrinsically lead to demodulation jumps if TYPE II estimation is made. We concluded from numerous experimental observations that the φ_0 term for both EFPI and IFPI is, in general, dependent on OPD, and more importantly, is usually a function of OPD. Being a function of OPD makes the φ_0 calibratable, which is the key to reducing the probability of jumps as will be discussed in 4.3.5. In this subsection some major causes of the OPD-dependent φ_0 will be introduced; nevertheless, factors not included in this subsection may also cause a changing φ_0.

Phase front distortion

The φ_0 change due to phase front distortion is an inherent property of the FP cavity. In other words, unlike other factors, it is a "built-in" signature of the cavity and is unremovable by any hardware and/or software. At the cavity interface, the optical beam will be diffracted from a fiber mode into either a free-space mode (for EFPI) or other fiber modes (for IFPI). During propagation, the phase front of the cavity mode will

become distorted, and a non-zero phase term will be generated when the phase-front-distorted beam is recoupled back into the lead-in fiber. Intuitively, the greater the distortion is, the larger the phase term would be; as the distortion is OPD-dependent, so is the induced phase. For EFPI, detailed analysis can be found in [40, 52, 108], and the case for IFPI was studied in [59]. In general, for EFPI, the phase term caused by phase front distortion is small and changes moderately with OPD; for IFPI, due to multi-mode excitation, this term could be large and change more rapidly.

Material dispersion

If the FP cavity is filled by a material with chromatic dispersion (i.e., not air), and while the spectral bandwidth of the spectrometer is large (e.g., WLI System I), material dispersion can cause a "chirp" in the spectrum which finally amounts to a spurious phase term. The material dispersion is described by the Sellmeier model, the coefficients of the model are all temperature-dependent. For a temperature sensor, changing the temperature subsequently changes the OPD, while the Sellmeier coefficients simultaneously vary to cause a changing φ_0. This was simulated using the parameters of the WLI System I and a silica wafer with initial thickness of 70μm. Dispersion of the wafer was modeled by the temperature-dependent Sellmeier model with parameters from [67]. During the simulation, temperature was increased from 20°C to 1300°C, and the linear coefficient of thermal expansion (CTE) was set to $8.5\text{x}10^{-6}$. The φ_0 term was calculated using Blackmanharris windowed FFT and plotted as the solid line in Figure 4.6. The agreement of the simulation result with experiment will be given later in 4.3.5.

Fixed-pattern noise (FPN)

A pixel-sensor (such as a CCD) usually bears fixed-pattern noise due to uneven pixel-to-pixel sensitivity [109]. Some spectrometers (such as the spectrometer used in WLI system I) are built with such devices. Typically the FPN is small enough for accurate spectral analysis, however for sensitive OPD measurement, the influence from the FPN can be noticeable. The OPD-dependent phase term φ_0 can be understood as follows. The spectrum of the FP sensor with the FPN is written as (with time-dependent noise excluded)

$$I_n = A\cos\left(OPD \cdot k_n + \varphi_0\right) + \bar{W}_n \tag{4.26}$$

where $\bar{W}_n$ represents the FPN. The Fourier domain spectrum is thus expressed as

$$\tilde{I}_k = \mathbf{FFT}_k\left(I_n\right) = S_k + \tilde{w}_k \tag{4.27}$$

where S_k is the FT of the harmonic signal and $\tilde{w}_k$ is the FT of the FPN. A major difference between the FPN and normal noise is that $\tilde{w}_k$ is fixed for each Fourier bin.

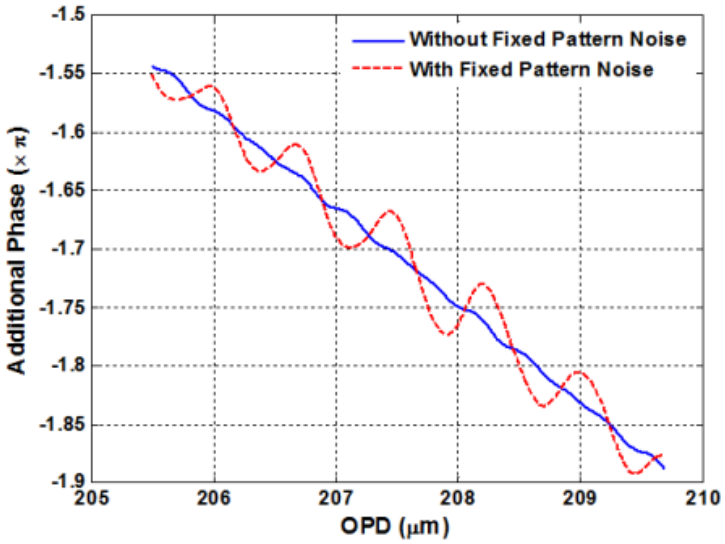

Figure 4.6. Computer-simulated phase term φ_0 caused by material dispersion (solid) and fixed-pattern noise (dashed). The dispersion of a 70μm-thick silica wafer was modeled by the temperature-dependent Sellmeier model. WLI System I, together with Blackmanharris windowed FFT was used for signal demodulation. For the simulation of fixed-pattern noise, the applied white Gaussian noise yields a SNR = 12 dB.

When OPD changes, the FT peak position scans continuously, and the interference from $\tilde{w}$ is dependent on the peak position, thus the OPD estimation error becomes OPD-dependent. This OPD error is finally translated to a phase error via Eq. 4.25. The FPN induced phase shift always shows up with an oscillating pattern (with respect to OPD) with a period roughly equal to λ_c (the central wavelength). This can be easily understood by recalling that after the OPD shifts λ_c, the spectrum nearly recovers, and the influence by the FPN will consequently repeat. The FPN-induced phase was simulated by adding a

fixed white Gaussian noise to the spectrum acquired by WLI system I, which resulted in an equivalent SNR = 12 dB. This noise was added upon the spectra which are previously used to simulate and plot the dispersion-related phase (Figure 4.6, solid curve), and the final results are shown on the same figure as the dashed curve. The simulated influence indeed shows up as an OPD-dependent oscillatory phase term.

Finite sampling rate (FSR)

If the spectrometer has a finite sampling rate (FSR) across the full spectral range (e.g., WLI System II, the laser scanning rate is 5 Hz), the FSR will couple with the OPD changing rate to generate an additional phase. The added phase can be expressed as [60]

$$\Delta\varphi_0 \approx \left(\frac{dOPD}{dt}\right)\cdot\frac{k_c^2}{f_s N\Delta k} \tag{4.28}$$

where f_s denotes the scanning frequency and the derivative term represents the OPD changing rate. Among all the factors that induce the OPD-dependent φ_0, this FSR-induced phase is the most difficult to be removed, because it depends on the instantaneous OPD changing rate, and thus cannot be pre-calibrated.

4.3.5 More on total phase

The noise reduction mechanism of TYPE II estimations

In 4.2.2, we have shown the noise reduction gain (defined as the ratio between the RMS errors of TYPE I and TYPE II estimations) in Eq. 4.17 and a simple proof of the statement is given in 4.2.2. In this section we will explain more on the noise reduction mechanism of the TYPE II approaches.

Taking the variance on both sides of Eq. 4.18, we get

$$\mathbf{var}[\hat{\Phi}] = k_c^2\cdot\mathbf{var}[\hat{OPD}] + 2k_c\cdot\mathbf{cov}[\hat{OPD},\hat{\varphi}_0] + \mathbf{var}[\hat{\varphi}_0] \tag{4.29}$$

where **cov**[•] denotes the covariance. The values of the terms on the right-hand-side of Eq. 4.29 can be obtained from the components of the inversed Fisher information matrix, and correspondingly labeled as $J^{(i,j)}$ (i,j = 1,2). The values of $\mathbf{var}[\hat{OPD}] = J^{(11)}$ and

$\mathbf{var}[\hat{\varphi}_0]=J^{(22)}$ are defined in Eqs. 4.14 and 4.16, respectively. The value of $\mathbf{cov}[\hat{OPD},\hat{\varphi}_0]$ is determined by the anti-diagonal elements $J^{(1,2)}=J^{(2,1)}$ which can be calculated as:

$$J^{(1,2)}=J^{(2,1)}=-\frac{6\left(2n_0+N-1\right)}{S\cdot\Delta k\cdot N\left(N^2-1\right)} \tag{30}$$

The value is negative and sets the lower limit of the covariance in the sense that $|\mathrm{cov}[\bullet]| \geq |J^{(1,2)}|$. To estimate the variance of $\hat{\Phi}$ we insert Eqs. 4.14, 4.16 and 4.30 into Eq. 4.29, and get

$$\mathbf{var}[\hat{\Phi}]\approx\frac{12k_c^2N-12k_c\Delta k\left(2n_0+N-1\right)N+12\Delta k^2Y}{S\cdot\Delta k^2\cdot N^2\left(N^2-1\right)} \tag{31}$$

In order to simplify Eq. 4.31, the following approximations are made:

$$P\approx\frac{N^2}{2} \tag{4.32.1}$$

$$Q\approx\frac{N^3}{3} \tag{4.32.2}$$

$$k_c\approx k_0+\frac{1}{2}N\Delta k=\left(n_0+\frac{1}{2}N\right)\Delta k \tag{4.32.3}$$

$$k_c^2\approx\frac{Y\Delta k^2}{N}-\frac{\left(N\Delta k\right)^2}{12} \tag{4.32.4}$$

From (4.32.4) the following equation is obtained:

$$Y\Delta k^2\approx\left[1+\frac{1}{12}\left(\frac{N}{n_0}\right)^2\right]k_c^2N=\left(1+C_0\right)k_c^2N \tag{4.33}$$

Inserting (4.32.1)~(4.32.4) into Eq. 4.31 and after some mathematical manipulations, we get

$$\mathbf{var}[\hat{\Phi}] \approx \frac{1}{S \cdot N} \tag{4.34}$$

which is the CRB of $\hat{\varphi}_0$ with known OPD (Eq. 4.17). We can further prove that the TYPE II OPD estimation (Eq. 4.12) approaches the CRB of OPD estimation with known φ_0 by inserting Eq. 4.33 and Eq. 4.12 into Eq. 4.34 and setting $C_0 = (N/n_0)^2/12 \approx 0$ (to demonstrate, put in parameters for WLI System I, we get $C_0 \approx 0.01$ and for WLI System II $C_0 \approx 0.0001$), and finally get

$$\mathbf{var}[\hat{OPD}_{tot}] \approx \frac{1}{S \cdot (\Delta k)^2 Y} \tag{4.35}$$

which is the CRB for OPD estimation with known phase (Eq. 4.15). The above calculation was confirmed by computer simulation in which the variance and covariance terms in Eq. 4.29 are numerically solved (OPD = 200μm, WLI System I with FFT estimator was used, at each SNR 1000 observations were made).

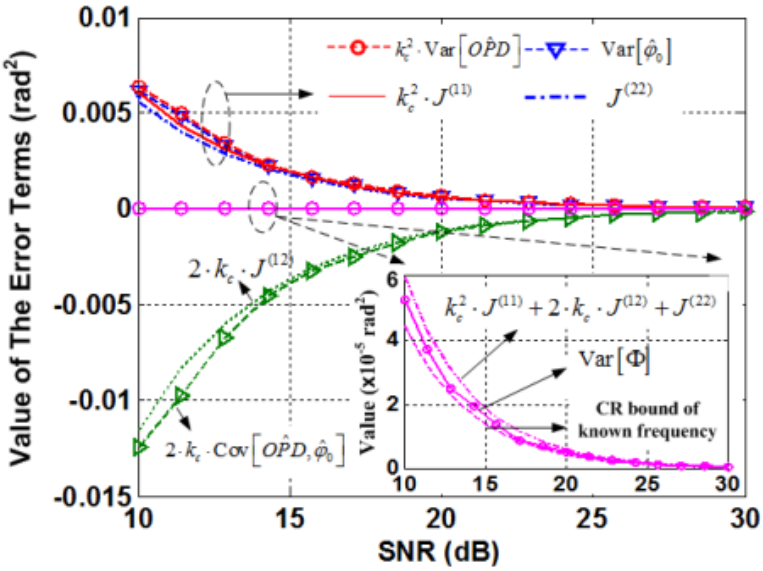

Figure 4.7. Computer-simulated variance and covariance terms in Eq. 4.29. The corresponding CRBs are plotted together. An important observation is that the variance terms and the covariance term cancel to yield a significantly reduced variance for the total phase estimation.

The result is plotted in Figure 4.7. The figure clearly shows how the covariance term cancels the variance terms (they have similar magnitude but opposite signs) to yield a much smaller variance for the total phase estimation. As the value of C_0 reduces, the difference between the two lines in the inset figure (corresponding to Eq. 4.29 and Eq. 4.34) will gradually vanish. It should be noted that Eq. 4.34 is the real CRB for the total phase estimation, whereas Eq. 4.29 is only an approximation (as shown in the figure, the variance falls in between the two lines).

Characteristics of the estimated total phase

The benefit of TYPE II estimation is multifold. First, as is demonstrated previously, the TYPE II estimators have superior noise reduction capability. The RMS error reduction factor for OPD is given in Eq.4.19, and the CRB of the TYPE II OPD estimator approaches the CRB of OPD estimation with known phase. Secondly, as shown in 4.3.3, the estimation bias of TYPE II estimator is much lower than that of the TYPE I's. More generally, the total phase estimation, $\hat{\Phi}$, follows the real OPD change more linearly than $\hat{OPD}$. At first glance, the definition of TYPE II OPD estimator (Eq.4.12) introduces a bias term (Eq. 4.11, $\hat{\varphi}_0$ term). In fact, it is the inclusion of this term that reduces the demodulation nonlinearity. In real applications, the projection from the real OPD change to the demodulated $\hat{OPD}$ (TYPE I) change is always not perfectly linear. This is caused by the nonlinearly changing φ_0 as discussed in 4.3.4. Interestingly, the divergence from linear that $\hat{\varphi}_0$ experiences is always accompanied by a proportional $\hat{OPD}$ deviation in the opposite direction (that is why $\hat{OPD}$ is not quite linear), however the outcome is a cancellation of the nonlinearity in the total phase which adds the two oppositely diverging terms. In sum, the TYPE I $\hat{OPD}$ has worse translation fidelity due to the influence of the spurious additional phase $\hat{\varphi}_0$, however the translation to $\hat{\Phi}$ is much linear. An excellent example is given in 3.4.4, Figure 3.28.

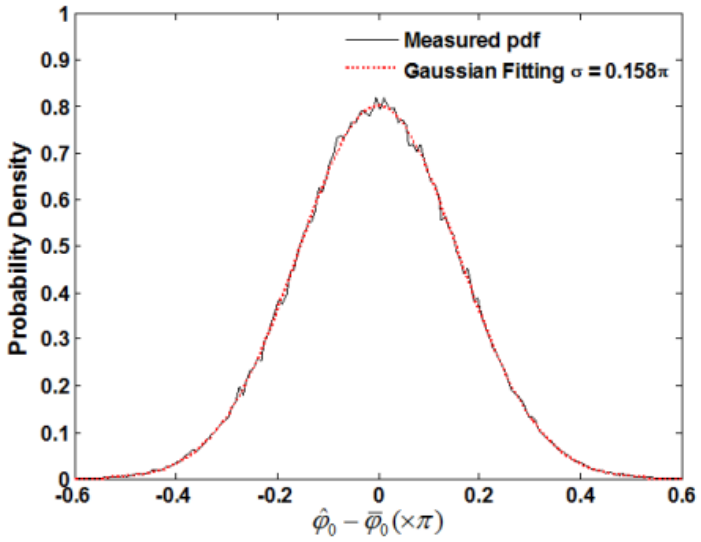

Figure 4.8. Experimentally obtained PDF of φ_0 estimation.

Reducing the probability of jump in TYPE II estimations

Despite its multiple benefits, a major drawback of the TYPE II estimation is the demodulation jump as discussed in 4.2.2. Based on the assumption that the PDF of $\hat{\varphi}_0$ is Gaussian, the theory in 4.2.2 predicts the lower limit of the jump probability by Eq. 4.21, and this limit is reached when the 2π phase confinement range is centered on φ_0 and the estimator reaches the phase CRB. It should be noted that the Gaussian PDF of the phase estimation is an essential assumption of the theory, which is demonstrated in Figure 4.8. The PDF plotted in the figure was obtained with a real EFPI sensor whose phase was kept constant during the measurement. The WLI System I was used in conjunction with the PT method, and the PDF was calculated from 200,000 estimations, which can be well fitted by a Gaussian with $\sigma_p = 0.158\pi$.

From the discussion in 4.2.2 and 4.3.4, the OPD-dependent phase term φ_0 can be calibrated in advance such that during real measurement, the expectation value of φ_0 can be estimated by $\hat{OPD}$, resulting in a proper assignment of the 2π phase range for $\hat{\varphi}_0$ with minimum jump risk.

In detail, after calibration, the φ_0 term is fitted with the OPD using a polynomial as $\varphi_0 =$ **P**(OPD). In real measurement, $\hat{OPD}$ and $\hat{\varphi}_0$ are estimated by a TYPE I estimator (e.g.,

FFT), and the expectation value of φ_0 is obtained by $\tilde{\varphi}_0 = \mathbf{P}(\hat{OPD})$. Then, multiple 2π will be added to or subtracted from $\hat{\varphi}_0$ such that it falls within the range $[\tilde{\varphi}_0 - \pi, \tilde{\varphi}_0 + \pi]$. Finally, the TYPE II OPD is estimated by Eqs. 4.11,4.12.

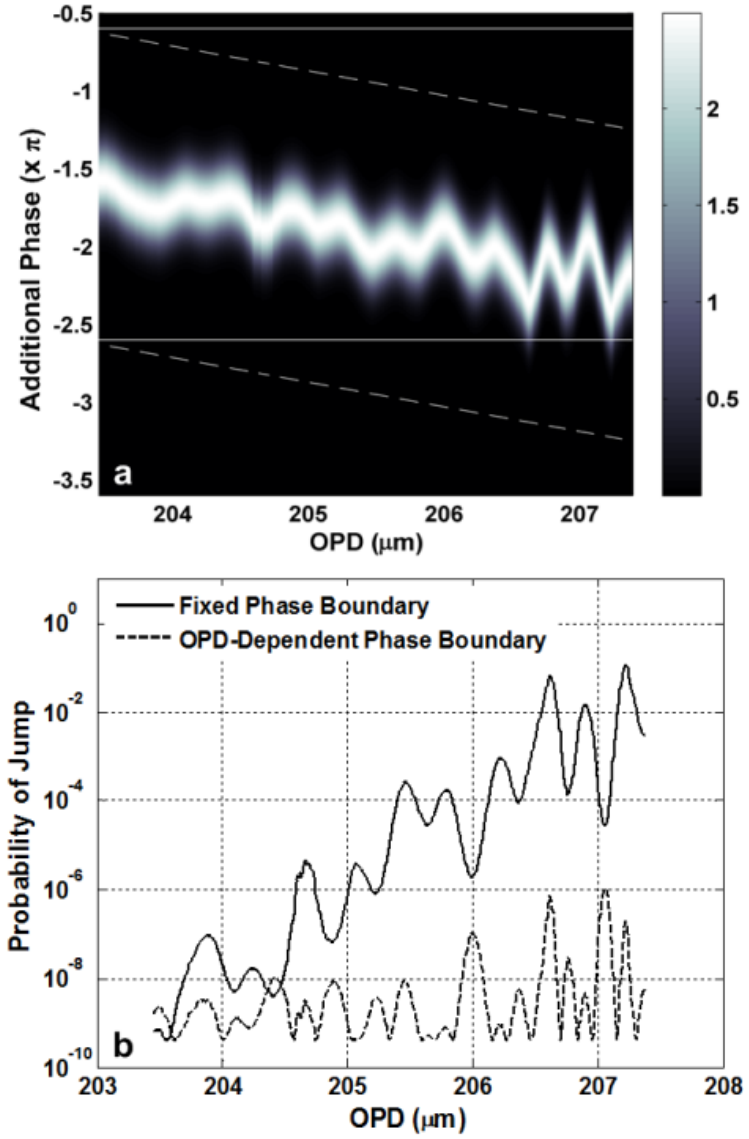

Figure 4.9**.** Reduction of jump probability by phase calibration. a: PDF of φ_0 estimation plotted with OPD, $\sigma_p = 0.158\pi$. The area between the solid lines is the assigned phase range assuming constant phase, dashed lines are the boundaries of the OPD-calibrated range with linear fitting. b: The corresponding probability of jump. Solid line: OPD-dependent jump probability for the constant range scheme. Dashed line: jump probability for the calibrated range scheme.

In Figure 4.9 an example is given to illustrate the above process. In (a), the color map of the PDF of the estimated phase is plotted as a function of OPD. The data was acquired experimentally from a sapphire-wafer based EFPI temperature sensor [14]. During the phase calibration, sufficient amount of data was recorded to capture the OPD-φ_0 relationship (comparing with Figure 4.6 reveals reasonable agreement). For simplicity, a linear fitting was used to fit the phase with the OPD, and accordingly the phase confinement range was assigned, shown as the dashed lines in the figure. In comparison, the solid lines are an alternative range scheme which centered at the initial φ_0 but assume constant values. According to the PDF of $\hat{\varphi}_0$ and the values of the range boundaries, the probability of jump (i.e., the probability of having phase estimation outside the pre-defined range) is plotted in (b) for both range schemes. For the fixed phase boundary (solid line in a), the maximum probability of jump reached ~10% at OPD ≈ 207.2μm, whereas using the OPD-dependent phase boundary the jump probability was uniformly below 1 part per million (ppm). A reduction of jump probability by 10^5 was resulted.

4.4 Conclusion

The demodulation of the WLI low-finesse FP sensor is identical to parameter estimation of a noise-contaminated, real, discrete tone with finite length. This forces us to solve the problem, and to evaluate the estimators in the context of harmonic analysis. We call attention to the importance of the Cramér-Rao bounds, because any developed algorithms should be evaluated using the bounds as standards. Three algorithms are compared in terms of their errors (including estimation variance and bias) and complexities; comparisons with the CRBs are highlighted.

In spite of its similarity to traditional harmonic analysis, the WLI problem bears some unique features. The data is real, and has finite length and low frequency, consequently the bias caused by spectral leakage becomes dominant when the SNR is high. A solution is to use windows with effective side lobe suppression in the periodogram, at the expense of moderately increased variance.

The TYPE I estimation (denoted as $\hat{OPD}$) will suffice if the requirement for resolution is not high. Despite low resolution, this approach has no jump problem. If high resolution is

desired, both $\hat{OPD}$ and $\hat{\varphi}_0$ need to be estimated, and subsequently combined to yield the TYPE II estimation ($\hat{OPD}_{tot}$). $\hat{OPD}_{tot}$ has significantly reduced estimation error and demodulation nonlinearity, however it has the risk of abrupt demodulation jumps. The jump is attributed to the $\hat{\varphi}_0$ term, the value of which is intrinsically ambiguous (with 2π-step jumps). Moreover, the value of φ_0 is not a constant and can vary during measurement. As such, $\hat{\varphi}_0$ and $\hat{OPD}$ are of parallel importance in TYPE II estimation. If φ_0 is reliably dependent on OPD, it can be calibrated in advance and an appropriate (OPD-dependent) 2π range can be assigned to $\hat{\varphi}_0$ to minimize the occurrence of jumps.

Chapter 5 Summary and Future Work

5.1 Summary

This dissertation addresses several theoretical issues in low-finesse fiber optic Fabry-Perot Interferometric sensors. The work is divided into two levels, and both levels coupled to each other closely. The first level is modeling of the FPI sensors, in which both EFPI and IFPI were studied. The second level is white-light-interferometry-based signal processing of the FP sensors. With a practical model, the physical behaviors of the FP structures are better understood, which helps gear toward optimized cavity and system design for reliable signal processing; on the other hand, understanding of the basic signal processing principles sets forth certain criteria by which the fabrication and operation of the sensors should obey.

A model for low finesse EFPI was developed in Chapter 2. Compared with prior models, this new model is more practical in describing a real cavity. The deduction of the theory was based on a rigorous diffraction treatment of the field in the FP cavity, and through some reasonable approximations, we reached a transform pair between the interferometer output and the spatial power density distribution projected onto the fiber transmission axis. With approximations, such relationship reduces to a Fourier-transform problem, and presents a *k*-domain analogy of the Wiener-Khintchine theorem. The theory was experimentally proven using both single-mode fiber and multimode fiber based EFPIs, and relationships between the new model with other models were established. We found that the fringe visibility and additional phase in the interferogram were strongly influenced by the output spatial power density distribution and working wavelength, but were not directly related to either temporal or spatial degree of coherence. According to the model, different fiber excitation condition results in quite distinctive features of the visibility curve, and maximizing the fringe contrast relies on designing the excitation to yield a minimized beam divergence. At last, the OPD-dependent additional phase terms were analyzed separately for air-gap and wafer-based EFPIs. It was found that, in principle, the additional phase of an air-gap cavity changed very moderately while that of a wafer-based cavity was dominantly affected by material dispersion. The significance of this observation is further explored in Chapter 4.

Secondly, the SMS-IFPI structure was theoretically studied (Chapter 3). Splicing reflectivity, IFPI refocusing, and the additional phase in the sensor spectrum were modeled. The IFPI cavity refocusing effect was studied by a ray matrix approach and fiber modal analysis. As a result of the study, the multiplexing capacity of the SMS-IFPI fiber sensors was dramatically increased by promoting refocusing of light. Wave-front distortion in the MMF section of a SMS-IFPI sensor is a direct result of the multi-modal nature of the cavity. Similar to EFPI fiber sensors, the wave-front distortion generates an additional phase term in the interference spectrogram. The total phase in the spectrogram is modeled by a rotating effective vector. Such effect poses a spurious OPD-dependent additional phase in the spectrum. It is predicted that in a real application, if the OPD change is small in a measurement, the change of the additional phase term will not be significant; however, for applications where OPD changes are large, it is possible that the phase term will change very rapidly and accurate OPD decoding will be difficult. The resulted non-constant phase term in the fiber sensor spectrogram plays an important role in sensor signal demodulation. When a phase shift of π occurs, an ambiguity arises in fringe-order estimation, generating an abrupt jump in the OPD calculated by traditional constant-phase algorithms. These phenomena can cause the resulting measurement to suffer from poor accuracy, even in sensors with high signal-to-noise ratio. To avoid such jumps, a new demodulation algorithm based was developed, which calculates not only the OPD, but also the additional phase, and uses both values for the calculation of the total phase. The algorithm is shown to have high resolution, and is able to eliminate spurious jumps as long as the additional phase shift stays within 2π.

At last, signal processing of the FP sensors using WLI was studied (Chapter 4). The demodulation of the WLI low-finesse FP sensor is identical to parameter estimation of a noise-contaminated, real, discrete tone with finite length. This forces us to solve the problem, and to evaluate the estimators in the context of harmonic analysis. The Cramér-Rao bounds of the WLI algorithms were calculated, and any developed algorithms should be evaluated using the bounds as standards. Three algorithms were compared in terms of their errors (including estimation variance and bias) and complexities; comparisons with the CRBs were highlighted. In spite of its similarity to traditional harmonic analysis, the WLI problem bears some unique features. The data is real, and has finite length and low

frequency, consequently the bias caused by spectral leakage becomes dominant when the SNR is high. A solution is to use windows with effective side lobe suppression in the periodogram, at the expense of moderately increased variance. Two types of algorithms were studied and compared. The TYPE I estimation will suffice if the requirement for resolution is not high. Despite low resolution, this approach has no jump problem. If high resolution is desired, both OPD and the additional phase need to be estimated, and subsequently combined to yield the TYPE II estimation. Such estimation has significantly reduced estimation error and demodulation nonlinearity, however it has the risk of abrupt demodulation jumps. The jump is attributed to the additional phase term, the value of which is intrinsically ambiguous (with 2π-step jumps). Moreover, the value of the additional phase is not a constant, and can vary during measurement. If the additional phase is reliably dependent on OPD, it can be calibrated in advance and an appropriate (OPD-dependent) 2π range can be assigned to minimize the occurrence of jumps.

5.2 Contributions and publications

The major contributions of this dissertation are listed below.

- A theory for SMF-/MMF-EFPI is developed. This model is more accurate than the geometric-optics-based approach, and is more practical compared with the more sophisticated fiber modal analysis approach. The model, with solid experimental validation, successfully describes the change of fringe visibility and additional phase with major cavity and system parameters. The discovery of the Fourier-transform-like dependence of the fringe visibility on the spatial light power distribution is of great theoretical and practical values. The model is useful for EFPI system optimization.
- A model of SMS-IFPI is built using fiber modal analysis. Two major predictions of the model are cavity refocusing and OPD-dependent additional phase. The significance of the cavity refocusing lies in the fact that multiplexing capacity of the sensors is improved from less than 6 to more than 20. The importance of the additional phase is its relationship with the abrupt signal demodulation jumps.
- The signal processing algorithms for low-finesse FPIs are reviewed, classified, evaluated, and improved. Theorems are developed to describe the ultimate estimation resolution and the origins and probability of demodulation jumps. Optimized

algorithm is found, and comparison among different algorithms is provided. The additional phase term is identified as a hidden factor to cause the demodulation jumps, and means of reducing the jump probability by sensor pre-calibration is proposed and demonstrated.

The major publications by the author during the dissertation are listed below.

- **Cheng Ma**, Bo Dong, Evan Lally and Anbo Wang, Optimization of single-/multi-/single-mode intrinsic Fabry-Perot fiber sensors, J. Lightwave Technol., v 30, p 2281-2288, 2012.
- **Cheng Ma**, Bo Dong, Jianmin Gong and Anbo Wang, Decoding the spectrum of extrinsic Fabry-Perot fiber interferometers, Opt. Express, v 19, p 23727-23742, 2011.
- **Cheng Ma** and Anbo Wang, Toward eliminating signal demodulation jumps in white-light optical fiber intrinsic Fabry-Perot interferometric sensors, J. Lightwave Technol., v 29, p 1913-1919, 2011.
- **Cheng Ma** and Anbo Wang, Multimode excitation-induced phase shifts in intrinsic Fabry–Perot interferometric fiber sensor spectra, Appl. Opt. v 49, p 4836-4845, 2010.
- **Cheng Ma** and Anbo Wang, Optical fiber tip acoustic resonator for hydrogen sensing, Opt. Lett., v 35, p 2043-2045, 2010.
- **Cheng Ma**, Brian Scott, Gary Pickrell and Anbo Wang, Porous capillary tubing waveguide for high-temperature carbon monoxide detection, IEEE Photon. Technol. Lett., v 22, p 323-5, 2010.
- **Cheng Ma**, Brian Scott, Gary Pickrell and Anbo Wang, Porous capillary tubing waveguide for multigas sensing, Opt. Lett., v 35, p 315-17, 2010.

5.3 Recommendation for future work

Some theoretical and experimental works, which are direct extensions of the dissertation, are not pursued. However, they are of great potential impacts. The following is a list of the suggested future work.

5.3.1 Elimination of the demodulation jumps

Elimination of the OPD demodulation jumps (in TYPE II algorithms) is possible using the phase-precalibration method developed in 4.3.5 (although complete elimination is impossible, reducing the probability below a small threshold value, e.g., 10^{-6}, could be achieved). However, there are two potential problems. 1) The repeatability of the additional phase evolution is still not fully demonstrated. Even if the repeatability is confirmed, the additional phase-OPD relationship can be sometimes more complicated than depicted in Figure 4.9. As such, a simple mathematical calibration relationship is difficult to find. 2) The repeatability of the phase-OPD relationship among different sensors needs to be confirmed. If the phase evolution differs from sensor to sensor, calibration has to be performed for each individual sensor. The complexity involved will lead to high cost, and in turn dramatically discounts the viability of the approach. In order to economically eliminate the demodulation jumps, answers to the following questions are necessary: 1) Can the additional phase be made repeatable? 2) Can the change of the additional phase, within the full measurement range, be made minimum and linear by optimized sensor design?

5.3.2 Improvement of the fringe visibility

For MMF-EFPI, the fringe visibility is highly sensitive to the parallelism of the cavity mirrors and the diverge angle of the light beam. Such constraints significantly increase the sensor manufacture complexity, giving rise to high cost. According to the theory, it is possible to relax the requirement for sensor elements (such as wafer thickness and parallelism) by controlled fiber excitation and selection of working wavelength: beam pre-collimation and longer wavelength operation are practical means to improve fringe visibility.

5.3.3 Development of universal FPI demodulation software

The present computer programs developed for OPD demodulation are written in raw Matlab codes. Their compatibility will be extended by converting into C or C++. For real application, a program applicable to all types of FPIs is highly desirable, which can automatically detect effective spectral range, select proper algorithm, be compatible with

sensor multiplexing, and perform data conversion according to the specific data acquisition instrument.

5.3.4 Application of the FV-$I(k_z)$ relationship

The FV-$I(k_z)$ relationship developed in 2.2.2 has been successfully applied in EFPI modeling to predict the sensor spectrum given the device structure. The relationship is basically a one-to-one projection between the visibility curve and the light spatial distribution. It is possible, for example, to characterize the optical beam distribution by measuring the visibility curve of a low-finesse FP cavity placed co-axially with the beam. It is therefore potentially useful for optical component characterization, such as measurement of the mode field diameter of optical fibers.

Bibliography

1. M. Nikles and F. Ravet, "Distributed fibre sensors: Depth and sensitivity," Nat Photon **4**, 431-432 (2010).
2. "Carbon Trust invests in ultrahigh temperature sensor," Nature Photonics **4**, 424-424 (2010).
3. A. F. Abouraddy, M. Bayindir, G. Benoit, S. D. Hart, K. Kuriki, N. Orf, O. Shapira, F. Sorin, B. Temelkuran, and Y. Fink, "Towards multimaterial multifunctional fibres that see, hear, sense and communicate," Nat Mater **6**, 336-347 (2007).
4. A. F. Abouraddy, O. Shapira, M. Bayindir, J. Arnold, F. Sorin, D. S. Hinczewski, J. D. Joannopoulos, and Y. Fink, "Large-scale optical-field measurements with geometric fibre constructs," Nat Mater **5**, 532-536 (2006).
5. M. Bayindir, F. Sorin, A. F. Abouraddy, J. Viens, S. D. Hart, J. D. Joannopoulos, and Y. Fink, "Metal-insulator-semiconductor optoelectronic fibres," Nature **431**, 826-829 (2004).
6. J. P. Dakin, D. J. Pratt, G. W. Bibby, and J. N. Ross, "Distributed optical fibre Raman temperature sensor using a semiconductor light source and detector," Electronics Letters **21**, 569-570 (1985).
7. T. Horiguchi, K. Shimizu, T. Kurashima, M. Tateda, and Y. Koyamada, "Development of a distributed sensing technique using Brillouin scattering," Lightwave Technology, Journal of **13**, 1296-1302 (1995).
8. M. Froggatt and J. Moore, "High-Spatial-Resolution Distributed Strain Measurement in Optical Fiber with Rayleigh Scatter," Appl. Opt. **37**, 1735-1740 (1998).
9. D. A. Jackson, "Monomode optical fibre interferometers for precision measurement," Journal of Physics E: Scientific Instruments **18**, 981 (1985).
10. D. A. Jackson, "Recent progress in monomode fibre-optic sensors," Measurement Science and Technology **5**, 621 (1994).
11. C. Belleville and G. Duplain, "White-light interferometric multimode fiber-optic strain sensor," Opt. Lett. **18**, 78-80 (1993).
12. H. Xiao, J. Deng, G. Pickrell, R. G. May, and A. Wang, "Single-Crystal Sapphire Fiber-Based Strain Sensor for High-Temperature Applications," J. Lightwave Technol. **21**, 2276 (2003).

13. H. Xiao, J. Deng, Z. Wang, W. Huo, P. Zhang, M. Luo, G. R. Pickrell, R. G. May, and A. Wang, "Fiber optic pressure sensor with self-compensation capability for harsh environment applications," Optical Engineering **44**, 054403-054410 (2005).
14. Y. Zhu, Z. Huang, F. Shen, and A. Wang, "Sapphire-fiber-based white-light interferometric sensor for high-temperature measurements," Opt. Lett. **30**, 711-713 (2005).
15. B. Yu, D. W. Kim, J. Deng, H. Xiao, and A. Wang, "Fiber Fabry-Perot Sensors for Detection of Partial Discharges in Power Transformers," Appl. Opt. **42**, 3241-3250 (2003).
16. Y. Zhang, X. Chen, Y. Wang, K. L. Cooper, and A. Wang, "Microgap Multicavity Fabry-Perot Biosensor," Lightwave Technology, Journal of **25**, 1797-1804 (2007).
17. D. Rugar, H. J. Mamin, and P. Guethner, "Improved fiber-optic interferometer for atomic force microscopy," Applied Physics Letters **55**, 2588-2590 (1989).
18. A. Oral, R. A. Grimble, H. O. Ozer, and J. B. Pethica, "High-sensitivity noncontact atomic force microscope/scanning tunneling microscope (nc AFM/STM) operating at subangstrom oscillation amplitudes for atomic resolution imaging and force spectroscopy," Review of Scientific Instruments **74**, 3656-3663 (2003).
19. N. Suehira, Y. Tomiyoshi, Y. Sugawara, and S. Morita, "Low-temperature noncontact atomic-force microscope with quick sample and cantilever exchange mechanism," Review of Scientific Instruments **72**, 2971-2976 (2001).
20. H. I. Rasool, P. R. Wilkinson, A. Z. Stieg, and J. K. Gimzewski, "A low noise all-fiber interferometer for high resolution frequency modulated atomic force microscopy imaging in liquids," Review of Scientific Instruments **81**, 023703-023710 (2010).
21. J. L. Santos, A. P. Leite, and D. A. Jackson, "Optical fiber sensing with a low-finesse Fabry-Perot cavity," Appl. Opt. **31**, 7361-7366 (1992).
22. K. A. Murphy, M. F. Gunther, A. M. Vengsarkar, and R. O. Claus, "Quadrature phase-shifted, extrinsic Fabry-Perot optical fiber sensors," Opt. Lett. **16**, 273-275 (1991).
23. P. Sandoz, "Wavelet transform as a processing tool in white-light interferometry," Opt. Lett. **22**, 1065-1067 (1997).

24. K. G. Larkin, "Efficient nonlinear algorithm for envelope detection in white light interferometry," J. Opt. Soc. Am. A **13**, 832-843 (1996).
25. Z. Li, J. Gong, B. Dong, C. Ma, J. Wang, and A. Wang, "Compact optical path scanner and its application for decoding fiber-optic interferometers," Opt. Lett. **35**, 1284-1286 (2010).
26. T. Li, A. Wang, K. Murphy, and R. Claus, "White-light scanning fiber Michelson interferometer for absolute position-distance measurement," Opt. Lett. **20**, 785-787 (1995).
27. F. Shen and A. Wang, "Frequency-estimation-based signal-processing algorithm for white-light optical fiber Fabry-Perot interferometers," Appl. Opt. **44**, 5206-5214 (2005).
28. S. M. Kay, *Modern Spectral Estimation: Theory and Application* (Prentice Hall, 1999).
29. X. Zhang, *Modern Signal Processing,* 2 ed. (Tsinghua University Press, 2002).
30. Y. J. Rao, X. J. Wang, T. Zhu, and C. X. Zhou, "Demodulation algorithm for spatial-frequency-division-multiplexed fiber-optic Fizeau strain sensor networks," Opt. Lett. **31**, 700-702 (2006).
31. S. Chen, A. W. Palmer, K. T. V. Grattan, and B. T. Meggitt, "Digital signal-processing techniques for electronically scanned optical-fiber white-light interferometry," Appl. Opt. **31**, 6003-6010 (1992).
32. Y. Gong, Y.-J. Rao, Y. Guo, Z.-L. Ran, and Y. Wu, "Temperature-Insensitive Micro Fabry-Perot Strain Sensor Fabricated by Chemically Etching Er-Doped Fiber," Photonics Technology Letters, IEEE **21**, 1725-1727 (2009).
33. B. T. Meggitt, "Fiber optic white-light interferometric sensors Optical Fiber Sensor Technology," K. T. V. Grattan and B. T. Meggitt, eds. (Springer Netherlands, 1994), pp. 269-312.
34. R. O. Claus, M. F. Gunther, A. Wang, K. A. Murphy, and D. Sun, "Extrinsic Fabry-Perot Sensor for Structural Evaluation," Applications of Fiber Optic Sensors in Engineering Mechanics, 60-71 (1993).
35. J. Tapia-Mercado, A. V. Khomenko, and A. Garcia-Weidner, "Precision and sensitivity optimization for white-light interferometric fiber-optic sensors," Lightwave Technology, Journal of **19**, 70-74 (2001).

36. T. Wei, Y. Han, H.-L. Tsai, and H. Xiao, "Miniaturized fiber inline Fabry-Perot interferometer fabricated with a femtosecond laser," Opt. Lett. **33**, 536-538 (2008).
37. S. M. Musa, "Real-Time Signal Processing and Hardware Development for a Wavelength Modulated Optical Fiber Sensor System," Ph.D. dissertation, Virginia Tech (1997).
38. J. Zhang, G. D. Peng, L. Yuan, and W. Sun, "Composite-cavity-based Fabry-Perot interferometric strain sensors," Opt. Lett. **32**, 1833-1835 (2007).
39. B. Qi, G. R. Pickrell, J. Xu, P. Zhang, Y. Duan, W. Peng, Z. Huang, W. Huo, H. Xiao, R. G. May, and A. Wang, "Novel data processing techniques for dispersive white light interferometer," Optical Engineering **42**, 3165-3171 (2003).
40. M. Han, Y. Zhang, F. Shen, G. R. Pickrell, and A. Wang, "Signal-processing algorithm for white-light optical fiber extrinsicFabry-Perot interferometric sensors," Opt. Lett. **29**, 1736-1738 (2004).
41. J. Yi, "Fourier Transform White-Light Interferometry for the Measurement of Fiber-Optic Extrinsic Fabry-Perot Interferometric Sensors," Photonics Technology Letters, IEEE **20**, 75-77 (2008).
42. Y. Jiang, "High-resolution interrogation technique for fiber optic extrinsic Fabry-Perot interferometric sensors by the peak-to-peak method," Appl. Opt. **47**, 925-932 (2008).
43. Y. Jiang and W. Ding, "Recent developments in fiber optic spectral white-light interferometry," Photonic Sensors **1**, 62-71 (2011).
44. A. Majumdar and H. Huang, "Compact optical fiber whitelight interferometric distance sensor for arbitrary small distance measurement," Appl. Opt. **48**, 3702-3708 (2009).
45. A. Majumdar and H. Huang, "Development of an in-fiber white-light interferometric distance sensor for absolute measurement of arbitrary small distances," Appl. Opt. **47**, 2821-2828 (2008).
46. H. Huang, "Data interrogation for Fabry-Perot whitelight interferometry," in (SPIE, 2006), 617419-617417.
47. X. Zhou and Q. Yu, "Wide-Range Displacement Sensor Based on Fiber-Optic Fabry-Perot Interferometer for Subnanometer Measurement," Sensors Journal, IEEE **11**, 1602-1606 (2011).

48. R. Yun-Jiang, "Recent progress in fiber-optic extrinsic Fabry–Perot interferometric sensors," Optical Fiber Technology **12**, 227-237 (2006).
49. V. Arya, M. de Vries, K. A. Murphy, A. Wang, and R. O. Claus, "Exact Analysis of the Extrinsic Fabry-Perot Interferometric Optical Fiber Sensor Using Kirchhoff's Diffraction Formalism," Optical Fiber Technology **1**, 380-384 (1995).
50. F. Pérennès, P. C. Beard, and T. N. Mills, "Analysis of a Low-Finesse Fabry-Perot Sensing Interferometer Illuminated by a Multimode Optical Fiber," Appl. Opt. **38**, 7026-7034 (1999).
51. M. Han and A. Wang, "Exact Analysis of Low-Finesse Multimode Fiber Extrinsic Fabry-Perot Interferometers," Appl. Opt. **43**, 4659-4666 (2004).
52. M. Han and A. Wang, "Mode power distribution effect in white-light multimode fiber extrinsic Fabry-Perot interferometric sensor systems," Opt. Lett. **31**, 1202-1204 (2006).
53. P. R. Wilkinson and J. R. Pratt, "Analytical model for low finesse, external cavity, fiber Fabry-Perot interferometers including multiple reflections and angular misalignment," Appl. Opt. **50**, 4671-4680 (2011).
54. C. E. Lee and H. F. Taylor, "Fiber-optic Fabry-Perot temperature sensor using a low-coherence light source," Lightwave Technology, Journal of **9**, 129-134 (1991).
55. A. Wang, H. Xiao, J. Wang, Z. Wang, W. Zhao, and R. G. May, "Self-Calibrated Interferometric-Intensity-Based Optical Fiber Sensors," J. Lightwave Technol. **19**, 1495 (2001).
56. Y. Kim and D. P. Neikirk, "Micromachined Fabry-Perot cavity pressure transducer," Photonics Technology Letters, IEEE **7**, 1471-1473 (1995).
57. N. Furstenau, M. Schmidt, H. Horack, W. Goetze, and W. Schmidt, "Extrinsic Fabry-Perot interferometer vibration and acoustic sensor systems for airport ground traffic monitoring," Optoelectronics, IEE Proceedings - **144**, 134-144 (1997).
58. S. Tretter, "Estimating the frequency of a noisy sinusoid by linear regression (Corresp.)," Information Theory, IEEE Transactions on **31**, 832-835 (1985).
59. C. Ma and A. Wang, "Multimode excitation-induced phase shifts in intrinsic Fabry-Perot interferometric fiber sensor spectra," Appl. Opt. **49**, 4836-4845 (2010).

60. C. Ma, E. M. Lally, and A. Wang, "Toward Eliminating Signal Demodulation Jumps in Optical Fiber Intrinsic Fabry-Perot Interferometric Sensors," J. Lightwave Technol. **29**, 1913-1919 (2011).
61. M. Born and E. Wolf, *Principles of optics: electromagnetic theory of proagation, interference and diffraction of light,* 7 ed. (Cambrige University Press, 2003).
62. A. Yariv, *Optical electronics in modern communications,* 5th ed. (Oxford University Press, Inc., 1997).
63. E. D. Becker and T. C. Farrar, "Fourier Transform Spectroscopy," Science **178**, 361-368 (1972).
64. M. Artiglia, G. Coppa, P. Di Vita, M. Potenza, and A. Sharma, "Mode field diameter measurements in single-mode optical fibers," Lightwave Technology, Journal of **7**, 1139-1152 (1989).
65. Y. Kokubun and K. Iga, "Mode analysis of graded-index optical fibers using a scalar wave equation including gradient-index terms and direct numerical integration," J. Opt. Soc. Am. **70**, 388-394 (1980).
66. G. Keiser, *Optical Fiber Communications* (McGraw-Hill, Boston,Mass., 2000).
67. G. Ghosh, M. Endo, and T. Iwasaki, "Temperature-dependent Sellmeier coefficients and chromatic dispersions for some optical fiber glasses," Lightwave Technology, Journal of **12**, 1338-1342 (1994).
68. P. R. Horche, M. Lopez-Amo, M. A. Muriel, and J. A. Martin-Pereda, "Spectral behavior of a low-cost all-fiber component based on untapered multifiber unions," Photonics Technology Letters, IEEE **1**, 184-187 (1989).
69. D. Đonlagic and M. Zavrsnik, "Fiber-optic microbend sensor structure," Opt. Lett. **22**, 837-839 (1997).
70. D. Donlagic and B. Culshaw, "Microbend sensor structure for use in distributed and quasi-distributed sensor systems based on selective launching and filtering of the modes in graded index multimode fiber," Lightwave Technology, Journal of **17**, 1856-1868 (1999).
71. A. Kumar, R. K. Varshney, and R. Kumar, "SMS fiber optic microbend sensor structures: effect of the modal interference," Optics Communications **232**, 239-244 (2004).
72. A. Kumar, R. K. Varshney, S. Antony C, and P. Sharma, "Transmission characteristics of SMS fiber optic sensor structures," Optics Communications **219**, 215-219 (2003).

73. D. M. Mackie and A. W. Lee, "Slotted Multimode-Interference Devices," Appl. Opt. **43**, 6609-6619 (2004).
74. S. M. Tripathi, A. Kumar, E. Marin, and J.-P. Meunier, "Single-Multi-Single Mode Structure Based Band Pass/Stop Fiber Optic Filter With Tunable Bandwidth," J. Lightwave Technol. **28**, 3535-3541 (2010).
75. A. Sun, Y. Semenova, and G. Farrell, "A novel highly sensitive optical fiber microphone based on single mode–multimode–single mode structure," Microwave and Optical Technology Letters **53**, 442-445 (2011).
76. W. S. Mohammed, A. Mehta, and E. G. Johnson, "Wavelength tunable fiber lens based on multimode interference," Lightwave Technology, Journal of **22**, 469-477 (2004).
77. Q. Wu, Y. Semenova, P. Wang, and G. Farrell, "High sensitivity SMS fiber structure based refractometer: analysis and experiment," Opt. Express **19**, 7937-7944 (2011).
78. Q. Wang, G. Farrell, and W. Yan, "Investigation on Single-Mode-Multimode-Single-Mode Fiber Structure," J. Lightwave Technol. **26**, 512-519 (2008).
79. S. M. Tripathi, A. Kumar, R. K. Varshney, Y. B. P. Kumar, E. Marin, and J.-P. Meunier, "Strain and Temperature Sensing Characteristics of Single-Mode-Multimode-Single-Mode Structures," J. Lightwave Technol. **27**, 2348-2356 (2009).
80. Q. Shi, Z. Wang, L. Jin, Y. Li, H. Zhang, F. Lu, G. Kai, and X. Dong, "A Hollow-Core Photonic Crystal Fiber Cavity Based Multiplexed Fabry-Perot Interferometric Strain Sensor System," Photonics Technology Letters, IEEE **20**, 1329-1331 (2008).
81. Z. Huang, Y. Zhu, X. Chen, and A. Wang, "Intrinsic Fabry-Perot fiber sensor for temperature and strain measurements," Photonics Technology Letters, IEEE **17**, 2403-2405 (2005).
82. W. Emkey and C. Jack, "Analysis and evaluation of graded-index fiber lenses," Lightwave Technology, Journal of **5**, 1156-1164 (1987).
83. G. Yuan, G. Yu, R. Yun-Jiang, Z. Tian, and W. Yu, "Fiber-Optic Fabry-Perot Sensor Based on Periodic Focusing Effect of Graded-Index Multimode Fibers," Photonics Technology Letters, IEEE **22**, 1708-1710 (2010).

84. Y. Zhang, Y. Li, T. Wei, X. Lan, Y. Huang, G. Chen, and H. Xiao, "Fringe Visibility Enhanced Extrinsic Fabry-Perot Interferometer Using a Graded Index Fiber Collimator," Photonics Journal, IEEE **2**, 469-481 (2010).
85. A. D. Yablon and R. T. Bise, "Low-loss high-strength microstructured fiber fusion splices using GRIN fiber lenses," Photonics Technology Letters, IEEE **17**, 118-120 (2005).
86. A. D. Yablon, *Optical fiber fusion splicing* (Springer, Berlin; New York, 2005).
87. A. K. Ghatak and K. Thyagarajan, *An introduction to fiber optics* (Cambridge University Press, Cambridge; New York, 1998).
88. M. D. Feit and J. J. A. Fleck, "Light propagation in graded-index optical fibers," Appl. Opt. **17**, 3990-3998 (1978).
89. V. Bhatia, M. B. Sen, K. A. Murphy, and R. O. Claus, "Wavelength-tracked white light interferometry for highly sensitive strain and temperature measurements," Electronics Letters **32**, 247-249 (1996).
90. S. M. Tripathi, A. Kumar, R. K. Varshney, Y. B. P. Kumar, E. Marin, and J. P. Meunier, "Strain and temperature sensing characteristics of single-mode-multimode-single-mode structures," Journal of Lightwave Technology **27**, 2348-2356 (2009).
91. S. M. Tripathi, A. Kumar, E. Marin, and J. P. Meunier, "Critical Wavelength in the Transmission Spectrum of SMS Fiber Structure Employing GeO Doped Multimode Fiber," Photonics Technology Letters, IEEE **22**, 799-801 (2010).
92. F. Shen, Z. Wang, W. Peng, K. Cooper, G. Pickrell, and A. Wang, "UV-induced intrinsic Fabry-Perot interferometric sensors and their multiplexing for temperature and strain sensing," in *Smart Structures and Materials 2006: Sensors and Smart Structures Technologies for Civil, Mechanical, and Aerospace Systems, 27 Feb. 2006*, Proc. SPIE - Int. Soc. Opt. Eng. (USA) (SPIE - The International Society for Optical Engineering, 2006), 61740-61741.
93. M. Born and E. Wolf, *Principles of Optics: Electromagnetic Theory of Propagation, Interference and Diffraction of Light,* 7 ed. (Cambridge University Press, Cambridge, 1999).
94. T. Liu and G. F. Fernando, "A frequency division multiplexed low-finesse fiber optic Fabry--Perot sensor system for strain and displacement measurements," Review of Scientific Instruments **71**, 1275-1278 (2000).

95. S. Taplin, A. G. Podoleanu, D. J. Webb, and D. A. Jackson, "Displacement sensor using channelled spectrum dispersed on a linear CCD array," Electronics Letters **29**, 896-897 (1993).
96. C. Boulet, M. Hathaway, and D. A. Jackson, "Fiber-optic-based absolute displacement sensors at 1500 nm by meansof a variant of channeled spectrum signal recovery," Opt. Lett. **29**, 1602-1604 (2004).
97. T. Liu, M. Wu, Y. Rao, D. A. Jackson, and G. F. Fernando, "A multiplexed optical fibre-based extrinsic Fabry-Perot sensor system for in-situ strain monitoring in composites," Smart Materials and Structures **7**, 550 (1998).
98. T. Liu, D. Brooks, A. R. Martin, R. A. Badcock, and G. F. Fernando, "Design, fabrication, and evaluation of an optical fiber sensor for tensile and compressive strain measurements via the use of white light interferometry," in (SPIE, 1996), 408-416.
99. V. Bhatia, K. A. Murphy, R. O. Claus, T. A. Tran, and J. A. Greene, "Recent developments in optical-fiber-based extrinsic Fabry-Perot interferometric strain sensing technology," Smart Materials and Structures **4**, 246 (1995).
100. J. Schwider and L. Zhou, "Dispersive interferometric profilometer," Opt. Lett. **19**, 995-997 (1994).
101. M. Takeda, H. Ina, and S. Kobayashi, "Fourier-transform method of fringe-pattern analysis for computer-based topography and interferometry," J. Opt. Soc. Am. **72**, 156-160 (1982).
102. V. Bhatia, M. B. Sen, K. A. Murphy, and R. O. Claus, "Wavelength-tracked white light interferometry for highly sensitive strain and temperature measurements," Electronics Letters **32**, 247-249 (1996).
103. R. Cortés, A. V. Khomenko, A. N. Starodumov, N. Arzate, and L. A. Zenteno, "Interferometric fiber-optic temperature sensor with spiral polarization couplers," Optics Communications **154**, 268-272 (1998).
104. H. C. So, Y. T. Chan, Q. Ma, and P. C. Ching, "Comparison of various periodograms for sinusoid detection and frequency estimation," Aerospace and Electronic Systems, IEEE Transactions on **35**, 945-952 (1999).
105. D. Rife and R. Boorstyn, "Single tone parameter estimation from discrete-time observations," Information Theory, IEEE Transactions on **20**, 591-598 (1974).
106. F. J. Harris, "On the use of windows for harmonic analysis with the discrete Fourier transform," Proceedings of the IEEE **66**, 51-83 (1978).

107. H. C. So, C. Kit Wing, Y. T. Chan, and K. C. Ho, "Linear prediction approach for efficient frequency estimation of multiple real sinusoids: algorithms and analyses," Signal Processing, IEEE Transactions on **53**, 2290-2305 (2005).
108. C. Ma, B. Dong, J. Gong, and A. Wang, "Decoding the spectra of low-finesse extrinsic optical fiber Fabry-Perot interferometers," Opt. Express **19**, 23727-23742 (2011).
109. T. H. Barnes, "Photodiode array Fourier transform spectrometer with improved dynamic range," Appl. Opt. **24**, 3702-3706 (1985).